STRUCTURE-PROPERTY RELATIONSHIPS FROM MOLECULAR SIMULATION OF POLYMERIC MATRIX COMPOSITES

A Dissertation
Presented to
The Academic Faculty

by

Alexander M. Lohse

In Partial Fulfillment
of the Requirements for the Degree
Doctor of Philosophy in the
School of Materials Science and Engineering

Georgia Institute of Technology
August 2018

STRUCTURE-PROPERTY RELATIONSHIPS FROM MOLECULAR SIMULATION OF POLYMERIC MATRIX COMPOSITES

Approved by:

Professor Karl Jacob, Advisor
School of Materials Science and Engineering
Georgia Institute of Technology

Professor Edmond Chow, Advisor
School of Computational Science and Engineering
Georgia Institute of Technology

Professor Surya Kalidindi
School of Materials Science and Engineering
Georgia Institute of Technology

Professor Jerry Qi
School of Mechanical Engineering
Georgia Institute of Technology

Professor Donggang Yao
School of Materials Science and Engineering
Georgia Institute of Technology

Date Approved: 17 July 2018

To my wife, Bri, whose support and sacrifices made this possible.

ACKNOWLEDGEMENTS

I would like to first thank my advisors, Dr. Karl Jacob and Dr. Edmond Chow. Their guidance and complementary perspectives helped sculpt my research. In addition, both provided valuable life advice at various times throughout my time at Georgia Tech.

I would like to thank my committee members for their time and feedback when writing this dissertation. Specifically, Dr. Surya Kalidindi, whose own research and guidance in the NSF FLAMEL program helped shape part of this research. Dr. Jerry Qi for his expertise in covalent adaptable networks and suggestions for improving my research in that area. Dr. Donggang Yao for his feedback and perspective in the dissertation process.

I need to acknowledge Matthew Wolf for access to computing resources within the College of Computing, without which I would not have been able to complete my work.

I would like to thank Dr. Richard Fujimoto, Holly Rush, and the NSF IGERT FLAMEL program at Georgia Tech for funding this work and putting together a fantastic program at the intersection of materials science and computational engineering. I would also like to thank 3M, specifically Geoffrey Morris, for funding part of this work through the 3M Graduate Fellowship.

I need to thank my wife, Bri, without whose support and own sacrifices this dissertation would not have happened. And finally I need to thank my parents, Jeff and Julie, for their constant support through all my years of education.

TABLE OF CONTENTS

LIST OF TABLES

LIST OF FIGURES

SUMMARY

Epoxy materials are some of the most widely used polymers in the aviation and automotive industries because of their environmental degradation resistance and strength at high temperatures. Carbon fiber reinforced plastic with an epoxy matrix has been used in the defense industry since the 1960's and its use is becoming more prevalent due to its high specific strength, specific modulus, and tailorable mechanical properties. The development of nanomaterials in the past two decades has led to the use of nanofillers, such as graphene and carbon nanotubes, in composites to improve the modulus and in-plane and out-of-plane strength in composites. The number of filler types, functionalities, and orientations in composites reinforced with nano and macroscale fillers leads to a complicated and lengthy trial and error experimental approach. Computational researchers have been trying to find a new approach to narrow down promising combinations of fillers and matrix materials using their known chemical and mechanical attributes. This work is directed toward understanding structure-property linkages in a range of composite materials. This research uses molecular dynamics simulation to analyze the (1) interfacial atomistic structure of a traditional epoxy/graphene system with different surface functionalities, (2) dissolution (recycling) mechanism and thermomechanical properties of covalent adaptable networks (CAN), and (3) reaction mechanism pathways and structure development for carbonization of polyacrylonitrile (PAN). Each section uses modeling of chemical reactions as a method to study structure-property relationships. Non-bonded surface interactions are compared to bonded surface interactions in epoxy/functionalized-graphene composites with bonding occurring through a distance-based bond formation method in classical MD. Transesterification reactions

are modeled through distance and energy based dissociation and formation of bonds in CANs to understand their dissolution behavior. Dissociation and formation of strong bonds through reactive MD modeling of PAN develops reaction pathways for graphite formation in carbonization.

The first research area characterized the interphase structure change in epoxy/graphene nanocomposites with graphene that were multilayered, hydroxyl surface functionalized, and amide surface functionalized at varying surface attachment densities. Interphase structure was quantified through 2-point spatial statistics and/or radial distribution functions. Principal component analysis was used to reduce the statistical representations of the interphase structures in epoxy to their most salient features and ordinary least-squares regression related the principal components to temperature changes during cooling through glass transition and stress values during simulated tensile strain. The first five principal components of 2-point statistical structure representations explained over 95% of the structure variance in bulk epoxy while nearly 99% of structure variance was explained with just two principal components for interphase epoxy structure. The models were able to predict system temperature and stress each with over 90% prediction accuracy and a direct linkage of interphase structure described by principal components to temperature/stress was developed.

The second research area developed a classical molecular dynamics simulation methodology for bond exchange reactions in covalent adaptable networks. Covalent adaptable networks are network polymers that have reversible crosslinks allowing for recycling mechanisms and stress relaxation not obtainable by traditional thermosets. The network degradation mechanism was studied through CAN interaction with ethylene glycol solvent. Increasing the rate of bond exchange reactions was found to increase both dangling end intradiffusion and ethylene glycol interdiffusion. The role of crosslink density and bond exchange reactions was examined through the lens of fractional free volume. The size and shape of individual voids as represented

through a surface area to volume ratio distribution was found to correlate with the overall system stress under tensile strain and stress relaxation. Bond exchange reactions were found to improve the solvent diffusivity when degree of crosslinking was over the gelation point. Under the gelation point the enhanced chain mobility from bond exchange reactions is negligible compared to the chain mobility as a result of a lightly crosslinked network.

The final research area used ReaxFF simulations to study detailed reaction mechanisms and structure development resulting from carbonization of stabilized polyacrylonitrile (s-PAN). Carbonization simulations were performed with varying oxygen content, molecular orientation, and temperature. The oxygen content did not significantly effect the C_5 and C_6 graphitic ring formation. However, higher oxygen content did promote formation of CO and CO_2 gases which lower the final fiber carbon content. The carbonization process was found to shift the graphitic structures toward a random orientation with the fiber axis, regardless of the initial molecular orientation of s-PAN. Higher temperature was found to significantly improve the numbers of graphite rings in the final structure. This confirms experimental results and production methodologies which use high temperature graphitization after carbonization to produce high-modulus fibers with high carbon content and large crystallites. H_2 and N_2 gases were produced most prevalently during carbonization simulations. Detailed reaction mechanism analysis showed that H_2 and N_2 elimination produce carbon radicals that can then form crosslinks with other s-PAN molecules and eventually lead to ring formation and fiber densification.

CHAPTER I

INTRODUCTION

1.1 Thermoset Polymers

Traditionally polymers are divided into two categories based on their behavior upon heating: thermoplastic or thermoset. Thermoplastic polymers soften above their glass transition temperature, T_g, and eventually melt when heated. When cooled they harden and become rigid. Thermoplastics are typically linear or branched chain structures, such as polyethylene. Thermoset polymers harden when heated due to the formation of covalent crosslinks between monomers resulting in a network structure. After this curing process has occurred, thermosets do not melt upon reheating. The structure will degrade at high temperatures due to polymer backbone chain scission. The network structure creates a rigid polymer with strength and dimensional stability at high temperatures, see Figure 1.1. For this reason thermosets are desired in high temperature or high strength applications, such as electronic circuit boards and structural automotive and aerospace parts. Vulcanized rubber and epoxy are two examples of thermosets.

Epoxy polymers consist of two different monomers, referred to here as resin and hardener, which form crosslinks. The resin contains two or more epoxide groups (bifunctional, trifunctional, etc.) which will bond to the hardener forming a crosslinking site. Nitrogen containing hardeners are most desirable as they generally produce the best temperature resistance and mechanical properties in the final cured epoxy. Additionally, aromatic amines have demonstrated superior thermomechanical properties than aliphatic amines. For example, a comparison of temperature resistances between different hardeners showed a roughly 50°C higher thermal resistance for an

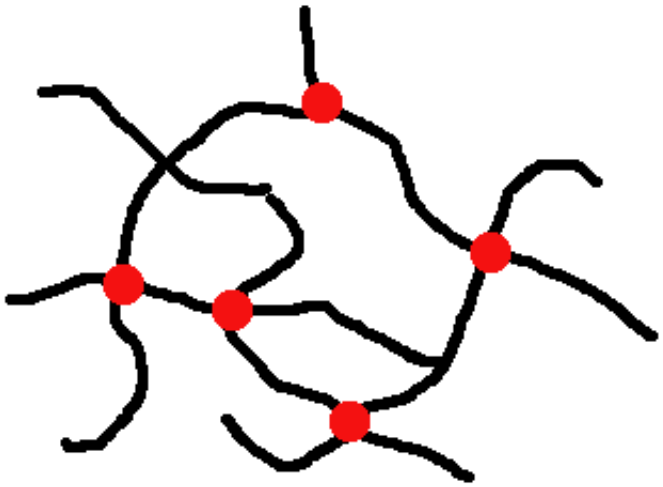

Figure 1.1: Basic morphology of crosslinked, thermosetting polymer. Red dots indicate the crosslinking points.

aromatic amine compared with aliphatic. For the best properties, it is desired that the total number of reaction sites for both resin and hardener are equivalent and that the degree of crosslinking (ratio of the number of crosslinks produced to the number of crosslinks stoichiometrically possible) is high. The crosslinking process is referred to as curing. As seen in Figure 1.2a, curing occurs at elevated temperatures (typically in the 100°C to 200°C range) and involves scission of the C-O bond (activation) of the epoxide end. The activated epoxide carbon will then react with an amine and also form a hydroxyl group. Further, nitrogen containing hardeners can produce secondary amine bonding, as shown in Figure 1.2b. Once the curing process is completed the crosslinked sites are permanent.

A fully formed network polymer has infinite molecular weight at the percolation threshold (or sol-gel transition), according to gel theory. The importance of reaching the critical crosslink density has previously been reported through examining divergence of power-law behavior in the dynamic shear moduli at the sol-gel transition [2]. The rigid network of epoxies creates a polymer with high strength and stability due to the suppression of molecular chain motion and, consequently, long relaxation

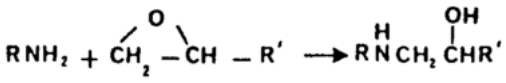

(a)

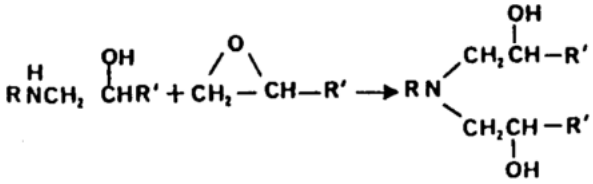

(b)

Figure 1.2: Primary (a) and secondary (b) amine crosslinking reactions in which the oxirane ring in the resin opens and bonds with amine in the hardener [1].

times. The properties of final cured epoxies can vary depending on the resin/hardener system used, the processing parameters, the use of proper resin/hardener ratio, and the cure cycle chosen. Table 1.1 lists general ranges of properties for network (epoxy) polymer.

1.2 Nanoscale Composites

Rising fuel prices have prompted many companies in the transportation industry to pursue material solutions for lightweighting. The desire is to find a material that is both lightweight and high strength to replace traditional, heavy metallic counterparts. Polymeric matrix composites are a class of materials using a filler material surrounded by a matrix. Some of the most commonly known and used is carbon fiber reinforced plastic (CFRP) and glass fiber reinforced plastic. Over the past several decades these materials have seen expanded use in the transportation industry due to their high specific strength and specific modulus. For example, the Boeing 787 Dreamliner passenger jet is over 50% by weight composite materials. CFRP use fabric composed of unidirectional or woven carbon fibers layered on top of each other in specific directions to produce desired properties and is held together by the matrix material. This

Table 1.1: General Epoxy Properties

Property	Value
Tensile strength at break, MPa	27 - 90
Elongation at break, %	3 - 6
Elastic Modulus, GPa	2.4
Compressive Strength, MPa	100 - 170
Flexural Strength, MPa	90 - 145
CTE, x10^{-6}, $\circ$C	45 - 65
Specific Gravity	1.11 - 1.40

stacking produces high strength and stiffness if the loading direction is in the direction of the fibers; however, out-of-plane loading results in a weak material and the potential for delamination, see Figure 1.2. Several solutions have been proposed to increase the out-of-plane loading strength including 3-D weaving of the fabric. With the rise of nanomaterial research polymeric composites containing nanosized fillers, such as alumina particles, clay particles, carbon nanotubes, and graphene have also been used to increase the interfacial adhesion of matrix to fiber and to improve the out-of-plane strength. Graphene and nanocellulose are two promising fillers that are investigated in this dissertation and are summarized in this section.

Graphene is a material composed of a single layer of carbon atoms, as if a carbon nanotube (CNT) was split along a seam and unrolled. Due to the delocalized electrons and pi stacking the in-plane mechanical properties of graphene are some of the highest ever measured, upwards of 500 GPa elastic modulus and 130 GPa ultimate tensile strength. Although these values are produced for a theoretical single layer of graphene with no impurities, it shows the promise of graphene as a high strength material. During the past few decades carbon nanotubes have shown great promise as a filler

material in polymer matrix composites as a way to increase both strength and stiffness [3]. However, the curvature of nanotubes presents issues with obtaining adequate wetting of the matrix material and creating an effective interface between nanoparticle and matrix. However, graphene is a planar structure with large specific surface area allowing for better opportunity for matrix/filler interaction. Additionally, graphene is more easily mass-manufactured driving costs below that of CNT and presenting an opportunity for widespread industrial use.

The best way to ensure enhancement of properties by using graphene as a filler is to create an effective interface so that efficient stress transfer occurs. The large surface area of graphene ensures van der Waals interactions between the matrix and graphene. Furthermore, enhancement of interfacial strength has been shown by creating a functionalized surface. Fang et al. [4] functionalized a graphene surface with amine groups allowing covalent bonding of the epoxy matrix to the graphene nanosheet. They found addition of 0.4% by weight of the modified graphene improved elastic modulus by 60.2%, tensile strength by 54.1%, and fracture toughness by 72.7% compared to the neat epoxy. Many other graphene surface functionalizations have been attempted to improve stress transfer [5]. Although experimental tests have proven the efficacy of graphene as a nanofiller, the polymer architecture at the interface is still difficult to understand through experimentation, as the interphase region is typically on the order of Angstroms or nanometer length scales.

Recently efforts have increased to use cellulose nanocrystals (CNC) as a reinforcing agent in polymer composites. It has the potential to be a sustainable and non-petroleum based alternative to many other forms of fillers. To obtain CNC's, cellulose is typically dissolved in sulfuric acid. The acid attacks the amorphous regions of the cellulose and leaves behind the nanoscale-sized, nearly defect free crystalline regions, as seen in Figure 1.3. NC is typically 3-5 nm wide and 50 - 500 nm in length. The

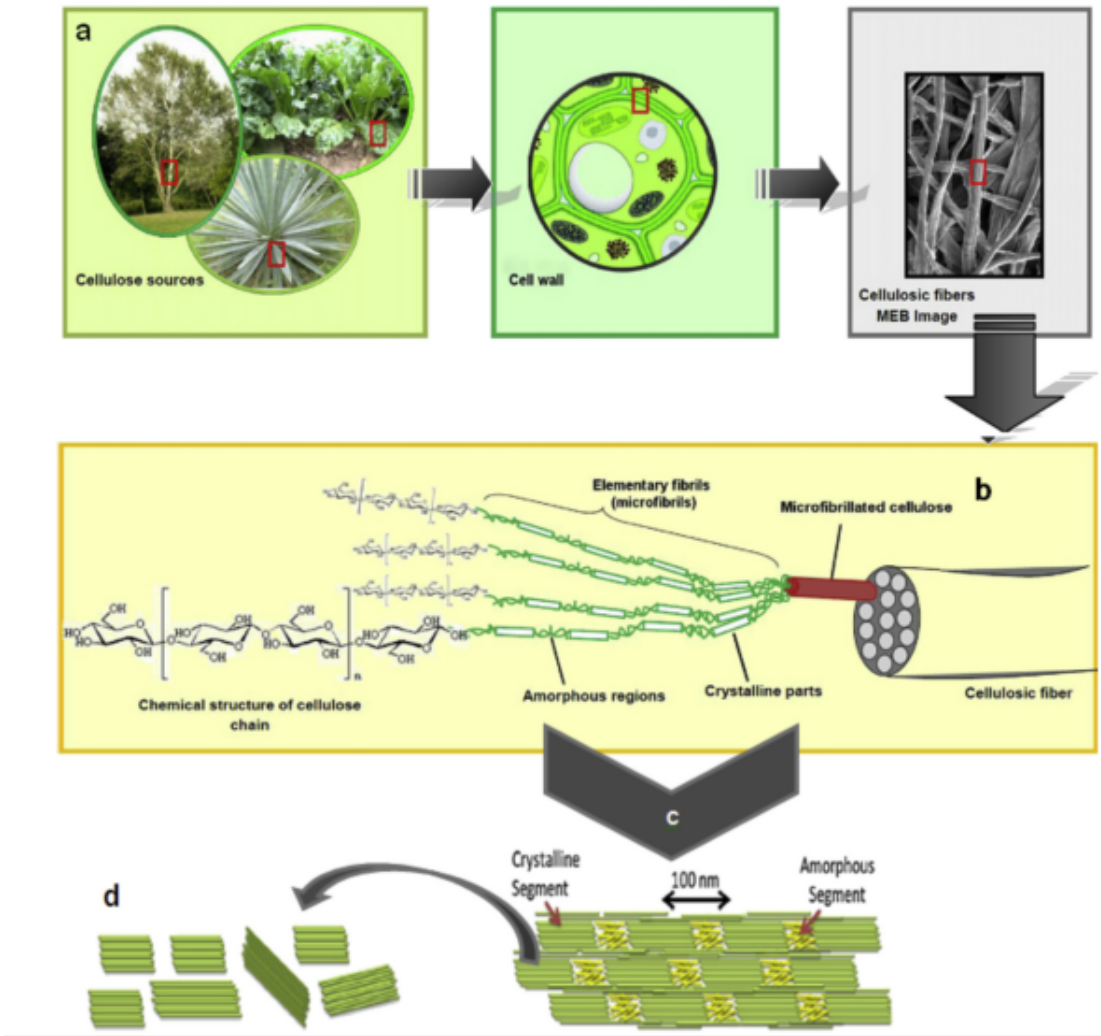

Figure 1.3: Processing route to obtain nanocellulose from wood-based sources [7].

high axial strength and stability is generally attributed to the inter and intra hydrogen bonding [6]; however wide variability in strength is reported due to the various polymorphs of cellulose that exist. The tensile modulus has been reported by various sources to be, experimentally, from 110-220 GPa and tensile strength as 7.5-7.7 GPa from modeling studies. The presence of surface hydroxyl groups in cellulose allows for excellent wetting and hydrogen bonding interaction with hydrophilic polymers, allowing for strong interfacial adhesion. The surface hydroxyl groups also allow CNC to be surface functionalized in different ways in order to be incorporated into a hydrophobic polymer matrix [7, 8].

An example of a biodegradable polymer with property improvement due to the addition of NC filler is poly (lactic acid) (PLA). PLA is a polymer of interest as it is derived from corn and other biomass making it a sustainable, renewable, and biodegradable plastic. Addition of CNC was made as a cost reduction strategy. It was found that inclusion of micro-fibrillated cellulose in PLA increased the tensile modulus by 40% and the tensile strength by 25% [9]. Further, Kamal and Khoshkava [10] found that NC acted as nucleation sites for crystallization in PLA, which improved the rubbery state elastic modulus by 180%. High thermal stability is another characteristic of CNC. Degradation has been reported to occur between 200-300 °C [6, 11]. These properties make nanocellulose a promising and sustainable filler material in polymeric matrix composites.

1.3 Molecular Dynamics Simulation

Studying the effect of different nanofillers on composite properties is a challenging and time intensive experimental problem. The variety of filler types, concentration, size variation of the filler, and functionalization type alone quickly produces an unwieldy number of samples. However, molecular simulation of polymers provides a method to understand fundamental mechanisms difficult to observe experimentally. Simulation methods can be used to efficiently understand behavior of a system at low cost. Polymer systems have been studied using a variety of methods that cover timespans from femtoseconds to minutes and length scales from Angstroms to meters including quantum mechanics [12], molecular dynamics [13], dissipative particle dynamics and Brownian dynamics [14], Monte Carlo methods [15], and continuum mechanics [16]. Figure 1.4 shows the hierarchy of simulation from the quantum to macro scale. Molecular dynamics sits between quantum chemistry methods such as density functional theory and mesoscale methods, such as dissipative particle dynamics. It is thus positioned to be able to provide useful information to help understand

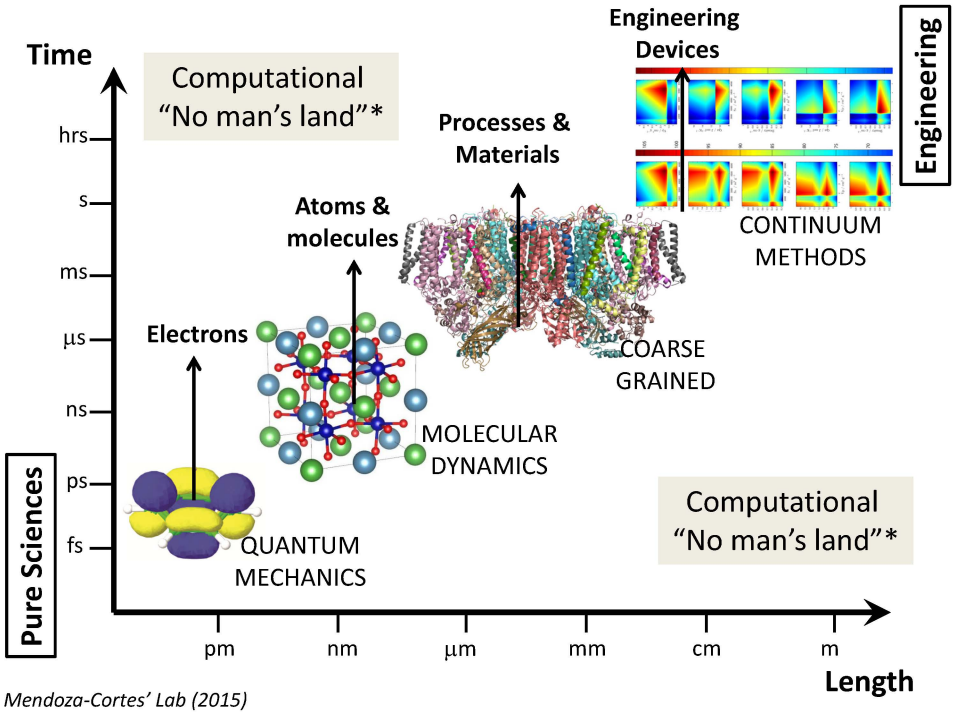

Figure 1.4: Depiction of hierarchical simulation of materials from quantum mechanics to finite element. This dissertation will focus on molecular dynamics.

mesoscale phenomena while using atom level detail. Molecular dynamics simulation is typically in the nanosecond timescale and nanometer length scale. The remainder of this section describes the theory behind these simulations.

Both molecular mechanics (MM) and molecular dynamics (MD) are simulation methods that use forcefield models of molecules to describe the energy and forces of an atomistic system and are often used in conjunction to obtain an equilibrium structure. Systems from hundreds to hundreds-of-millions of atoms have been studied using these methods, including semi-conductors, polymers, metals, and proteins. In both methods, the classical description of the molecule includes a bead-spring model to describe atoms and bonds and a Lennard-Jones description of non-bonded van der Waals interactions. Table 1.2 shows the equations for the Optimized Potential for Liquid Simulation (OPLS) forcefield as an example [17]. Figure 1.5 depicts the bond, angle, dihedral, and improper terms for molecules. Forcefields are commonly

developed using ab initio calculations and then fitting the forcefield model for a wide range of molecules to the ab initio data. This is an iterative optimization procedure that gives a best fit and provides a classical description of molecules.

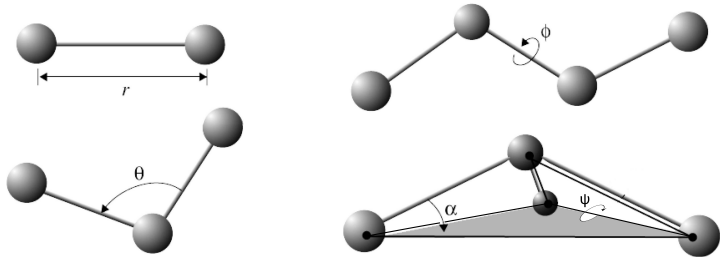

Figure 1.5: Example of bond, angle, torsion, and improper terms used in describing molecular energy.

Forcefields in both MM and MD describe the forces experienced by various atoms and how they interact when bonded (intramolecular) or not bonded (intermolecular) to other atoms. Forcefields are typically divided into classical, or class 1, which include bond, angle, dihedral, and improper terms, and class 2, which include class 1 terms and cross-terms such as bond-angle, bond-bond, angle-angle, etc. Common class 1 forcefields include Dreiding [18], CHARMM [19], and OPLS [20]. Common class 2 forcefields include CFF93 [21] and COMPASS [22]. Additionally, class 3 forcefields have been developed and are described as reactive forcefields, such as Reactive Empirical Bond Order [23] and ReaxFF [24]. These forcefields contain only non-bonded parameters. At each iteration of MM or MD the bond order between atoms is determined by analyzing the local topological and energy landscape. In this way one can model chemical reactions intrinsically.

Molecular mechanics (MM) seeks to arrange and orient the molecular system in the lowest possible energy conformation, taking into account all forcefield descriptors (bonds, angles, dihedrals, impropers, non-bonded interactions). The basic idea of MM is to find the total energy of the system given atomic positions and then calculate the energy derivatives. MM then iterates to decrease the derivative of potential energy

Table 1.2: OPLS Forcefield Equations

Descriptor	Equation
Non-bonded	$E_{ab} = \sum_i \sum_j [q_i q_j e^2 / r_{ij} + 4\epsilon_{ij}([\sigma_{ij}/r_{ij}]^{12} - [\sigma_{ij}/r_{ij}]^6])] f_{ij}$
Bond	$E_{bond} = \sum_{bonds} K_r (r - r_{eq})^2$
Angle	$E_{angle} = \sum_{angles} K_\theta (\theta - \theta_{eq})^2$
Dihedral	$E_{dihedral} = \sum_i \frac{V_1^i}{2}[1 + cos(\phi_i + f_{i,1})] + \frac{V_2^i}{2}[1 - cos(2\phi_i + f_{i,2})] + \frac{V_3^i}{2}[1 + cos(3\phi_i + f_{i,3})]$

toward zero using methods such as conjugate gradient or stochastic descent. At each iteration, atomic coordinates are rearranged to reflect the new lower energy, until the structure is at an energy minimum [25]. Molecular mechanics operates at 0 K temperature. Molecular mechanics is useful for finding the lowest energy conformation of a molecule or system and for initial equilibration. In contrast, molecular dynamics seeks to solve the trajectories of atoms under various conditions using Newton's equations of motion.

The basic scheme for a MD simulation can be seen in Figure 1.6. Initialization of a MM/MD simulation involves giving initial coordinates and velocities of all atoms. In order to avoid inaccurate structure representation the initial conditions should mimic the realistic structure as much as possible, especially avoiding overlapping atoms. Different strategies for obtaining starting configurations and equilibration methods are presented separately in subsequent chapters of this dissertation. After initialization, the first step is to use the forces, described by the forcefield equations, on each atom in the system to update the velocity of the atoms by half of a timestep. The forces are described by,

$$\vec{f}_i(t) = -\nabla_i U(t) \tag{1.1}$$

where $U(t)$ is the total energy described by the forcefield equations. Using the velocity,

the equations of motion can be integrated to predict the position of the atom at the next timestep. After the atom positions have been updated to the next timestep the forces on each atom are recalculated, with the constraints and boundary conditions applied. Finally, the velocity is updated by another half timestep. The time is updated and the process is repeated until the total simulation time is complete. This timestepping algorithm is called the Velocity-Verlet formulation and is used throughout many MD codes. More specifically, the algorithm relates the force vector to velocity and position by

$$\frac{d\vec{v_i}}{dt} = \frac{\vec{f_i}}{m_i} = \frac{d^2\vec{r_i}}{dt^2} \tag{1.2}$$

Using Taylor expansion in the Verlet algorithm with the terms t and $t - \Delta t$ we can find $r_i(t + \Delta t)$ if we know $r_i(t)$ and $r_i(t - \Delta t)$. In this way we get,

$$r_i(t_0 + \Delta t) = -r_i(t_0 - \Delta t) + 2r_i(t_0) + a_i(t_0)\Delta t^2 + O(\Delta t^4) \tag{1.3}$$

MD simulations are performed under various ensembles, including the canonical

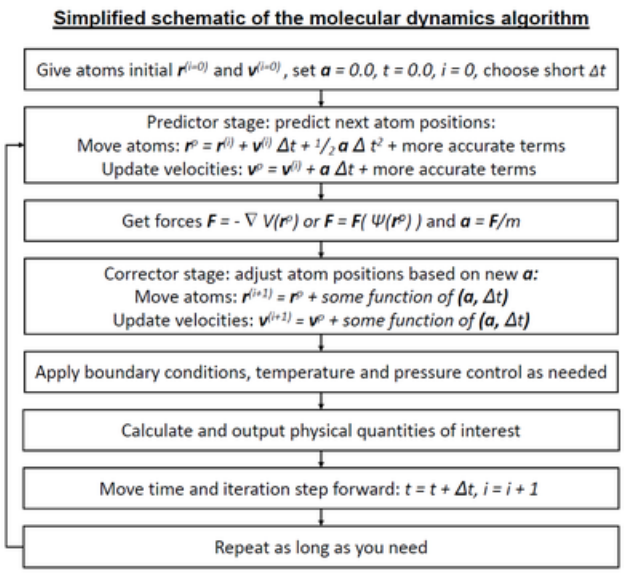

Figure 1.6: Flowchart showing the basic scheme to perform molecular dynamics.

(NVT, constant volume and temperature), isothermal-isobaric (NPT, constant pressure and temperature), and microcanonical (NVE, constant volume and energy),

where N is the number of atoms. Various algorithms exist to keep the desired thermodynamics variables constant, including Andersen [26], Berendsen [27], and Nose-Hoover [28, 29]. For example, the Berendsen thermostat controls temperature through weak coupling of the system to an external bath which adds or removes energy to the system. By contrast, Nose-Hoover algorithm adds an extra degree of freedom representing a heat bath to the system energy function. This dissertation uses Nose-Hoover and Berendsen.

The NVE ensemble does not hold temperature or pressure constant and is thus suitable for already stable systems. However, when combined with a separate temperature integrator (in LAMMPS "fix langevin") the NVE ensemble can be useful to creating equilibrated structures without using a MM method. The NVT ensemble describes a system in which heat exchange occurs with some external heat bath to maintain constant temperature. The bath adds or removes heat from the system by adjusting atom velocities at regular time intervals. The NPT ensemble adjusts the pressure of a system through volume change and according to a pressure bath. The NPT ensemble is useful in equilibration to an appropriate system density.

Due to the small number of atoms in MD and in order to get a more accurate representation of bulk properties periodic boundary conditions are often employed, as seen in Figure 1.7. Periodic boundaries allow the atoms to interact with image atoms across the boundaries of the simulation box so that it is as if the material is continuing on ad infinitum. Combining periodic boundary conditions with a deformation theoretically allows MD to generate bulk material properties while understanding the molecular topology details during deformation. In reality, unrealistically high strain rates and the absence of defects typically results in deviation from macroscale properties seen experimentally. MD simulation is capable of measuring properties like T_g by cooling or heating, mechanical and rheological properties by stretching or shearing the simulation box, and various thermodynamic properties. As an example the stress

and strain of a system can be measured through affine deformation of the simulation box along an axis. The stress calculation for the entire system is given by,

$$\sigma_{ij}^{a} = -\frac{1}{V^a}[m^a v_i^a v_j^a + \frac{1}{2}\sum_b r_i^{ab} f_j^{ab}] \tag{1.4}$$

where, V^a is volume, v^a is the velocity in the i and j directions, N_p is the number of particles, m^a is the mass, r_i^{ab} is the pairwise distance between atoms a and b, and f_j^{ab} is the force between atoms a and b. Summing this equation over all atoms yields the overall system stress.

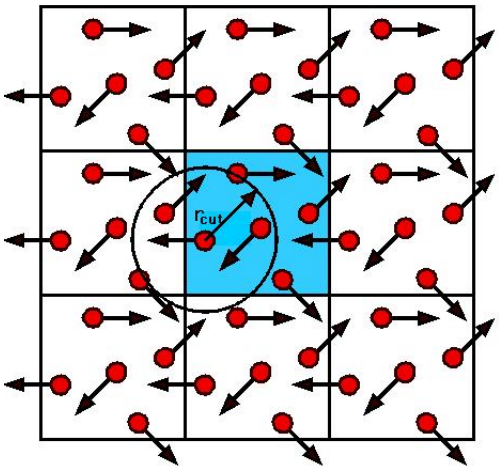

Figure 1.7: Example of periodic boundary conditions in which the simulation box is repeated on all boundaries so that the system resembles the bulk. Note for example if an atom moves out of the left side of the simulation box it will re-enter at the right side with the same velocity.

Many different strategies and codes, commercial and open source, are available to perform atomistic simulations. Throughout this research Avogadro [30] is used to generate individual initial monomer configurations, PACKMOL [31] is used to populate initial simulation boxes with monomers, LAMMPS [32] simulation package is used for atomistic simulations, and VMD [33] and OVITO [34] are used to visualize the simulation results. All these packages were chosen for their open source licenses and extensive use within the material simulation community. All simulations are performed on the Windu Computer Cluster in the Center for Interactive and High Performance Computing within the College of Computing at Georgia Tech.

1.4 Research Motivation

CFRP have been used in the defense industry since the 1960's after the discovery of high strength carbon fibers in the 1950's. However, the last two decades have seen a rapid increase in the use of these materials in the commercial sector, specifically automotive and aerospace, in an effort to reduce weight and improve fuel economy while maintaining structural integrity. The past few decades have also seen increased efforts to mitigate the environmental impacts of non-recyclable plastics, such as epoxies.

The increased use of CFRP and the rise of nanotechnology have led to the development of new nanocomposite materials. The number of different fillers and modifications in size, shape, and functionality that can be applied lead to a challenging, expensive, and time consuming experimental problem. Computational materials science allows efficient study of these materials to aid in targeted experimentation and to reduce the time needed for development. The progress in the machine learning field also provides methods with which to increase our understanding of the data generated by simulation and to aid in the optimal design of the filler materials within the composite. This research is well aligned with the goals of the Materials Genome Initiative [35], which states:

> The ultimate goal is to generate computational tools that enable real-world materials development, that optimize or minimize traditional experimental testing, and that predict materials performance under diverse product conditions.

The main goal of this research will be to use molecular dynamics simulation to analyze the (1) interfacial atomistic structure and mechanical properties of a traditional epoxy/graphene system with different surface functionalities, (2) dissolution (recycling) mechanism and thermomechanical properties of covalent adaptable networks (CAN), and (3) carbonization reaction mechanism of polyacrylonitrile (PAN)

fibers. Each of these projects will use different methods of modeling of chemical reactions to elicit structure-property relationships. A new method for characterizing atomistic structure will be presented for the traditional epoxy/graphene system. Non-bonded surface interactions are compared to bonded surface interactions in epoxy/functionalized-graphene composites with bonds created through a distance-based bond formation method in classical MD. Simulations of CAN polymers further the mechanistic understanding of recyclability and recoverability in these materials and shed light on the role of bond exchange reactions on dissolution and mechanical properties. Transesterification reactions in these simulations are modeled through distance and energy based bond dissociation and formation of bonds in CANs. ReaxFF simulations of PAN carbonization will improve the knowledge of reaction mechanisms that occur during carbon fiber production. Dissociation and formation of strong bonds is achieved through reactive MD modeling.

CHAPTER II

LITERATURE REVIEW

2.1 Molecular Dynamics Simulation of Epoxy and Nanocomposites

Several works have investigated the mechanical and thermal properties of epoxies and composites using molecular dynamics simulation. Since epoxies are amorphous a challenge in this field is the generation of a realistic initial structure. Successful Monte Carlo techniques for generation of initial amorphous structure have previously been developed. Using configurational bias Monte Carlo based on rotational isomeric state (RIS) theory provides a way to build up a chain structure atom by atom while incorporating the influences from surrounding non-bonded atoms as well [16, 36]. Coarse-graining and reverse mapping have proved successful and efficient at creating equilibrium structures [37]. Improvement of computing resources has allowed for using MD simulation as a tool for structure generation using simulated polymerization techniques. In general, this process involves packing a simulation box with individual monomers and over the course of a MD simulation creating bonds between monomers that become close to one another, basic scheme seen in Figure 2.1. Research into structure generation has grown to include combinations of techniques, for example, the LAMMPS simulation package includes a Monte Carlo swapping algorithm for building polymer structures.

Several researchers have addressed the issues surrounding formation of glassy polymer structures, including charge equilibration [38], reaction kinetics for primary and secondary bonding [39], and system stability as a function of the number of crosslinks created [40]. Epoxies, for example, are characterized by high T_g and long relaxation

times making it difficult to overcome steric hindrances on the short timescales of MD. In general, compression and relaxation and using both high pressures and high temperatures have been shown to effectively overcome the large energy barriers and speed up the process of obtaining equilibrium [41, 42]. The general framework consists of simulations of high temperature NVT, final system temperature NVT, final system temperature NPT. This scheme is repeated several times gradually increasing the pressure in the NPT step to compress the system, then gradually decreasing it to atmospheric pressure. Abbott et al. [43] created a simulation scheme to solve many of the individual issues previously investigated and that work is recreated and re-purposed throughout this dissertation.

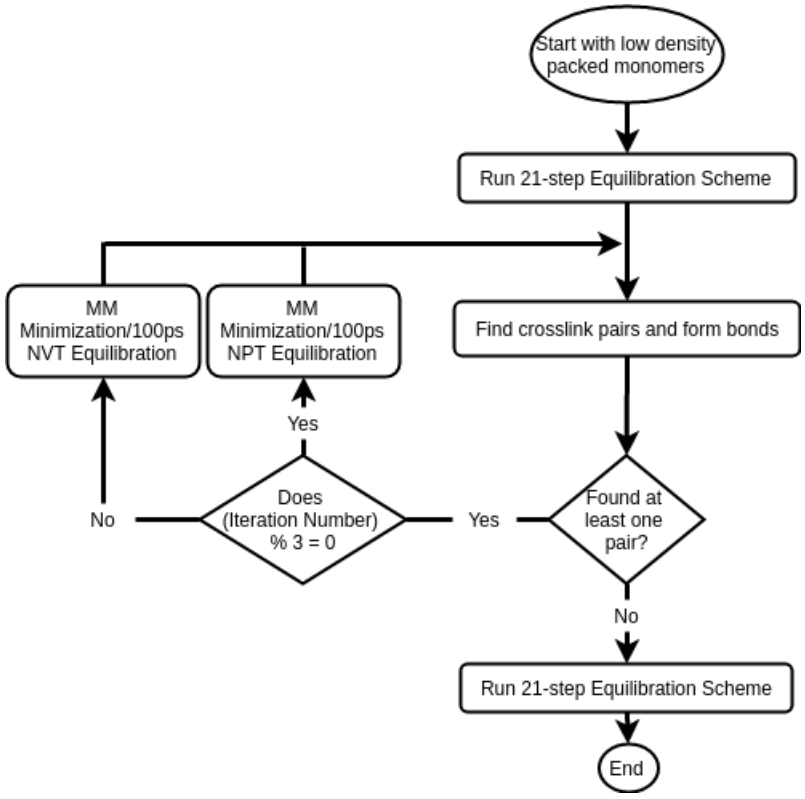

Figure 2.1: Flowchart showing the crosslinking process for a resin/hardener system. This is a general scheme used in many works and also throughout this dissertation.

An important starting point in studying the behavior of nanocomposites is full understanding of the behavior of the epoxy matrix material. Mechanical and thermal

properties have been studied at length using MD. For example, Bandyopadhyay et al. [40] studied the effect of crosslink density on the mechanical properties of an EPON-862 and DETDA epoxy system. The researchers found that with increasing crosslink density (ranging from 54% to 76%) the T_g and stiffness increased and coefficient of thermal expansion (CTE) decreased. An extensive review by Li et al. [44] summarizes the use of molecular dynamics for model generation and for extracting thermomechanical properties of thermoset polymers. Molecular dynamics can provide chemical level details describing the structure change that occurs during the crosslinking process, cooling through glass transition, and straining a system. The authors present a method for determining glass transition temperature through NPT cooling simulations. The rate of density, or specific volume, change is different above and below the glass transition, as seen in Figure 2.2. Therefore, plotting the specific volume versus temperature and performing a piecewise linear fit with two regions will find the glass transition temperature at the crossover point (the coefficient of thermal expansion can also be obtained from the slope of these two regions). Furthermore, it was noted that T_g will typically be higher in MD simulations due to the faster cooling rate, often 10 K/ns or higher, than achievable experimentally, often 10 K/min. However, the authors present a correction derived from the William-Landel-Ferry equation that predicts a 3 K/decade offset from the cooling rates, and this offset will be taken into consideration throughout glass transition studies in this dissertation. Mechanical properties of molecular systems are typically obtained through either through the static [45] or dynamic [46, 27] method. In the static method a small strain is applied to the system followed by a MM energy minimization. The second derivative of the potential energy with respect to the strain, after minimization, leads to the stiffness matrix. The dynamic method involves affine deformation of the simulation volume and plotting the stress/strain curve. Again, mechanical properties in molecular dynamics simulation often vary from experimental results due to

the high strain rates in MD, lack of defects, and the inability to implicitly model bond breakage. Recently, attempts to use reactive forcefields to model bond breakage during strain of a thermoset system have been made [47]. These results show accurate response to experimental studies after applying appropriate interpolation to account for varying strain rates. Additionally, the reactive forcefield was able to capture two characteristic yield events, often seen experimentally but not in simulation.

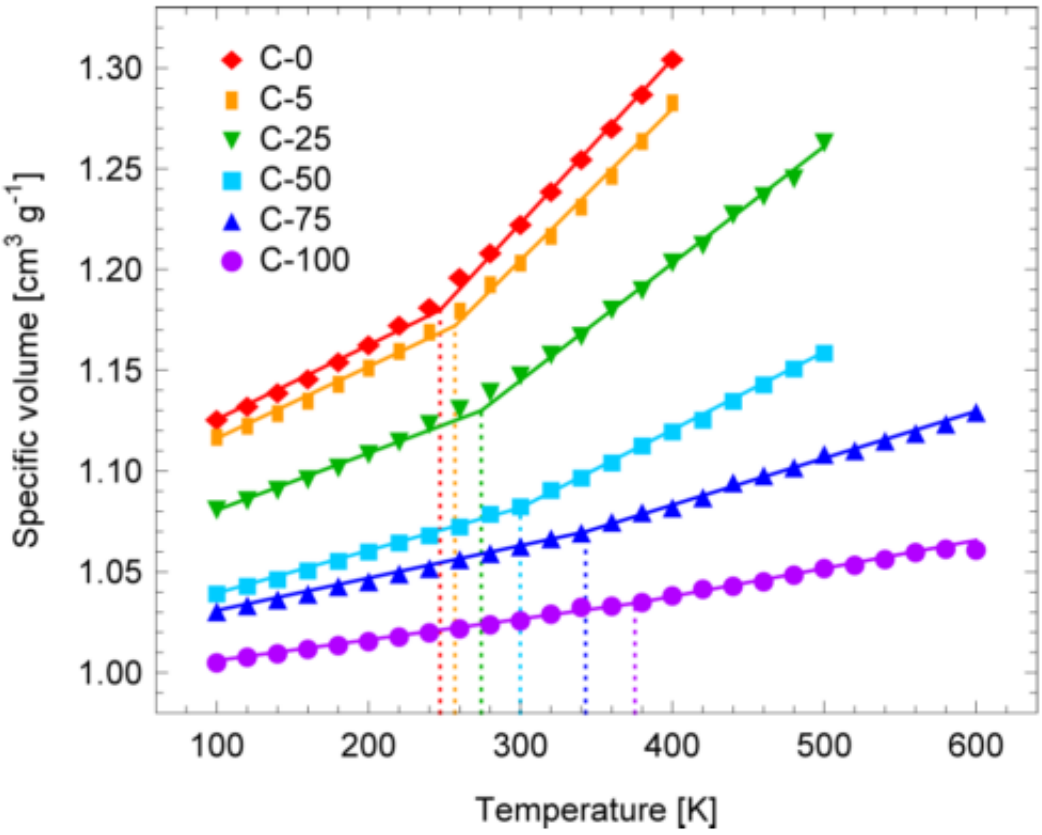

Figure 2.2: Graph showing the relationship between crosslink density and glass transition temperature using changes in specific volume with temperature [48].

The mechanism for physical and chemical aging has also been studied. The physical aging mechanism was found as a conformational change of the polymer that ultimately results in a volume reduction [49]. By establishing a linear relationship between enthalpy change and volume change and using experimental data to establish an equation for change of enthalpy as a function of aging time, one can relate

the change in molecular simulation volume to the aging time. This allowed for a molecular model to have the volume changed accordingly to reflect the epoxy system at a certain aging time.

The study of hygrothermal or environmental aging has also been attempted at the molecular level. However, the short timescales of molecular dynamics make simulating chemical aging challenging. Li [50] studied the effect on mechanical properties with varying amounts of bond scission manually created based on oxidation and hydrolysis reactions. The density of the simulation was found to increase with initial bond cutting and then decrease with higher percentage of broken bonds. This was attributed to small molecules initially being able to diffuse into void space and increase compactness, however with further creation of small molecules the network becomes lightly compact and free volume space increases. Young's modulus and T_g was found to drop off significantly with the percentage of broken bonds. Clancy et al. [51] studied the effect of moisture content and temperature on mechanical properties of epoxies. Water molecules were inserted into void areas within the epoxy structure after it had been equilibrated. It was found that elastic moduli generally decreased with increasing moisture content, decreasing degree of crosslinking, and increasing temperature. The chain scission process was modeled by varying degree of crosslinking. Yao et al. [52] used MD to study the mechanism of hygrothermal aging. Similar to [50] they used random chain scission to mimic varying degrees of hydrolysis and random insertion of up to 5 wt% water molecules, with no chain scission, to mimic plasticization. Using an epoxy adhesive model the researchers found hydrolysis decreases T_g, modulus, and max stress while plasticization reduces T_g but increases modulus and max stress.

Of interest to researchers in the last several decades has been the study of nanocomposite materials and especially the interfacial relationship between matrix and filler. Nanocomposites can be classified as those materials which contain fillers on the nano

length scale. At these length scales the surface area to volume ratio of most fillers begins to increase rapidly. As a consequence, low weight percentage of fillers are needed in the matrix to produce improvement of composite mechanical properties and there are less defects within the filler materials themselves. In order to realize the benefits of the near pristine fillers, the matrix and filler must interact favorably to allow efficient stress transfer at the interface. By using energy and density maps, spatial correlations, tensile and shear strain, and other simulation techniques and analyses MD is able to characterize interfacial properties of nanocomposites.

Carbon nanotubes (CNTs) are a popular nanocomposite filler and have been studied extensively in molecular dynamics. Lu, et. al. [53] used pull-out simulations of CNTs within a polyethylene matrix and CNTs surrounded by other CNTs in order to estimate the interfacial strength in these composites. They used the AIREBO forcefield to implicitly model bond breakage and crack initiation at the interface and found the interfacial energy, and consequently pull-out strength, is proportional to the CNT chiral number but does not depend on CNT length. However, Arash et al. [3] found that an increase of 3x the aspect ratio led to a 75% improvement in tensile modulus for a CNT/polyethylene composite. CNT in amorphous carbon matrix was studied to analyze the effect of filler orientation, content, type, and functionalization on mechanical properties [54]. Formation of crosslinks with the amorphous carbon matrix was found to increase transverse modulus and specific strength and was attributed to the increased load transfer. Axial specific modulus suffered slightly due to CNT damage from crosslink formation. Formation of a graphitic structure in the interphase during equilibration suggested that CNTs acted as nucleation sites. Interphase structure development in the presence of CNTs has been documented experimentally as well [55]. It has been found that presence of CNTs nucleate crystalline regions in linear polymers and align those regions perpendicular to the axial direction of CNT. This leads to compact polymer packing and mechanical property improvement in

the interphase. Figure 2.3 provides a transmission electron microscope image of the interphase region in a CNT/epoxy composite.

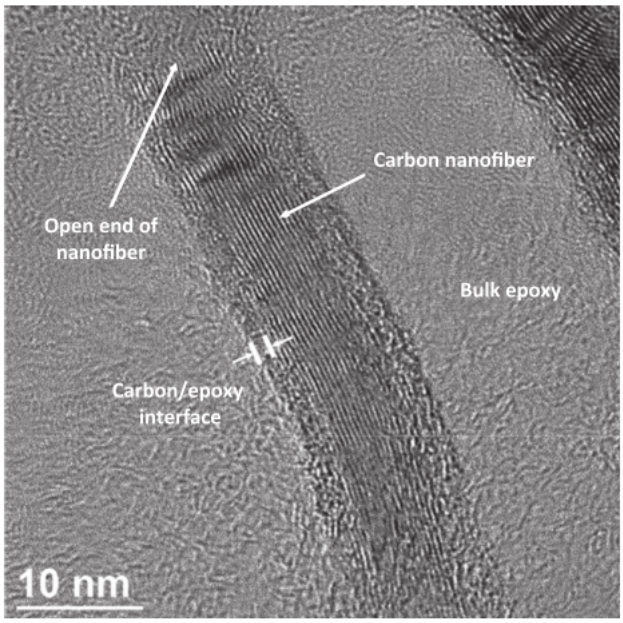

Figure 2.3: TEM image showing structural difference between interphase region and bulk epoxy in carbon nanotube composite [56].

Graphene is a 2D lattice of carbon atoms that has the same structure as an unzipped, unrolled CNT. Graphene's 2D structure gives it very high surface area to volume ratio. The lack of curvature creates better wettability and interaction with matrix materials than typically seen with carbon nanotubes. MD simulations of graphene and epoxy nanocomposites have shown the interfacial region to be around 7 Å to 10 Å using density change as the key metric [57]. Experimentally, transmission electron microscopy has found interfacial region of epoxy/CNT composites to be about 10 Å [56]. Using non-functionalized multi-layer graphene (MLG) sheets atomistic simulations proved that the interfacial adhesion energy, as measured by

$$U_{interface} = (PE_{resin} + PE_{MLG} - PE_{composite})/A \tag{2.1}$$

is larger between graphene faces and epoxy rather than graphene ends and epoxy [57]. Figure 2.4 shows the stress and strain of bulk epoxy and an epoxy/multilayered

graphene composite. It clearly shows the composite with higher yield stress and modulus than the bulk epoxy providing evidence that the filler acts as a reinforcing agent with effective load transfer. The effect of crosslink density on the mechanical

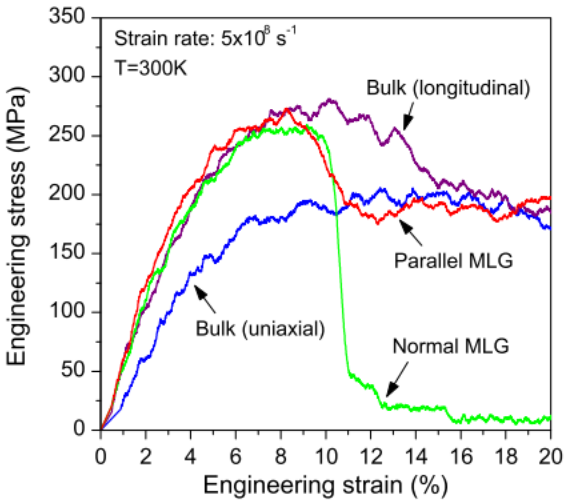

Figure 2.4: Stress/strain curve of multilayered-graphene/epoxy nanocomposite and bulk epoxy simulation [57].

properties of the composite system was also studied [56]. The researchers determined the bulk epoxy material was amorphous while the interphase region exhibited a structure, determined by measuring the mass density as a function of distance from the graphene sheet face. The interface had a higher residual stress and potential energy likely leading to failure at the interface rather than the bulk epoxy.

Liu et al. did a comprehensive study to examine the toughening mechanism of graphene-polymer nano-composites using atomistic simulation [58]. Larger polymer chains with higher numbers of chain entanglements increase toughness, greater volume fraction of graphene sheets increases the interaction energy through toughening a rubbery matrix, the wrinkled structure of graphene increases toughening likely due to a larger interfacial area for interaction with the matrix, and the planar structure of graphene contributes to greater toughening due to improved interfacial interaction compared to the curved surfaces of CNTs or C60 bucky-balls. Rahman and Foster

[59] further studied the deformation mechanism of graphene sheets in amorphous polyethylene. By varying the distance and orientation of the graphene sheets the authors were able to investigate the effect of spatial arrangement of graphene sheets on elastic properties using MD. Contrary to previous studies, Rahman and Foster utilized the reactive AIREBO forcefield to account for bond breaking in the deformation. The authors concluded that a clustered, randomly oriented arrangement of graphene sheets improved the performance greater than well spaced or multilayered sheets. This can be attributed to overlapping spheres of influence so that a greater, non-local portion of the polymer matrix is affected by the graphene. They also documented the evolution of voids, crazing, and straightening of the polymer matrix during plastic deformation and determined voids grew in the direction of deformation. Additionally, small voids were found in the equilibration stages near/in the interphase region likely from a reduced polymer mobility in the vicinity of the graphene sheet

A graphene nanocomposite system will have an optimal volume fraction that will allow non-local interaction throughout the structure. The issue is getting to that volume fraction while ensuring graphene is well-dispersed. Rahman and Haque [60] studied the influence of graphene nanoplatelet aspect ratio, dispersion, and concentration on the stress-strain response of the cross-linked epoxy (EPON862/TETA) composite. The authors evaluated the cohesive force (tensile) and pullout force (shear) by looking at the change in interaction energy between the filler and the matrix. From radial distribution functions they found that the maximum concentration of atoms occurred at about 4 Å from the graphene surface, molecular energy increases with increasing strain (deformation), and, again, the well-dispersed system shows greater elastic modulus improvement than a layered graphene system.

In order to improve the stress transfer and aid in dispersion of graphene within epoxy various functionalizations of a graphene sheet have been investigated. These different approaches are summarized in numerous reviews [5, 61, 62, 63, 64]. Both

covalent and non-covalent approaches have been attempted as seen in see Figure 2.5. Non-covalent approaches use van der Waals, hydrogen bonding, and physical inter-

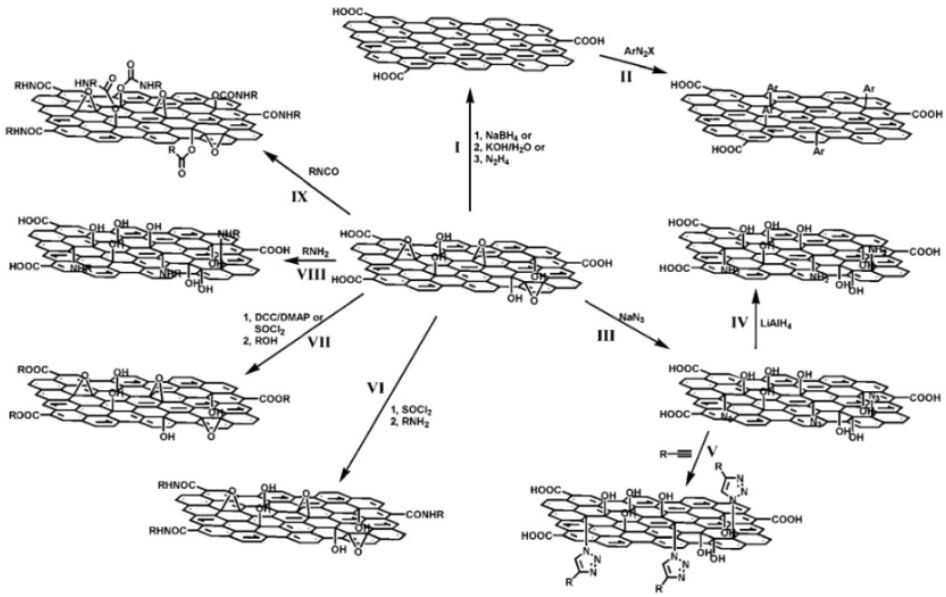

Figure 2.5: Image showing multiple types of graphene functionalization possibilities [65].

actions to improve the load compatibility while covalent approaches directly bond the matrix to graphene. Some common attachments include hydroxyl, epoxide, and amine groups. As an example, researchers have successfully grafted poly(vinyl alcohol) (PVA) onto graphene oxide (GO) by reacting the hydroxyl groups of PVA and carboxylic groups of GO. Grafting polystyrene chains to the surface of GO resulted in a 15°C increase in T_g, 57.2% increase in modulus, and 69.5% increase in tensile strength. Non-covalent functionalization has also been studied and attempts to exploit π interactions. As an example, GNPs with pyrenebutyric acid (PBA) functional groups and dispersed in epoxy increased the storage modulus by 100% relative to neat epoxy. Functionalization of the graphene sheet introduces defects which may reduce the improvement from the filler. Therefore, it is desirable to find the optimal attachment density that creates efficient load transfer while also capturing the benefits of graphene filler.

2.2 Covalent Adaptable Networks

Thermosets are desired in applications requiring strength and dimensional stability at high temperatures. For example, many carbon fiber reinforced plastics are made with thermosets, such as epoxy, in order to create high strength, low weight structures. Although thermosets are optimal for these applications, the creation of permanent, covalent crosslinks makes recycling and reprocessing of these materials very challenging. Mechanical recycling strategies include grinding and pulverizing to create powdered fillers or fibrous products. Thermal processes include combustion, pyrolysis, or fluidized bed processes. The inability to efficiently recycle epoxies also leads to difficulty in recovering any fillers if the epoxy is used as matrix in a composite material. Rising plastic levels in landfills and increased use of epoxy materials are driving the need for a new solution strategy to recycling of these materials [66].

Recent discoveries have created thermosets with reversible crosslinks called covalent adaptable networks (CAN), or more broadly dynamic covalent bonding systems. These novel polymer systems can flow and be reprocessed, degraded to their individual monomeric components, welded, or dissolved in solvent depending on the polymer chemistry used. Dynamic covalent chemistry systems can be broadly classified into systems in which exchange reactions take place and the total number of reversible bonds remains fixed, such as transesterification reactions, and systems in which new covalent bonds are created or existing bonds are broken, such as addition-fragmentation reactions. Systems have been proposed in which the dynamic bond is C-C, C-O, C-N, and C-S [67]. These reactions require a stimulus/catalyst for reactions to occur or to stop the reaction process. This has the benefit of easily tunable reactions. The catalyst is often ultraviolet light [68], heat [69], or a pH change [70].

Due to the chemistry of CANs they exhibit properties on a spectrum between a thermoplastic and a thermoset polymer [72]. Mechanical relaxation in thermoplastics occurs through interdiffusion of polymeric chains. The chains only experience

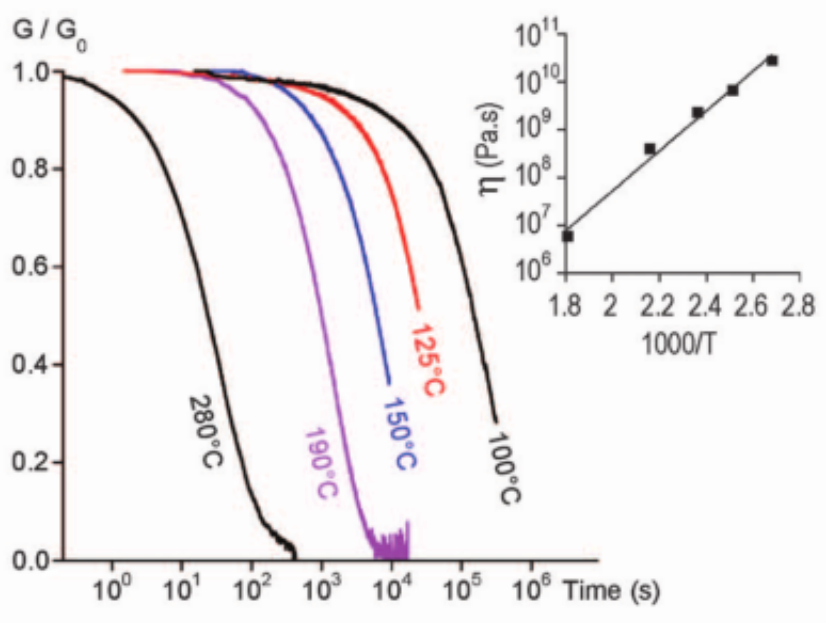

Figure 2.6: Stress relaxation graph for a CAN at different temperatures. Increasing temperature accelerates the relaxation process [71].

physical interactions with other chains and thus given enough time can slide past one another and rearrange into a thermodynamically favorable state. Thermosets have infinite molecular weight once crosslinked beyond their gel point. This means that a thermoset will not have a relaxation time as chains are constrained by the chemical crosslinks. CANs are chemically crosslinked and see similar property dependence on crosslink density. However, CANs will show relaxation behavior when reversible reactions are triggered. This invariably leads to the conclusion that crosslink density is a critical determination for relaxation behavior. Higher crosslink density will give higher modulus and T_g in thermosetting polymers and will produce more exchange reaction opportunities per unit time in CANs. However, higher crosslink density will also restrict molecular movement more than a lower crosslink density which will hinder stress relaxation behavior. Additionally, researchers have studied the impact of temperature on the relaxation behavior in CANs and have found that higher temperatures yield faster relaxation rates, as seen in Figure 2.6.

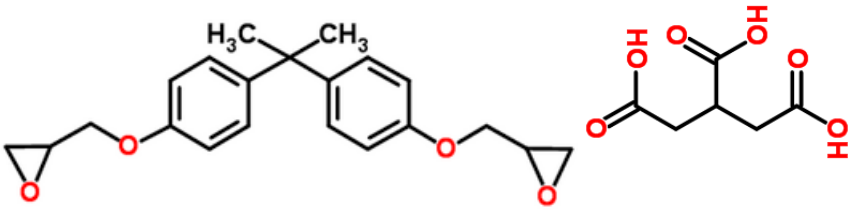

(a) (b)

Figure 2.7: DGEBA (a) and Tricarballylic acid (b) monomers used in the creation of the covalent adaptable network.

This work will focus on the covalent adaptable network system designed in [71] in which a transesterification reaction, or bond exchange reaction (BER), allows for structure relaxation upon heating of the material. This system uses a diglycidyl ether of bisphenol A (DGEBA) monomer and a tricarballylic acid crosslinker, seen in Figure 2.7. The crosslinking reaction in this system involves the opening of the epoxide ends on the DGEBA and crosslinking of the secondary carbon to the open hydroxyl groups on the tricarballylic acid. After the crosslinking process, the transesterification reaction involves forming a bond between a hydroxyl group in the DGEBA and the carbonyl on the tricarballylic acid, then breaking the bond with the currently bonded ether oxygen creating a new hydroxyl group on the DGEBA monomer. The scheme can be seen in Figure 2.8. These exchange reactions, triggered by heat and presence

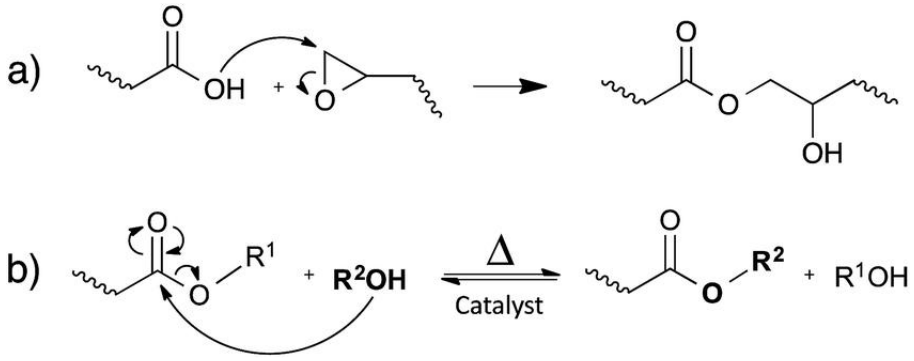

Figure 2.8: Schematic of the a) crosslinking reaction and b) transesterification (BER) reaction assuming presence of catalyst.

of a catalyst, allow the structure to rearrange and relax. Yu et al. were able to tune the mechanical and thermal properties of these materials by using different types of hardener. For example, the T_g varied between approximately 30 and 63 °C when using a fatty acid versus a glutaric anhydride hardener [73]. These materials have shown reprocessing capabilities through studies in which they were repeatedly pulverized, heated and welded, and mechanically tested. Throughout four of these cycles the modulus decreased only slightly, strength decreased roughly 50%, and max strain decreased from 143.3% to 91.8%. However, after a six hour heating cycle the sample was nearly repaired and exhibited similar behavior to the fresh sample [74]. Recent work has shown the dissolution behavior of these materials in ethylene glycol in order to recover CFRP composites made with these CANs. It was found that CAN blocks soaking in EG were able to be completely dissolved in about 160 minutes at 180°C. When dissolving a CFRP composite the carbon fiber was able to be recovered with near no detriment to mechanical properties within the margin of error [75].

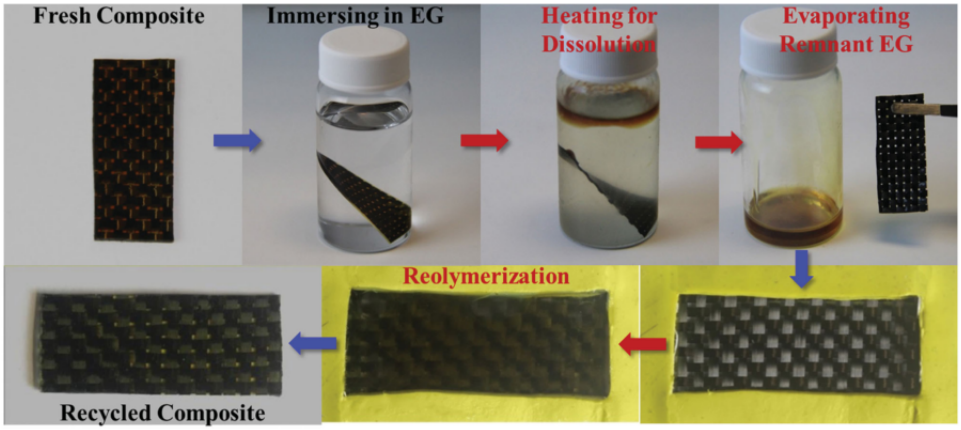

Figure 2.9: Dissolution process to recover carbon fiber, and reform composite material using dissolution of CANs [75].

Computational studies of these materials have been attempted both at the continuum and atomistic levels. At the continuum level the exchange reaction process was modeled by allowing chains to reform and decompose throughout the loading process and through coupling the total elastic strain energy from the microscopic

chain reactions to the macroscopic relaxation behavior [76].

Molecular topology details would be helpful to understand certain phenomena such as welding, free volume distributions, or dissolution behavior. However, modeling these materials with classical molecular dynamics is non-trivial due to the continuous bond breaking and reforming. A hybrid QM/MD approach could be employed such as Car-Parinello, however this would severely limit the timescale available to study these materials. A reactive forcefield with implicit bond formation/breakage could be employed however would need to be parameterized for these specific reactions and would suffer from the small simulation size and length scales achievable. At least several nanoseconds of simulation would be required to observe stress relaxation behavior.

Recently, researchers developed a scheme to model the BER reaction process in classical molecular dynamics that uses a distance based criteria for forming bonds, similar to the crosslinking mechanism described in section 2.1. The flowchart can be seen in Figure 2.10. This scheme has the benefit of allowing large system sizes and long simulation times while allowing tuning of the time between bond searches to match correct stress relaxation behavior. In one study, the elastic modulus, measured at various times throughout a 20 ns simulation, proved the relative stability of mechanical properties throughout the BER process. Additionally, the stress relaxation time was estimated as 3500 ps from straining the simulation box to 80% at 450 K, running the BER reaction scheme, and measuring the stress as a function of time throughout a 10 ns simulation. The graph was then fitted using a standard negative exponential decay function [77]. Further study into the welding behavior of these materials has revealed a basic Fickian diffusion process and given enough time the original modulus is obtained in the newly welded material. It was determined that a lower crosslink density contributes to a shorter welding time due to increased free volume and that increased entanglement leads to decreased diffusivity of polymer

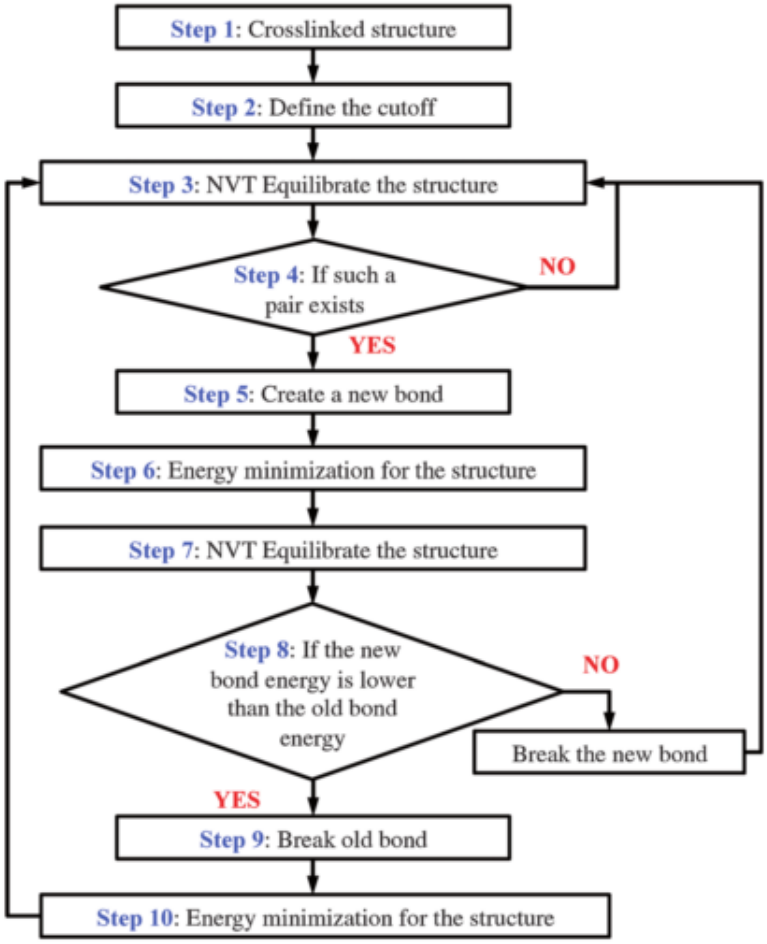

Figure 2.10: Flowchart showing the BER reaction process used during classical molecular dynamics simulations of CANs [77].

chains [78].

2.3 Polyacrylonitrile Pyrolysis and Simulation

2.3.1 PAN Fiber Processing

Due to rising fuel prices the past several decades, the transportation industry has been pushing to lightweight vehicles and aircraft. This has naturally led to increased use of polymer matrix composites, such as carbon fiber reinforced plastic (CFRP). Carbon fiber has the benefit of directional properties and high specific modulus allowing efficient, tailored product design and properties. Research has been ongoing to understand overall composite design and also improve mechanical properties of the

carbon fiber itself.

The process of creating carbon fibers is well studied [79, 80] and is summarized in Figure 2.11. The main precursor used is polyacrylonitrile (PAN). The first step involves spinning the PAN precursor into a fiber, typically with gel or electro spinning. After spinning, the PAN fiber undergoes oxidative stabilization at approximately 200-300 °C. During this process the fiber is oxidized and the chains also crosslink creating a denser stabilized-PAN (s-PAN) fiber with a ring structure (through dehydrogenation and cyclization). The cyclic structure of the s-PAN improves fiber stiffness and allows for further heating during carbonization. Wang et al. studied the effect of atmospheric oxygen content on the final s-PAN structure [81]. The stabilized fiber showed a critical oxygen content of around 11% regardless of the atmospheric concentration. Additionally, a highly concentrated atmosphere did not alter the degree of cyclization that occurred in the fiber; however, degree of cyclization was directly proportional to oxygen content in the fiber. This suggests an oxygen deficient atmosphere/fiber could inhibit cyclization reactions creating a skin-core structure and poor carbon yields.

After stabilization, the s-PAN fiber undergoes carbonization in which the temperature is ramped to anywhere from 1000 to 3000 °C in an inert (typically nitrogen) atmosphere. This high temperature carbonization produces mostly non-carbon gaseous molecules, leaving a polymer chain of carbon molecules. During this stage, the s-PAN chains begin to crosslink and form basal planes of graphite structure. A fourth step is sometimes included, called graphitization. This process is the same as carbonization simply at higher temperatures. Further heating after carbonization increases the alignment and graphitization of these molecules along the fiber axis, improving mechanical properties. The carbonization stage can occur at various temperatures, depending on end use of the fiber. Typically, lower temperature carbonization produces lower modulus fibers.

One way to improve the mechanical properties of carbon fiber is through increased

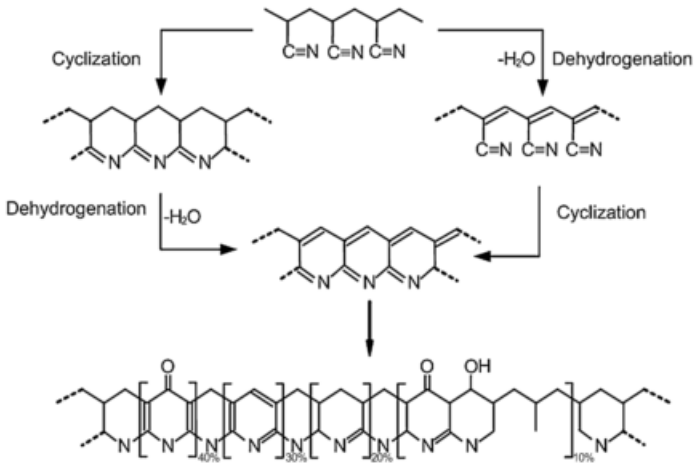

(a)

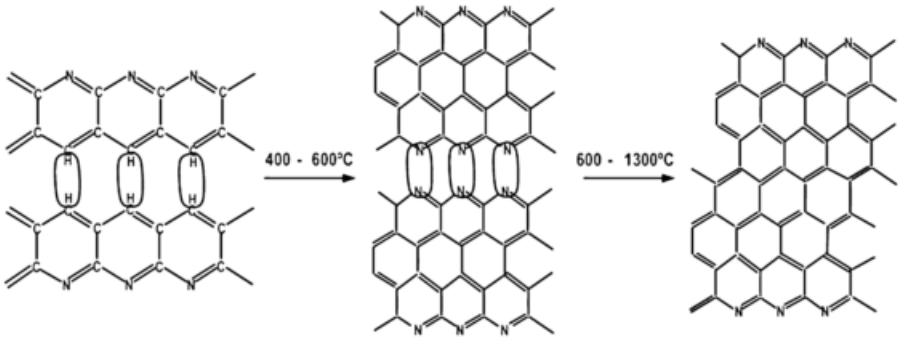

(b)

Figure 2.11: Proposed chemical changes during (a) stabilization and (b) carbonization of PAN [79].

alignment of crystalline regions in the PAN which will also lead to increased graphitic alignment in the carbonized fiber. CNTs have demonstrated formation of interphase structure within a polymer matrix in many studies. This interphase is characterized by higher density, alignment of polymer chains, and, consequently, higher mechanical properties. Additionally, incorporation of micro and nano-sized fillers within PAN precursor have shown to act as nucleation sites for crystalline regions [55]. Carbon nanotubes and graphene/graphite have been two popular fillers. Chae et al. [82] looked at the effect of single-wall, double-wall, and multi-wall carbon nanotubes and vapor grown carbon nanofibers within PAN. All fillers demonstrated improved

graphite alignment in the final fiber compared to the baseline PAN fiber. A 70% improvement in tensile strength was observed for MWNT's and a 75% improvement was made for SWNT's. Liu found that addition of CNTs improved PAN/CNT tensile strength and modulus. Liu [83] also highlighted the role of fiber tension during stabilization and carbonization for improvement of polymer chain alignment and final fiber properties.

2.3.2 Pyrolysis Simulation

Saha et al. [84] used reactive forcefield molecular dynamics to study the mechanism of graphite alignment in the carbonization process. The work used a simulation cell composed of stabilized-PAN and a carbon nanotube or graphite, seen in Figure 2.12. The cell was heated to 2200 K, 2500 K, and 2800 K, and annealed for 2 ns, 500 ps, and 750 ps, respectively. The higher temperatures are required to elucidate the reactions in the short timespans required for molecular dynamics. The first mechanism of alignment occurs at lower temperatures in which the filler's π-electrons interact with the π-electrons of the C$\equiv$N bonds in the PAN. The second mechanism is more complicated and involves the formation of a covalent bond between the filler and the fragments of the stabilized PAN structure developing in the vicinity of the filler.

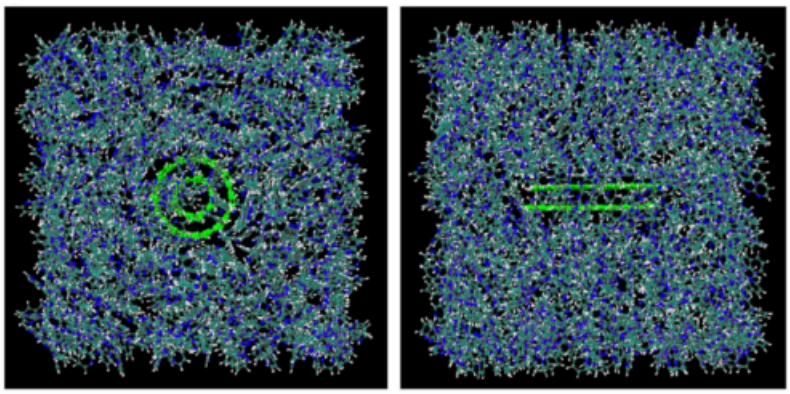

Figure 2.12: Depiction of the simulation cell for reactive forcefield molecular dynamics of PAN with double-walled CNT and graphite fillers [84].

Researchers have also used simulation to attempt to understand the mechanism

of cellulose pyrolysis. Agarwal et al. [85] used Car-Parinello molecular dynamics to look at the decomposition of cellulose at intermediate and high temperatures. They found the conversion of cellulose to HMF (hydroxymethylfurfural) and formic acid to occur through concerted mechanisms with ring contraction being the primary reaction at the lower 327 °C. At 600 °C they found precursor products formed with various pathways for formic acid, 5-hydroxy-methylfurfural, and levglucosan with the LGA formation most kinetically favorable. The LGA formation happens through C-O bond scission, neighborhood group participation in the transition state, hydrogen bonding stabilization, and then new C-O bond formations. Mettler et al. [86] also used Car-Parinello MD with artificially high temperatures to create reactions. The result was products similar to that observed with [85] but with different reaction pathways. For example, the researchers suggest a more stepwise reaction process with homolytic cleavage of the C-O bonds in the formation of formic acid. It is important to understand that using artificially high temperatures, while likely necessary for reactive molecular dynamics, may give unrealistic reaction pathways and potentially products that differ from experimentation, in which the pyrolysis process takes place over minutes.

The ab-initio techniques previously described are limited in system size and simulation time. Zheng et al. [87] used ReaxFF based molecular dynamics to analyze the pyrolysis method in amorphous cellulose. The researchers found CO_2, CO, and H_2O gaseous products as well as glycolaldehyde, hydroxy-acetone, and levoglucosan. The researchers annealed the simulation cell for 250 ps at 100 K intervals from 500 K to 1400 K. The products were in qualitative agreement with experiment; however, it was noted that small gaseous molecules varied. This can be attributed to either the short simulation time or the low temperatures. The results also were consistent with [85, 86] in suggesting that C-O bond scission is the first step in the pyrolysis process.

This dissertation will use reactive forcefield simulations, the following section summarizes the theory of these forcefields.

2.3.3 Reactive Forcefields

Reactive forcefields use only atomic positions, velocities, charges, and neighborhood information to determine the bond order of each atom and was originally developed by Van Duin et al. [24]. These forcefields update the bond order every timestep and are thus more computationally intensive than traditional, class I or class II forcefields. Short timesteps on the order of 0.1 to 0.5 fs are necessary to capture atomic movement. Determining bonding at each timestep means that these forcefields can be on the order of 10-50x slower than a traditional forcefield. However, they are able to simulate chemical reactions, specifically oxidative and high temperature degradation, on system sizes much larger than the capabilities of quantum mechanics. Additionally, existing parameterization of these forcefields have recently proven useful in describing atomistic fracture behavior in polymer matrix composites. Different reactive bond order forcefields have been developed, such as REBO and AIREBO, however in this section only ReaxFF will be discussed as it also includes non-bonded van der Waals interactions and is the latest development in this class of forcefields. ReaxFF has mainly been parameterized for combustion and aqueous reactions, as well as specific independent reactions, and for numerous atom types, see Figure 2.13 [88]. The majority of existing parameterizations exist for C, N, O, and H atoms making them particularly suited for organic polymer problems. The latest form of ReaxFF was specifically parameterized for hydrocarbon oxidation which makes it well suited to study both oxidation and thermal decomposition in polymers [89]. The form of ReaxFF is,

$$\begin{aligned} E_{system} =& E_{bond} + E_{lp} + E_{over} + E_{under} + E_{val} + E_{pen} + E_{coa} + E_{C2} + \\ & E_{triple} + E_{tors} + E_{conj} + E_{H-bond} + E_{vdWaals} + E_{Coulomb} \end{aligned} \tag{2.2}$$

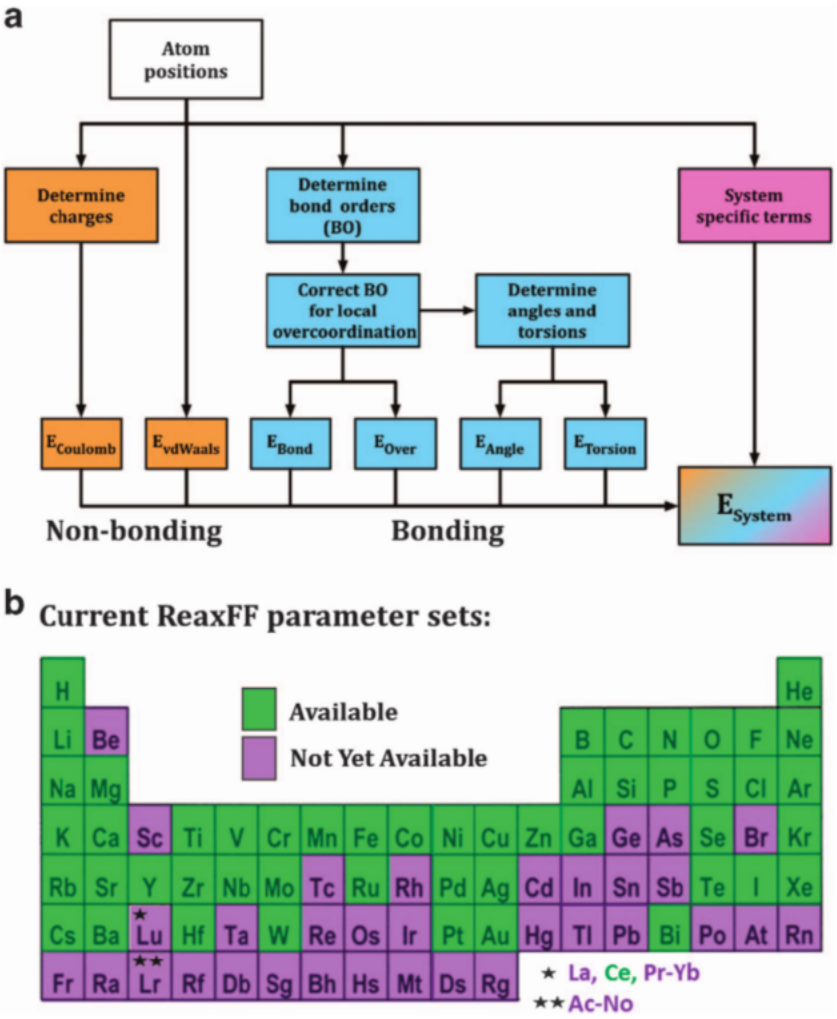

Figure 2.13: (a) Basic algorithm for calculating energies in ReaxFF and (b) the range of atom types in which current parameterizations exist [88].

where,

E_{lp}: Lone pair energy, penalty for non-optimal number of lone pairs

$E_{over/under}$: over/under coordination energy, the difference between the bond order and the number of electrons in bonds.

E_{val}: Valence angle energy taking into account changes in angle from bond order.

E_{pen}: penalty energy to stabilize systems with two double bonds sharing an atom in a valency angle

E_{coa}: Three body conjugation correction term to describe stability of such systems

E_{C2}: Energy contribution to stabilize triple bonds of C2 molecule systems

E_{triple}: energy used to stabilize triple bonded carbon/oxygen systems (carbon monoxide)

E_{conj}: four body conjugation term (aromatics)

E_{H-bond}: energy contribution from potential hydrogen bonding in the system

ReaxFF is important to consider using when exploring systems that involve chemical reactions. These include pyrolysis, catalysis, oxide formation, etc. In addition, because bond breakage is handled implicitly the morphology of polymers at different mechanical strains, particularly in the plastic regime, can be adequately described. For example, recently Koo et al. [90] used a ReaxFF parameterization to describe bond dissociation at ultra-high strain rates in a graphene-epoxy composite system and was able to accurately describe the brittle fracture behavior. Use of strain rates at $10^{12} - 10^{13}\text{s}^{-1}$ allowed decoupling of the thermal vibrations from the mechanical strain. Thus, the researchers were able to isolate bond breakage tendencies from mechanical strain alone. Odegard et al. [47] studied an EPON-862/DETDA epoxy system. They looked at stress/strain response using an existing ReaxFF parameterization and observed multiple characteristic yield events and a Young's modulus consistent with experimental measurements. A recent ReaxFF study looked at the effect of hydrothermal treatment of coal and its effect on the chemical structure [91]. The researchers found the water molecules form hydrogen bonds with coal and prevent intermolecular interaction. Li [50] used ReaxFF to study the decomposition of an epoxy network at high temperature with and without the presence of water and oxygen. It was found that ether bonds in the resin backbone were the first to break. In the system with water, the bond breakage occurred at a higher rate.

CHAPTER III

INTERPHASE STRUCTURE RELATIONSHIPS IN FUNCTIONALIZED AND NON-FUNCTIONALIZED GRAPHENE-EPOXY COMPOSITES

The benefit obtained from nanocomposite structures comes from the ability to utilize the properties of the filler material. To obtain the most benefit the stress transfer between the filler and matrix must be optimized through efficient interfacial design. This chapter will focus on using molecular dynamics simulations and the Materials Knowledge System (MKS) framework to characterize the differences in thermomechanical properties of graphene/epoxy nanocomposites with different surface functionalities. First, the structural differences in bulk epoxies as a function of strain rate, degree of cure, and functionality will be explored to validate the use of this framework to explain structural differences in MD simulations of bulk epoxy. Then, the interphase of epoxy/graphene composites will be analyzed with multi-layered graphene (1, 5, and 10 layers), hydroxyl functionalized and amide functionalized (functionalities at 1, 5, and 10% surface coverage) graphene. The hydroxyl functionalized is non-covalent and approximates a graphene oxide while the amide functionality is covalent and allows direct bonding of graphene and matrix. For each of these systems, the MKS framework [92] will be applied in order to quantify the interphase changes that occur as a result of surface modifications.

3.1 Structure Generation

Generation of an equilibrated, crosslinked polymer is a non-trivial task. Several researchers have proposed methods, all of which involve packing a simulation box with

individual monomers and using a distance based criteria to manually create crosslinks [38, 40, 56]. The epoxy structure generation procedure developed here is derived from those works. The resin used is diglycidyl ether of bisphenol F (EPON-862) and the hardener is diethyltoluenediamine (DETDA), shown in Figure 3.1. Individual monomers were drawn in the molecular editing program Avogadro [30], underwent geometry optimization, and are shown in Figure 3.2. Initial monomer units were repeated and packed into the simulation box using Packmol [31]. The pdb file output from Packmol contains atomic positions and bond topology. Editing of atom names, masses, and charges and creation of angle and dihedral topology was performed using topotools and tcl scripting within VMD. The OPLS forcefield was used for all simulations in this chapter.

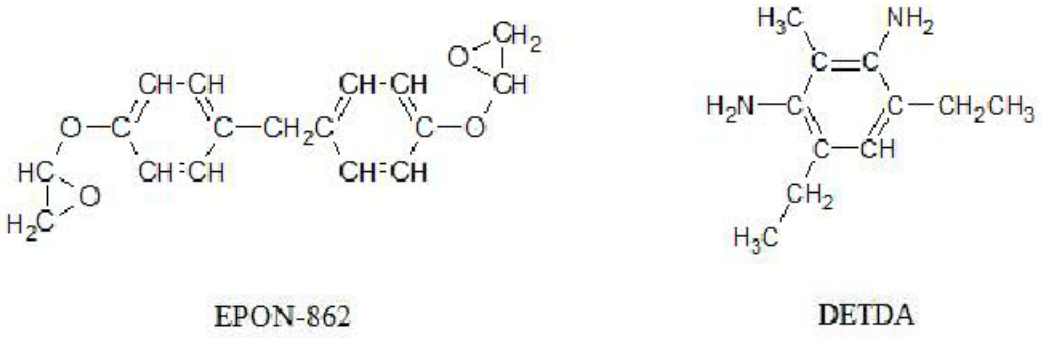

Figure 3.1: Schematic of the resin, EPON-862, and the hardener, DETDA.

The steps to obtaining equilibrium, crosslinked structure are as follows:

1. Pack DETDA/EPON-862 monomers in a simulation box at stoichiometrically perfect ratio (1 DETDA : 2 EPON-862) and at low density, approximately 0.2-0.3 g/cm^3.

2. Compress and relax structure through a series of high temperature NVT, final temperature NVT, and final temperature NPT simulations with varying pressure in the NPT simulations. This scheme is described in [41, 42].

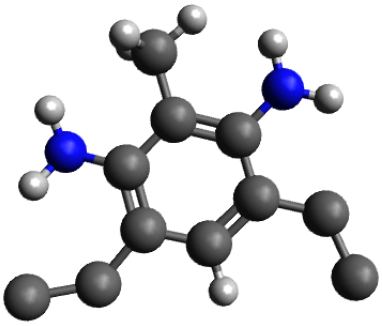

(a)

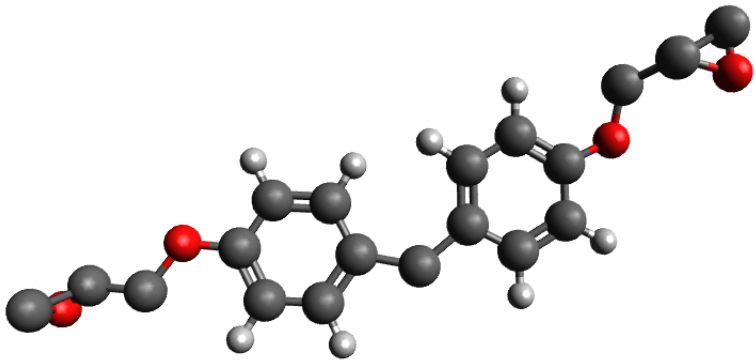

(b)

Figure 3.2: Structure of (a) DETDA and (b) EPON-862 from Avogadro with united atom representation.

3. Crosslink structure according to scheme in Figure 3.3.

   (a) Find crosslinking atoms on DETDA (amine groups) and EPON-862 (secondary carbon groups) that are within a distance r of each other.

   (b) Create bond, angle, dihedral parameters between those atoms.

   (c) Run MM minimization and 50 ps MD equilibration

   (d) Repeat (a)-(c) until no crosslinking pairs are found for two consecutive loops.

4. Repeat step 2.

For the creation of composites the above scheme is done under periodic conditions in x and y and non-periodic in z, using a reflective wall at the z-axis boundaries.

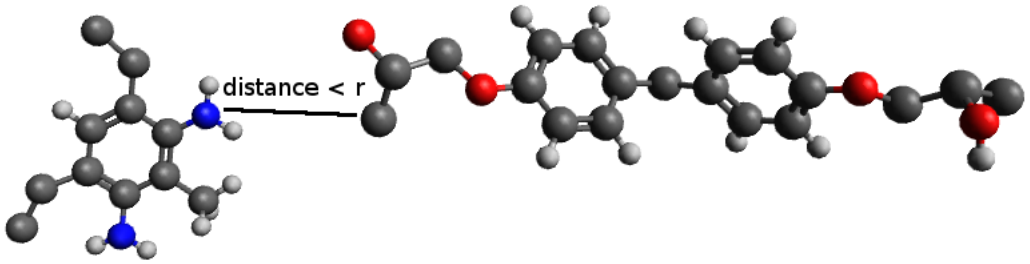

(a)

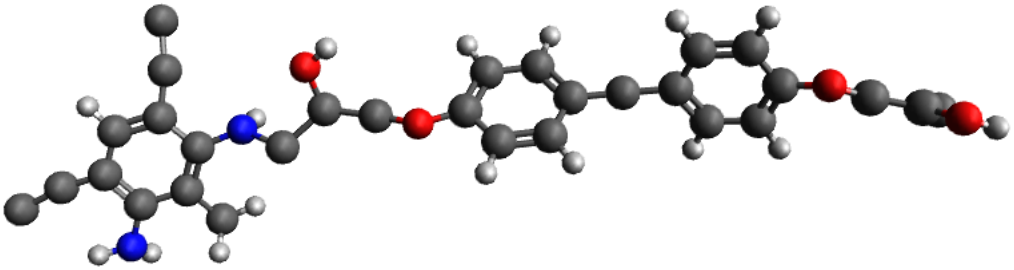

(b)

Figure 3.3: Depiction of the crosslinking process. (a) When a nitrogen on DETDA and carbon on epoxide end of EPON-862 come within a distance less than the specified radius, r, (b) a crosslinking bond is formed.

Graphene sheets of a predetermined size are generated using the "Carbon Nanostructure Builder" tool and topotools in VMD, which outputs atomic positions and bond, angle, dihedral topology of graphene. To create an "infinite" graphene sheet (maintain consistency with periodic boundaries) the atoms at the edges are bonded through the boundaries to one another using an in-house Python code. The surface functionalities are added using the same code. Realistic relative atomic positions are used to place functionalities at a carbon atom on the graphene sheet. The carbon atoms are chosen such that the functionalities are evenly distributed across the surface of the graphene. Angle and dihedral topology is added using an in-house Python code. The graphene sheet is then equilibrated with MM minimization and a 200 ps MD equilibration in the NPT ensemble with decoupling of the periodic axes pressure. This relaxes the graphene in both armchair and zig-zag directions. The equilibrated graphene and epoxy structures are seen in Figure 3.5.

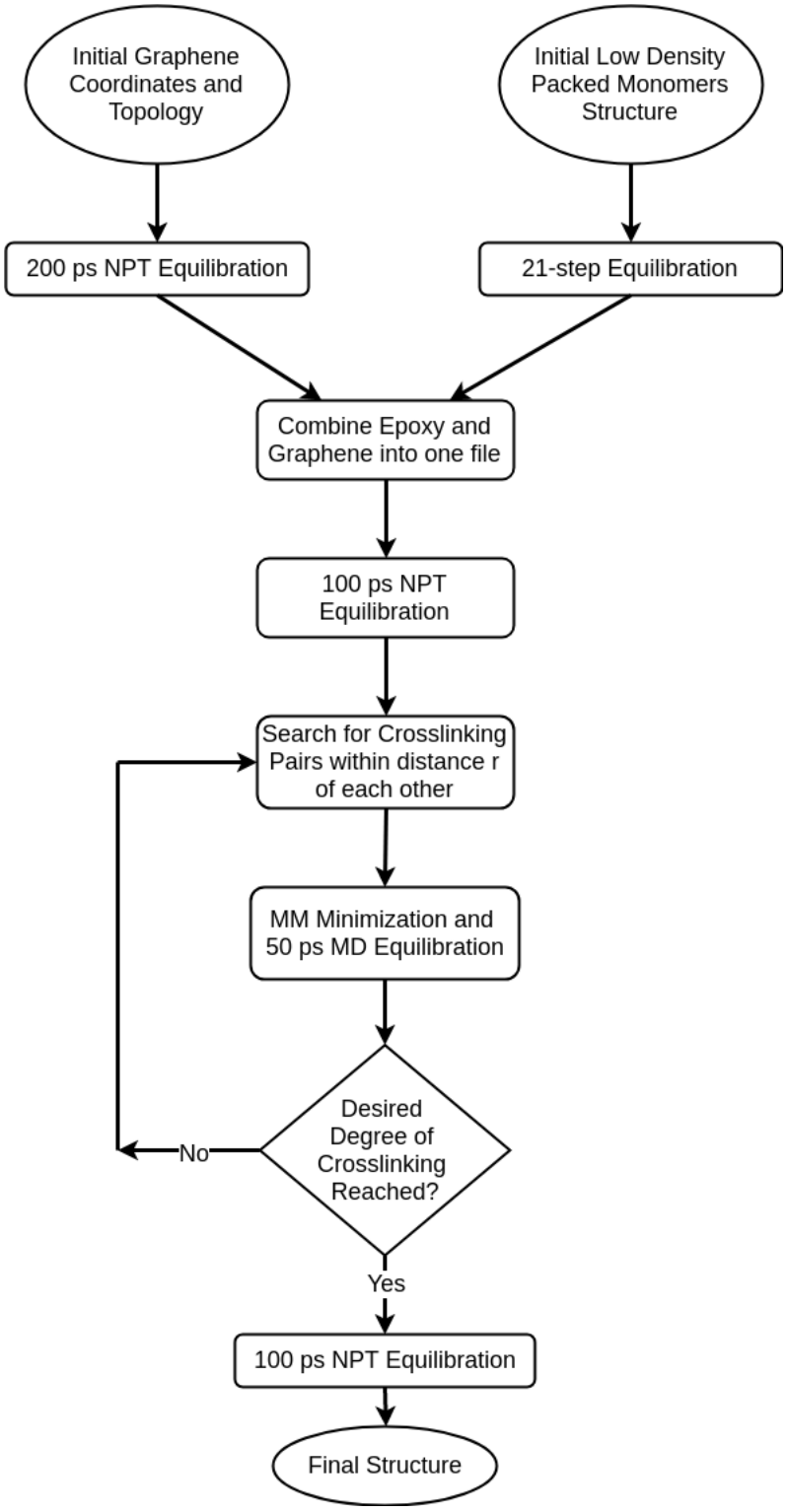

Figure 3.4: Flowchart showing the structure creation process for obtaining crosslinked epoxy/graphene composite.

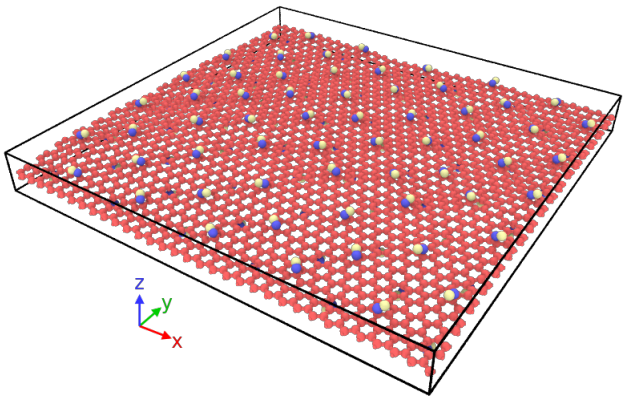

(a)

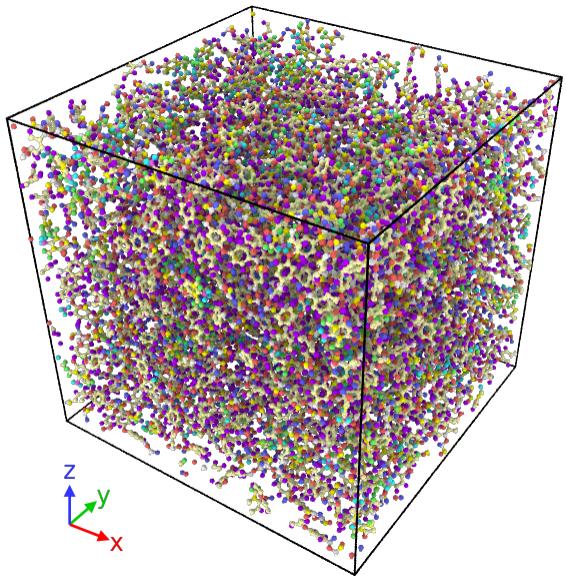

(b)

Figure 3.5: Equilibrated (a) graphene with hydroxyl functionalities and (b) non-crosslinked epoxy structure.

After graphene equilibration the equilibrated, non-crosslinked epoxy structure (step 2) undergoes a small deformation so that the box dimensions in x and y match those of the graphene sheet. The structures are then combined placing the epoxy at approximately 3.35 Å from the graphene surface to be consistent with previous MD simulations and experimental findings of interlayer graphene spacing. The z-axis is made periodic and a 100 ps equilibration is performed. The crosslinking procedure is

then allowed to occur in the presence of the graphene sheet, controlling the creation of crosslinking pairs so that none are created across the graphene and limiting the number of crosslinks that can occur per iteration to 1.5% of the total possible. The distance used for crosslinking was 9 Å and the final epoxy for all structures contained a degree of crosslinking of 75% and is seen in Figure 3.6. The temperature for crosslinking was 500 K, which is slightly elevated but increases monomer motion and helps relax the structure after crosslink formation. For the amide functionalized graphene sheet, the epoxy was able to crosslink directly to the nitrogens. The crosslink density was held to 75% as well, including attachments to graphene. This means the bulk epoxy has slightly decreased degree of crosslinking compared to non-covalently functionalized graphene. After the structure was fully crosslinked a 100 ps NPT equilibration was performed. A total of 9 structures were created in the manner described: 1, 5, and 10 layer bare graphene, 1%, 5%, and 10% attachment density of both non-covalent hydroxyl functionality and amide covalent functionality.

3.2 Structure Characterization Tools

Previous MD simulation of graphene-epoxy nanocomposites sought to describe the interfacial structure through density profiles (the epoxy structure has higher density at the interface) [57], analyzing interfacial energy [93], or through radial distribution functions out from the graphene surface [60]. However, none of these methods truly capture and quantify the changes occurring to the structure at the interface. A framework developed in [94] uses 2-point statistical correlations and spatial statistics to inherently capture detailed structural information. This work has been applied to image analysis, continuum finite element results, and recently molecular dynamics simulations [95, 96].

2-point statistics can be described by the function,

$$f_r^{hh'} = \frac{1}{S_r} \sum_{s=1}^{S_r} m_s^h m_{s+r}^{h'} \tag{3.1}$$

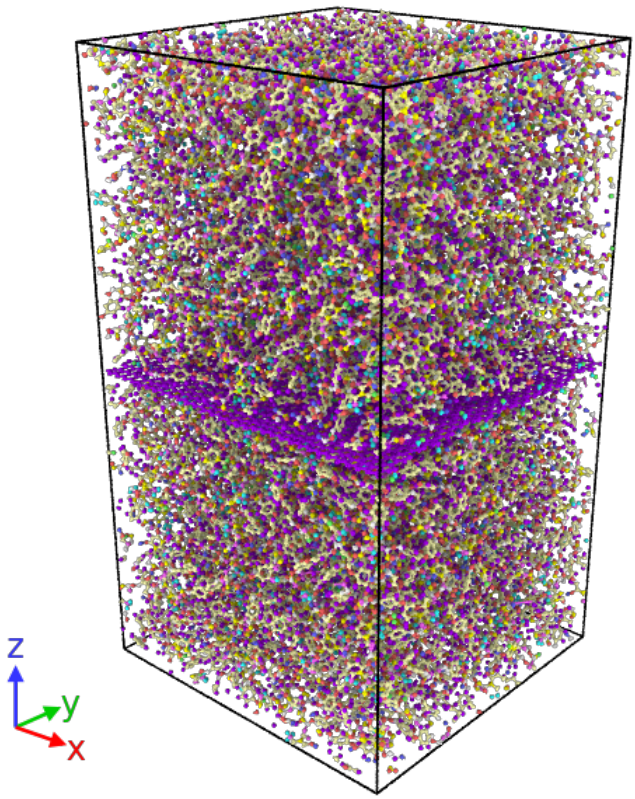

Figure 3.6: Final crosslinked epoxy/graphene structure.

As an example, imagine a binary 300 pixel by 300 pixel black and white image. Place a vector so that the tail is at one pixel and the head at another, and then repeat that process for all possible combinations within the image. The autocorrelation gives the probability density of finding black/white at both the head and tail of the vector. The cross-correlation gives the probability of black/white at the tail and white/black at the head of the vector. This function provides a probabilistic representation of structure. However, this structure representation contains as many components as there are discretizations, in the example above 300 x 300 or 9000 components. It is thus important to reduce the number of dimensions. Principal component analysis (PCA) is a dimensionality reduction technique that works by capturing the highest variances in the system. PCA can be described by first defining the covariance matrix

S,

$$S = \frac{1}{N}\sum_{n=1}^{N}(x_n - \bar{x})(x_n - \bar{x})^T \tag{3.2}$$

and the variance of the projected data as,

$$\frac{1}{N}\sum_{n=1}^{N} u^T x_n - u^T \bar{x}^2 = u^T S u \tag{3.3}$$

introducing a Lagrangian multiplier and setting the derivative of the projected variance, with respect to u, equal to zero,

$$u^T S u + \lambda(1 - u^T u) \tag{3.4}$$

we obtain an equation for the maximum variance,

$$u^T S u = \lambda \tag{3.5}$$

The eigenvector, u_1 with the largest eigenvalue, λ_1 becomes the first principal component, the eigenvector, u_2, corresponding the second largest eigenvalue, λ_2, is the second principal component, and so on. Thus, the first principal component is an axis that lies along the direction of highest variance within the data. This technique has reduced the structure to the most important details in order to describe its difference relative to other structures.

The basic procedure to obtain these statistical correlations in the case of MD simulations of graphene/epoxy nanocomposites are as follows:

1. Slice a LAMMPS dump file (snap shots of atom positions at regular intervals of time throughout a simulation) into 5 Å tall slabs away from the graphene interface and 50 Å wide in x and y directions (statistics did not change appreciably by making boxes wider than 50 Å) or 30 $Å^3$ boxes for bulk epoxy (2x the non-bonded van der Waals cutoff radius).

2. Further divide the slabs into voxels of 0.25 x 0.25 x 0.25 $Å^3$ (statistics were not changed by making voxel sizes smaller).

3. Loop through all the created voxels, if a voxel center is within the van der Waals radius (from the OPLS forcefield parameters) of an atom the voxel is labeled as 1, if it is not it is labeled as 0. This creates a binary representation of structure.

4. Develop 2-point statistical correlations on the binary structure.

5. Perform principal component analysis to extract the most salient structural information.

6. Create polynomial regression from PCA components to a structural property of interest

Alternatively, this work will also use radial distribution functions. 2-point correlations and RDF's are similar except that RDF is not directionally resolved. In an RDF, the density of atoms within a distance r to $r + dr$ is determined in a thin shell using a specified atom type as the central point. RDF's are commonly used in molecular dynamics simulations and in some cases are more appropriate structure descriptors than 2-point statistics. The workflow is the same replacing steps 1-3 with simply an RDF. The MKS theory is accessible through use of the pyMKS Python package, used extensively throughout this chapter for structural analysis.

3.3 Developing Structure-Property Correlations for Multi-functional Epoxies

There are numerous types of epoxy materials, each designed for particular end-uses. Different epoxies have been designed for strength at high temperatures, corrosion resistance, low temperature curing, etc. It is desirable to understand the underlying topological details that are crucial in determining the macroscopic properties of these epoxy materials. This section will use molecular dynamics and the MKS framework to understand the structural differences within di-, tri-, and tetra-functional epoxies. The effect of degree of cure and strain rate on the stress-strain relationships in these

materials will also be explored. All tensile simulations in this section are performed to 20% strain at 300 K with 0 atm pressure applied on the transverse axes to allow natural Poisson contraction using Nose-Hoover thermostatting and barostatting. Each system is strained in separate simulations in the x, y, and z axes. Those values are then averaged and a Savitzky-Golay filter is performed to smooth the final stress-strain graphs.

3.3.1 Simulated Systems

Epoxy structures were created in the same manner as the epoxy for the composite simulations, except that all axes are kept periodic throughout the entirety of equilibration. Di-functional, diglycidyl ether of bisphenol F (DGEBF), tri-functional, triglycidyl p-aminophenol (TGAP), and tetra-functional, tetraglycidyl diaminodiphenylmethane (TGDDM), resins were used to create three different epoxy structures. All systems used DETDA as the hardener to isolate the effect of resin functionality. The different system molecules are seen in Table 3.1. Structures were output during the crosslinking process at 0%, 15%, 30%, 45%, 60%, 75%, and 85%. The di-functional epoxy is used for assessing the degree of crosslinking on structure. For comparing between systems, the 75% degree of cure structure for each will be used. At 75% crosslinking the density for di-, tri-, and tetra- is 1.11, 1.14, and 1.11 g/cm^3, respectively.

3.3.2 Effect of Degree of Crosslinking

The degree of cure has previously been shown to significantly influence the mechanical properties of epoxy materials. A high degree of cure is associated with a rigid network that exhibits higher T_g as a result of limited chain mobility. Additionally, crosslinking constrains the network leading to strengthening. This section seeks to understand the distinguishing structural features that arise during the curing process. Di-functional epoxy structures at 0%, 15%, 30%, 45%, 60%, 75% , and 85% will be compared and

Table 3.1: Multifunctional Epoxy Systems

System	Resin:Hardener Ratio	Resin	Hardener
Di	520:260	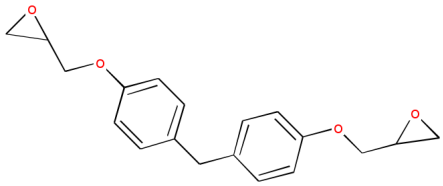	
Tri	544:408	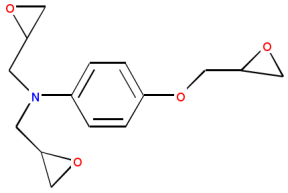	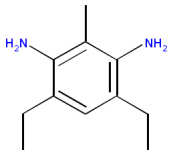
Tetra	360:360	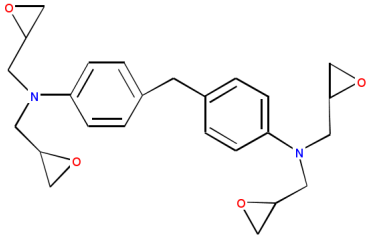	

correlated to as it undergoes tensile strain. The stress-strain response at a strain rate of $5x10^8\,s^{-1}$ is seen in Figure 3.7. As predicted, higher degree of cure results in improvements in yield and ultimate tensile strength.

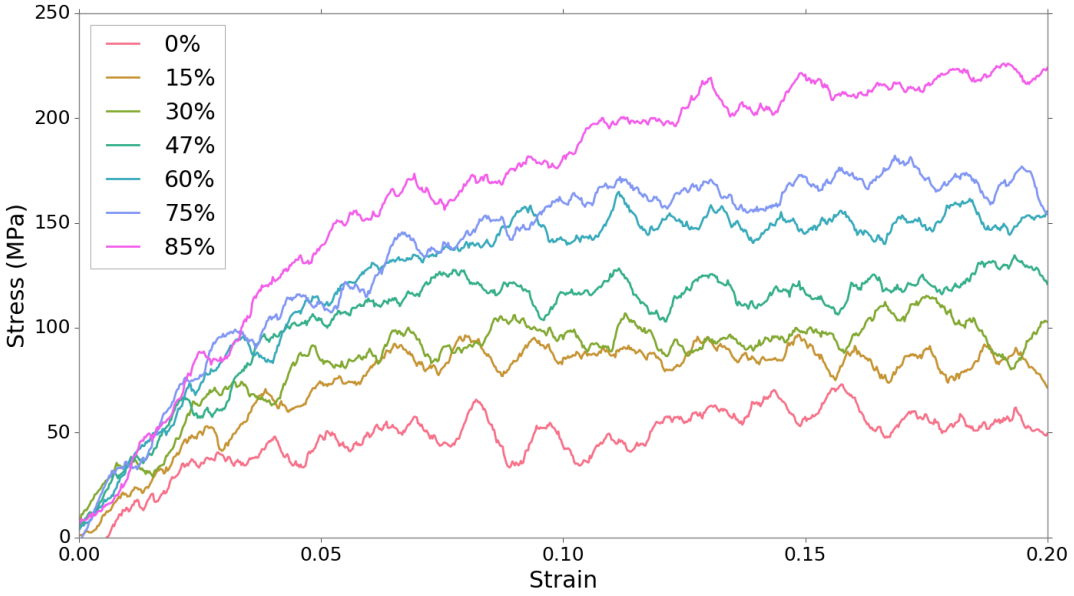

Figure 3.7: Stress-strain response in difunctional epoxy as a function of degree of cure.

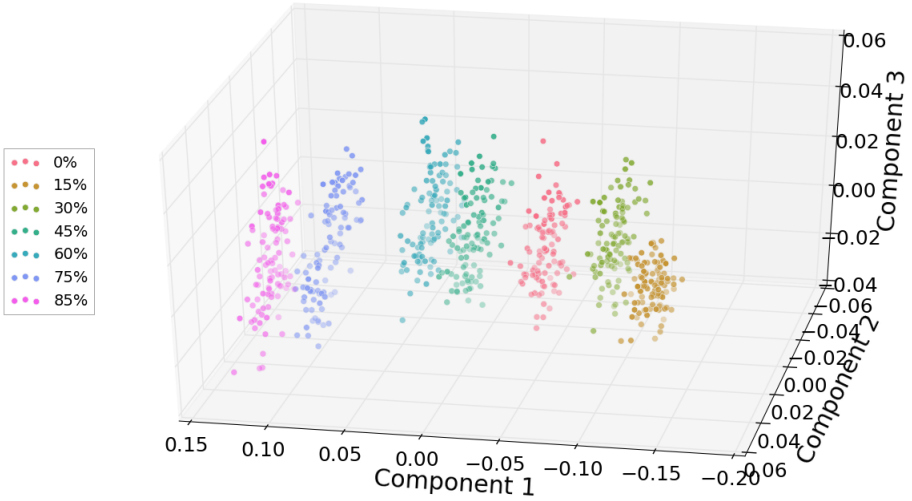

Figure 3.8: Difunctional epoxy structures represented in PCA space with components derived from the radial distribution function.

The radial distribution function for each system was calculated and then correlated

to overall system stress using the MKS framework. The structures are plotted in Figure 3.8 in PCA space. A polynomial regression model using a degree of 2 with 9 principal components was applied to relate the structure to stress. The model had average R^2 of 0.82 using 3-fold cross validation. It should be noted that nine principal components capture only 80% of the structural variance between the degrees of cure. A model built with 2-point statistical correlations resulted in over 95% of the variance being captured in just the first component. However, it was more difficult to draw a correlation to the stress values with the 2-point statistics model producing an R^2 of 0.62. The 2-point correlations contain more data points, each structure having 1,728,000 data points (120 x 120 x 120 voxels) than the RDF which has 100 data points per structure (10 Å radius with dr of 0.1 Å). Thus, only 142 structures were included for the 2-point statistics model whereas 566 structures were included for the RDF model.

3.3.3 The Role of Functionality

Epoxy functionality can play a critical role in the final properties of an epoxy. This section uses the MKS framework to develop a model which relates the structural differences arising from functionality to the stress. For comparison purposes systems with degree of cure of 75% are used. It is important to note that 75% cure does not correspond to the same crosslink density due to the different functionalities. The crosslink densities are 3.74 mol/kg, 5.50 mol/kg, and 5.03 mol/kg for di, tri and tetra, respectively. However, for developing a structure-property relationship the differences in structure as a function of cure are important to capture. Therefore, crosslink density, system density, molecular architecture, etc. are viewed as distinguishing features for a given degree of cure. The strain rate for these tensile simulations is $5x10^8\,s^{-1}$. The stress-strain response can be seen in Figure 3.9. The tri and tetra

functional systems exhibit higher yield and ultimate stresses compared to the di-functional. This is likely a result of the lower crosslink density in the di-functional resin.

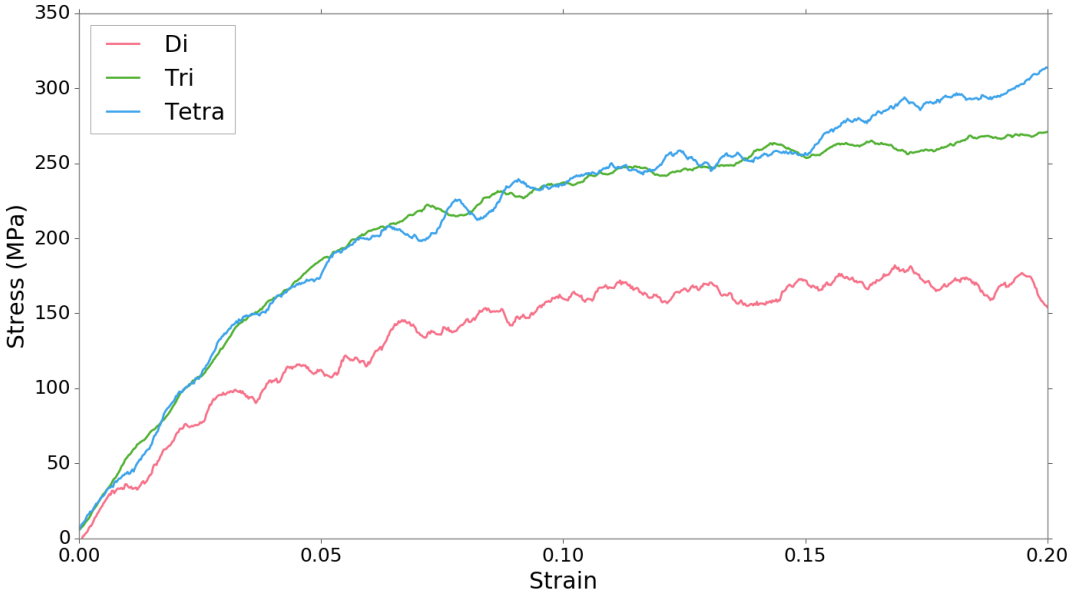

Figure 3.9: Stress-strain response in di, tri, and tetra functional epoxy at 75% degree of cure.

The MKS model using RDF was able to capture over 90% structural variance with two components. A model with 3rd degree and four components was determined to correlate best to the overall system stress, with an R^2 of 0.71. The MKS model with 2-point statistical correlations resulted in R^2 of 0.51.

3.3.4 Effect of Strain Rate

Due to the viscoelastic nature of most polymers the stress-strain relationship is affected by the strain rate. This section performs tensile stress simulations at $5x10^7\,s^{-1}$, $5x10^8\,s^{-1}$, and $5x10^9\,s^{-1}$ on the tetra-functionalized epoxy sample. Each simulation starts with the same starting structure, thus the separation of structures in PCA space can be attributed to the strain rate differences only. The stress-strain plot is shown in Figure 3.10. As predicted, the higher strain rate leads to higher stress values

experienced by the polymer.

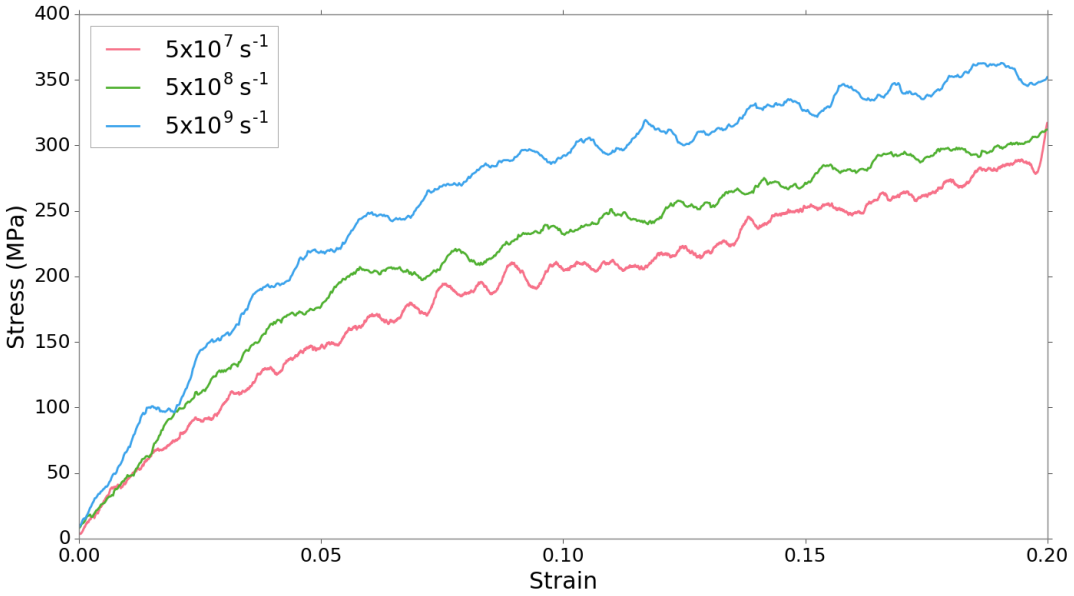

Figure 3.10: Stress-strain response in tetra-functional epoxy as a function of strain rate.

The RDF regression model with degree 2 and 9 number of components resulted in an R^2 value of 0.79. This is despite the fact that the first 5 principal components only described 34% of the variance in the systems structure. However, the 2-point statistics model captured 98% of the structural variance resulting from strain rate and predicted stress values with an R^2 of 0.65.

This section sought to validate the stated approach using both RDF and spatial statistics for bulk epoxy. While the spatial statistics better describe the structural differences in the models, the RDF are able to correlate structure with stress more effectively, perhaps as a result of more structures being included in the regression for RDFs. An overall summary of the created models in this section is given in Table 3.2.

Table 3.2: Model Parameters and Results for Multifunctional Epoxy

Model Name	Degree of Cure	Functionality	Strain Rate
Strain Rate (s^{-1})	$5x10^8$	$5x10^8$	$5x10^7$, $5x10^8$, $5x10^9$
Degree of Cure (%)	0, 15, 30, 45, 60, 75, 85	75	75
Functionality	Di	Di, Tri, Tetra	Tetra
RDF, 5 PC Explained Variance (%)	0.77	0.93	0.34
RDF, 3-fold CV Score	0.82	0.77	0.79
2-point Statistics, 5 PC Explained Variance (%)	0.95	0.97	0.98
2-point Statistics, 3-fold CV Score	0.59	0.51	0.65

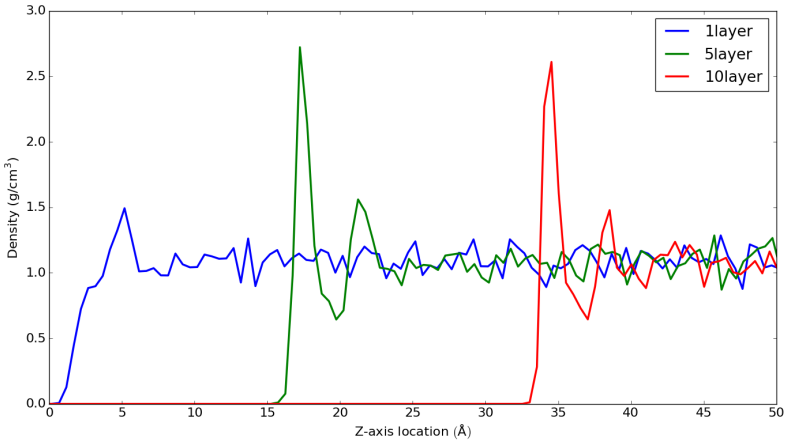

(a)

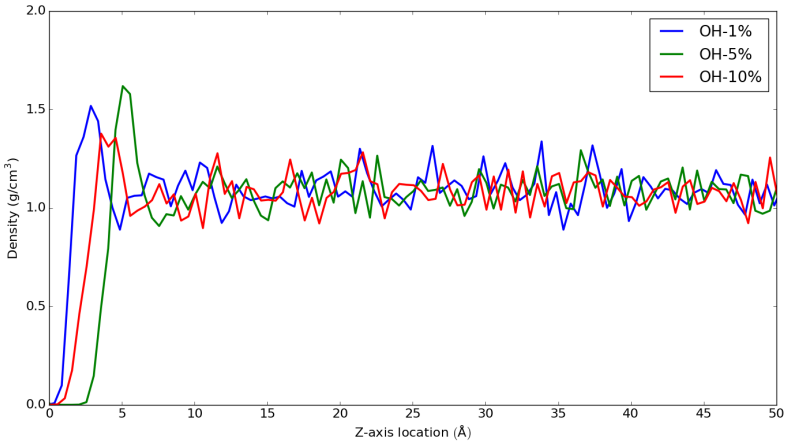

(b)

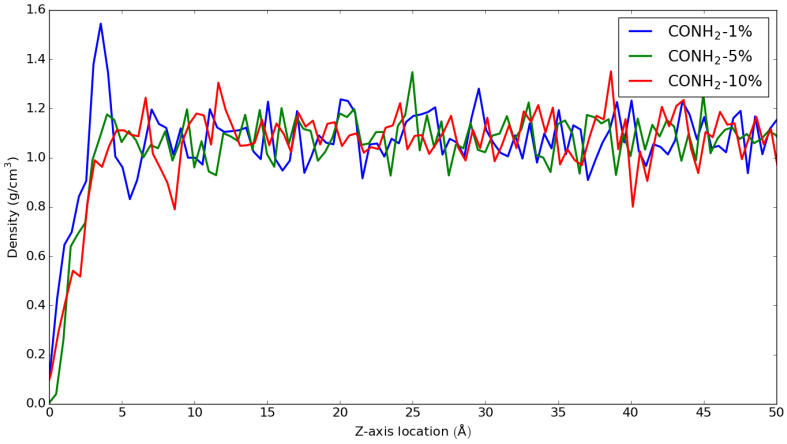

(c)

Figure 3.11: Density profiles at 300 K for the (a) multi-layered, (b) hydroxyl functionalized, and (c) amide functionalized composite systems.

3.4 Initial Composite Overall Structural Properties

Initial density profiles of all nine graphene/epoxy composite structures were obtained at 300 K. For the hydroxyl functionalized and bare graphene a structural difference, shown as increased density, is consistently visible in the initial 5 Å away from the graphene interface as seen in Figure 3.11. The 5-layer and 10-layer graphene structures exhibit significantly increased density in the interphase region compared to 1-layer graphene. Additionally, the 1% hydroxyl and 1% amide simulation densities resemble the bare 1-layer graphene likely as a result of the low attachment density. For the 5% and 10% amide functionalized graphene no difference in density from bulk epoxy was observed. Covalent surface attachment creates a smooth transition from graphene to epoxy and likely reduces the influence of non-bonded interaction structure changes on the interphase region.

Interfacial energy for each system was determined through,

$$U_{interface} = [(PE_{Epoxy} + PE_{Graphene}) - PE_{Composite}]/A \tag{3.6}$$

where A is the cross-sectional area of the simulation volume. Typically in MD the interfacial energy is obtained by taking the equilibrated matrix and filler energies separately, then bringing the systems together and obtaining the composite energy. However, this system was created such that epoxy was crosslinked in the presence of graphene and there is additional complexity with covalent attachments on three of the structures. Therefore, the equilibrated system energy was obtained first after an MM energy minimization. The epoxy atoms and graphene atoms were deleted from the system in turn and, after a minimization, both epoxy and graphene energies could be independently obtained. The interfacial energy values are summarized in Table 3.3. All values show similar interfacial energies. Amide functionalization gives the highest average energy followed by hydroxyl and then multi-layered. A positive value indicates that it was energetically favorable to bring the epoxy and graphene systems together.

Table 3.3: Interfacial Potential Energy of the Composite Systems

System	Potential Energy (kCal/mol-Å^2)
1-layer	0.52 ± 0.03
5-layer	0.55 ± 0.03
10-layer	0.51 ± 0.03
$CONH_2$ 1%	0.55 ± 0.03
$CONH_2$ 5%	0.67 ± 0.03
$CONH_2$ 10%	0.62 ± 0.03
OH 1%	0.56 ± 0.03
OH 5%	0.56 ± 0.03
OH 10%	0.67 ± 0.04

The higher value of amide functionality indicated that the attraction between amide functionalized graphene and bulk epoxy is the strongest among the systems of study.

3.5 Interphase Structure Analysis

It was demonstrated in section 3.3 that the MKS framework could be used to describe structural differences in bulk epoxy arising from functionality, degree of cure, and processing conditions (strain rate). This section will analyze the structural differences between interphase and bulk epoxy and between the interphase structure with different graphene surface functionalities. In an attempt the understand the topological differences arising from different external conditions, the analysis will be performed during three types of simulation: constant temperature, cooling through glass transition temperature, and tensile strain.

3.5.1 Constant Temperature

Constant temperature simulations were run at 300 K in the NPT ensemble. Each equilibrated sample was simulated for 1 ns with structure information output every 10 ps for a total of 101 microstructures for each sample. Structures at 0-5 Å, 5-10Å, and 25-30Å away from the graphene surface, were extracted and discretized. 2-point

statistical representations of the structures are seen in Figures 3.12, 3.13, and 3.14. The representations are in 3D but sliced along x, y, and z to show correlations in each plane and were created using Paraview [97].

It should be noted that the system size is large enough to capture graphene wrinkling, as seen in Figure 3.15. The wrinkling, in turn, creates an interphase region which undulates accordingly. However, the structure quantification method involves dividing the system into a voxelized square sub-system of just the interface at 0-5 Å from the graphene surface. The structure quantification method will therefore lose information from discretizing a curved surface in a cubic sub-system. There are two ways to consider this issue. To understand how the interphase is affected locally within a voxel then the structure should be analyzed directionally from the normal of the graphene sheet at that location. In this scenario a radial distribution or pair correlation function may be more appropriate. The second way to consider this is to include the interphase undulations within the 2-point statistics and consider it a microstructural feature. It has been previously studied with MD that graphene wrinkling has an effect on interphase properties and contributes to stress transfer from the sheet to the matrix. Therefore, this work uses both radial distribution functions and the 2-point statistics capturing interphase undulations in conjunction.

The highly oriented interphase structures with multi-layered graphene are apparent in the statistical representations compared to graphene with attached surface functionalities. The orientation along the xy plane suggests pi-stacking with carbon rings in the epoxy structure in addition to minimal graphene wrinkling. The orientation of carbon rings can be confirmed by looking at the radial distribution function (RDF) and the Herman's orientation parameter across the three types of surface functionalizations as seen in Figure 3.16. The RDF shows higher density of ring carbons at the interface compared to 10% hydroxyl or amide functionality. Hydroxyl functionalities would attract free nitrogens in the hardener and hydroxyl groups in the

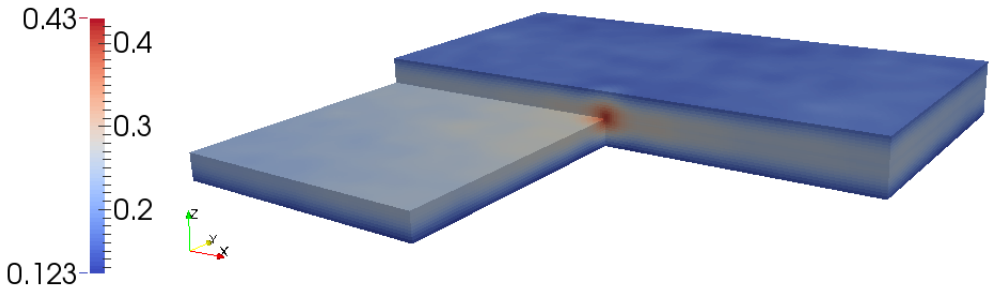

(a)

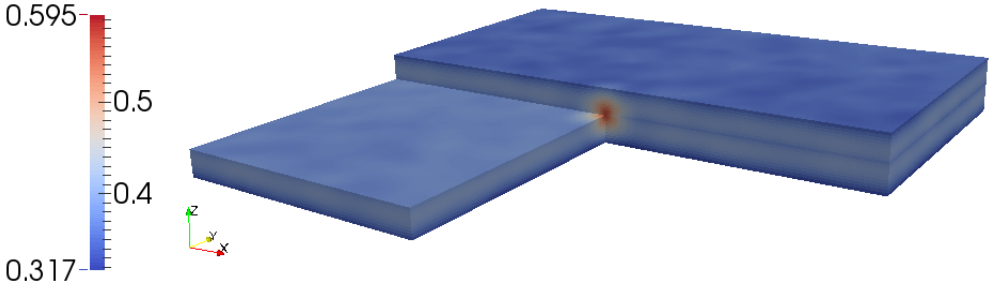

(b)

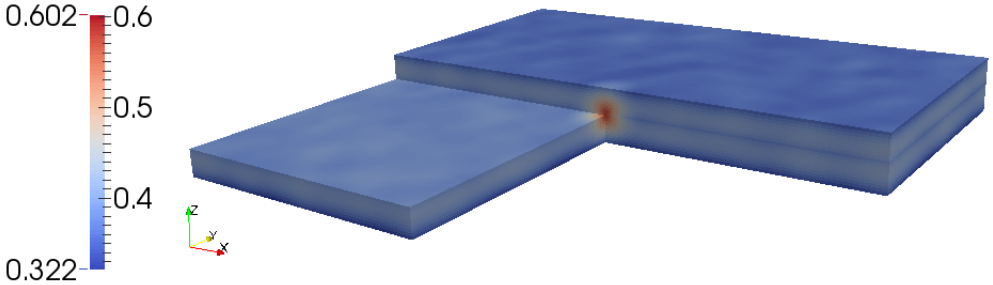

(c)

Figure 3.12: 2-point autocorrelations for the interphase structure at 0-5Å from the graphene for (a) 1-layer, (b) 5-layer, and (c) 10-layer structures.

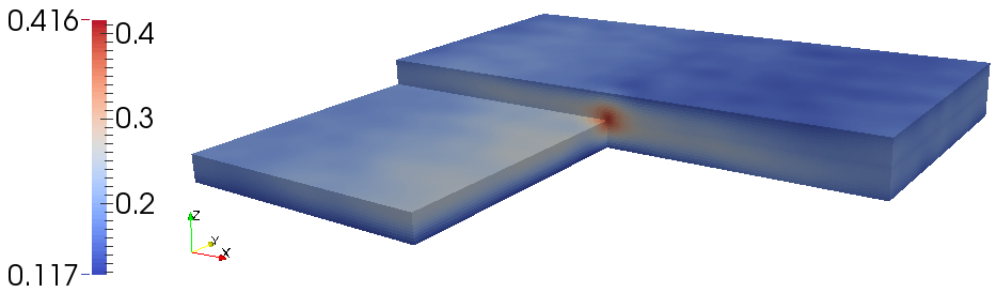

(a)

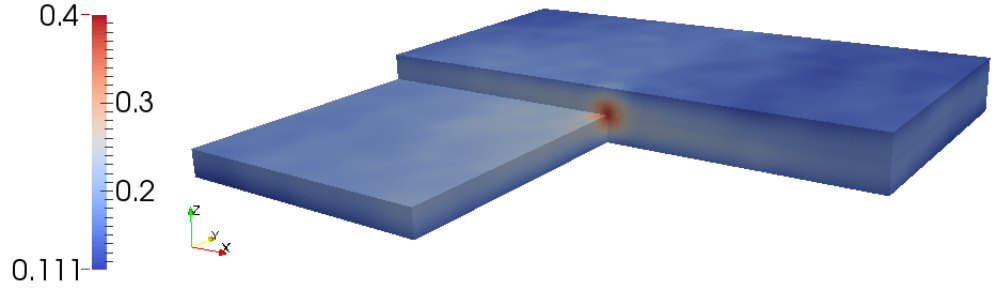

(b)

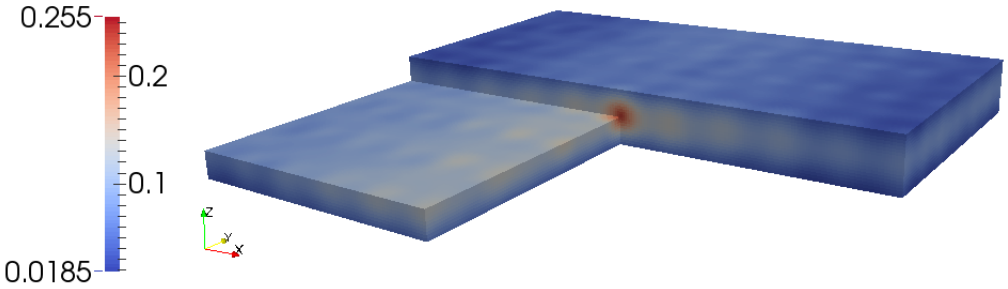

(c)

Figure 3.13: 2-point autocorrelations for the interphase structure at 0-5Å from the graphene for (a) 1%, (b) 5%, and (c) 10% amide surface coverage structures.

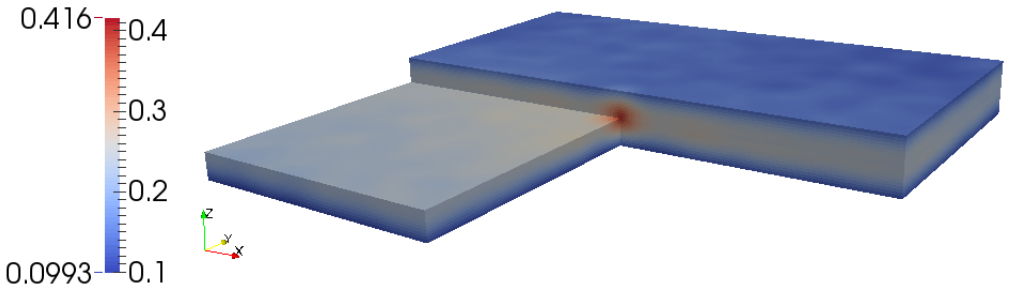

(a)

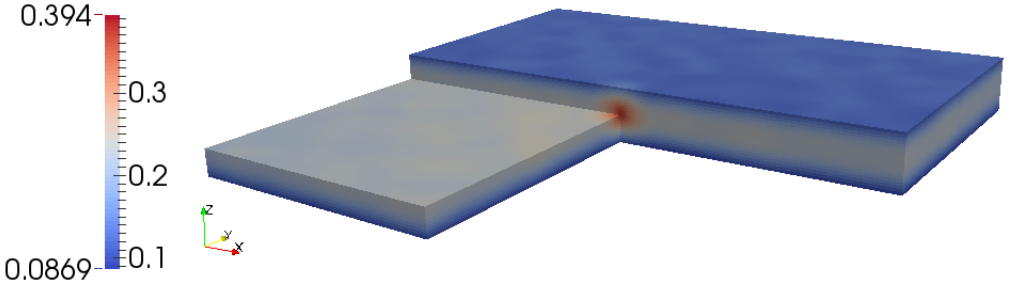

(b)

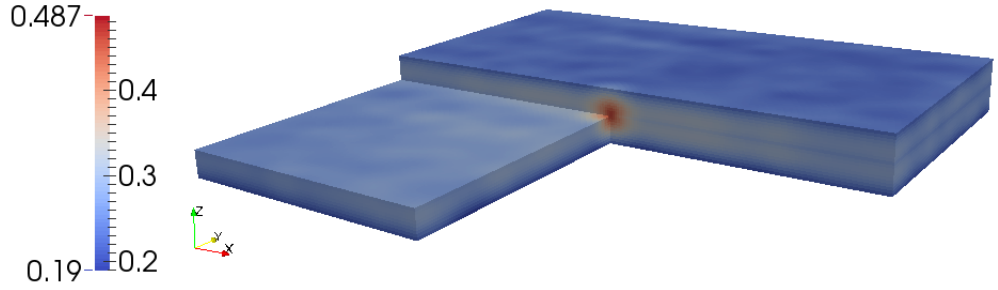

(c)

Figure 3.14: 2-point autocorrelations for the interphase structure at 0-5Å from the graphene for (a) 1%, (b) 5%, and (c) 10% hydroxyl surface coverage structures.

resin forming hydrogen bonds. Amide functionalities are covalently attached to resin chain ends and would shield non-bonded chains from interacting with the graphene.

The Herman's Orientation Parameter is commonly used in polymer science to describe the alignment of polymer chains relative to an axis. It is given by,

$$f = \frac{3(cos^2\phi) - 1}{2} \tag{3.7}$$

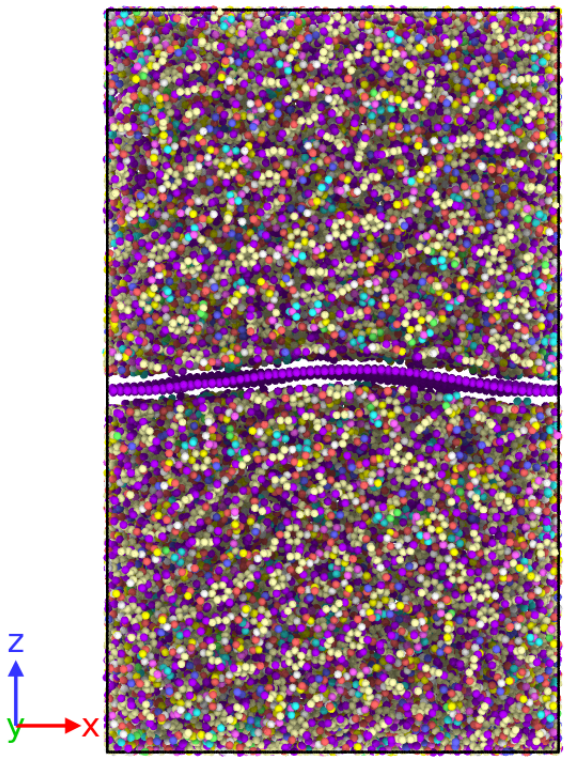

Figure 3.15: Sideview of single layer graphene at 300 K showing natural wrinkling of graphene sheet.

where ϕ is the angle between the vector of interest and the reference vector. If f is 1 the two vectors are completely aligned, if f is 0 there is random orientation, and if f is -0.5 the vectors are perpendicular to each other. Here the vector of interest is the normal of the plane that cuts through a single carbon ring in epoxy. The reference vector is the z-axis. The calculation is performed for each carbon ring in the structure. Comparison of the angle between the plane normal and z-axis describes the orientation of the rings in epoxy relative to the graphene sheet which is oriented in the xy plane. As seen in Figure 3.16b in which each dot represents a ring, despite a higher density of rings at the interface for the 10-layer sheet all samples exhibit ring orientation at the interface and then fade to random orientation over the course of about 4-6 Å. Further, the 10-layer sample exhibits orientation over the longest range from the graphene sheet.

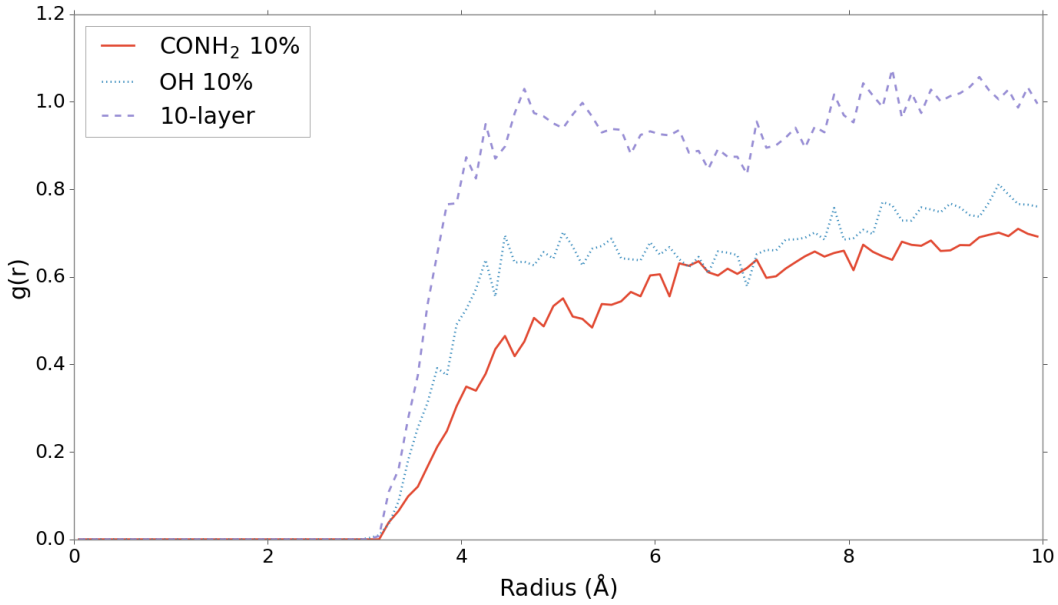

(a)

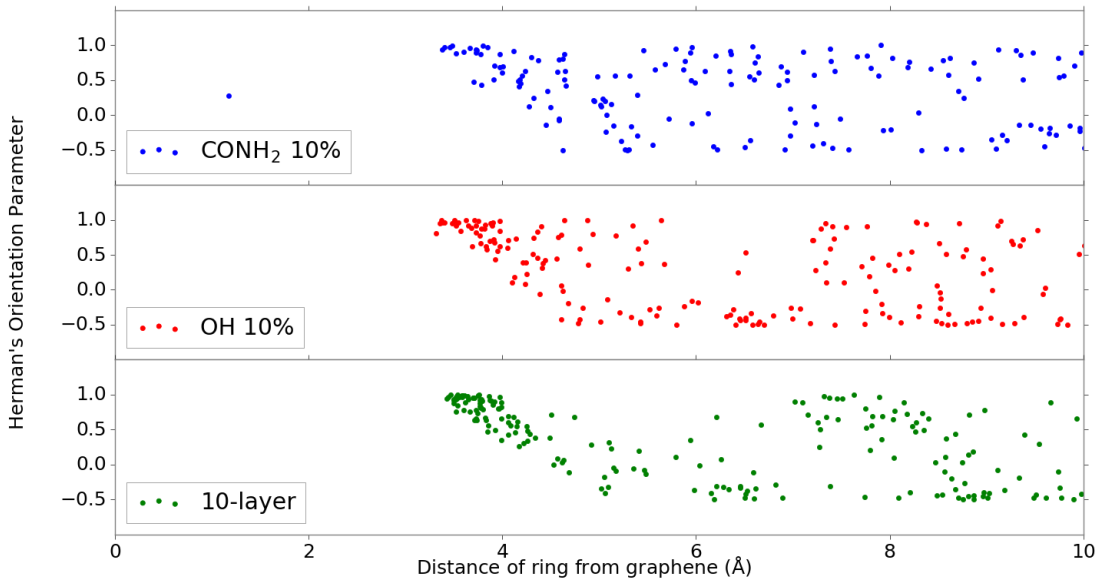

(b)

Figure 3.16: (a) Radial distribution function with graphene atoms as central atom to ring carbons in epoxy across the different types of surface functionalities. (b) Herman's orientation parameter of carbon rings as a function of distance from the graphene (each dot represents a separate ring).

To quantify the differences of the statistical representations, reduced order representations of the structures are built using PCA. This model explains over 90% of the interphase structure variance with just the first 2 components, as seen in Figure 3.17. The microstructures can be represented in a low-dimensional space in Figure 3.18. Here the microstructures are plotted according to the first three principal components. Each interphase separates and clusters within the PCA space indicating adequate information to distinguish between structures. The previous density profiles suggested that 5-layer and 10-layer samples had similar effect on the interphase structure. Indeed, in the PCA space the 5-layer and 10-layer structures cluster together suggesting little difference between the interphase in these systems.

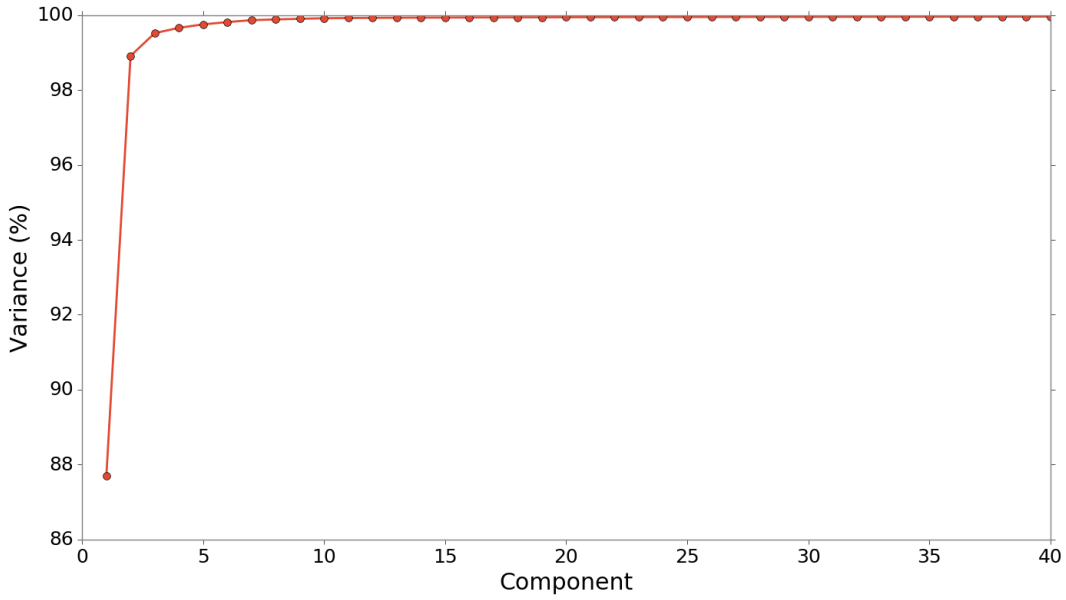

Figure 3.17: Variance captured by the low-dimensional model of interphase structures at 300 K.

3.5.2 Cooling through Glass Transition Temperature

It is known that addition of graphene to epoxy improves the T_g through surface interactions and creation of an interphase region in which matrix material is immobilized to some extent. Traditional methods for obtaining T_g in MD include cooling

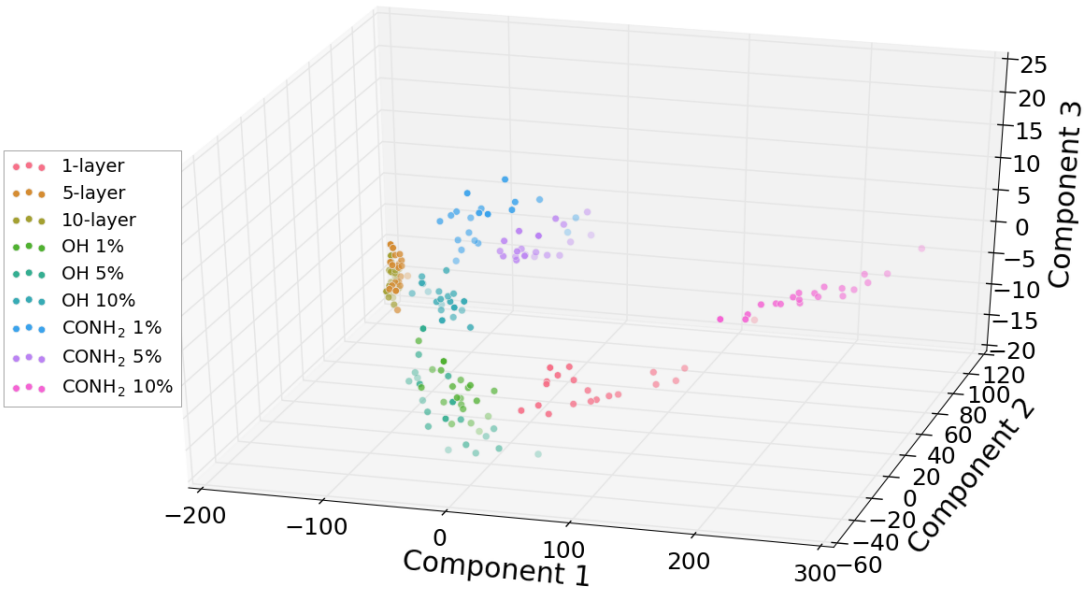

Figure 3.18: Low dimensional representation of the interphase structures. Each dot represents a microstructure from the simulation.

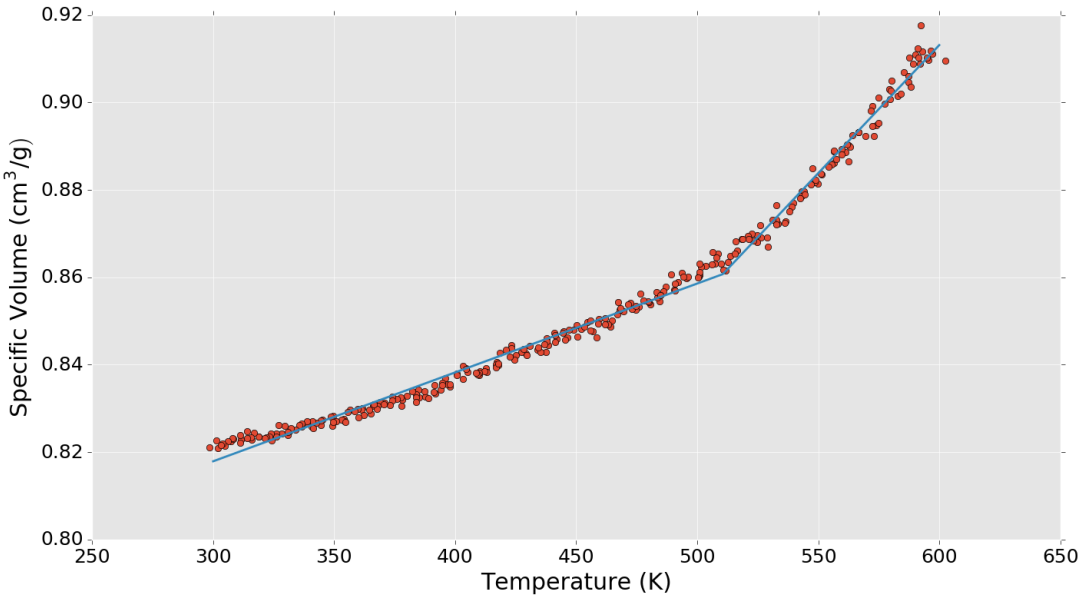

Figure 3.19: Specific volume as a function of temperature for 5-layer graphene-epoxy composite finding the glass transition temperature through piecewise linear fit.

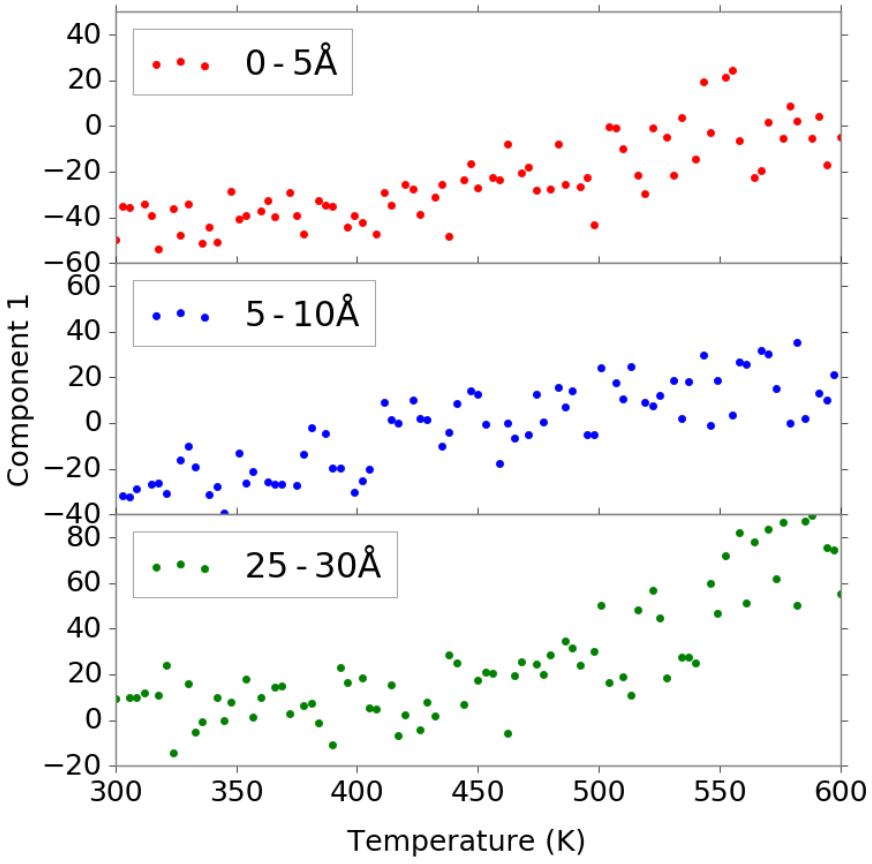

(a)

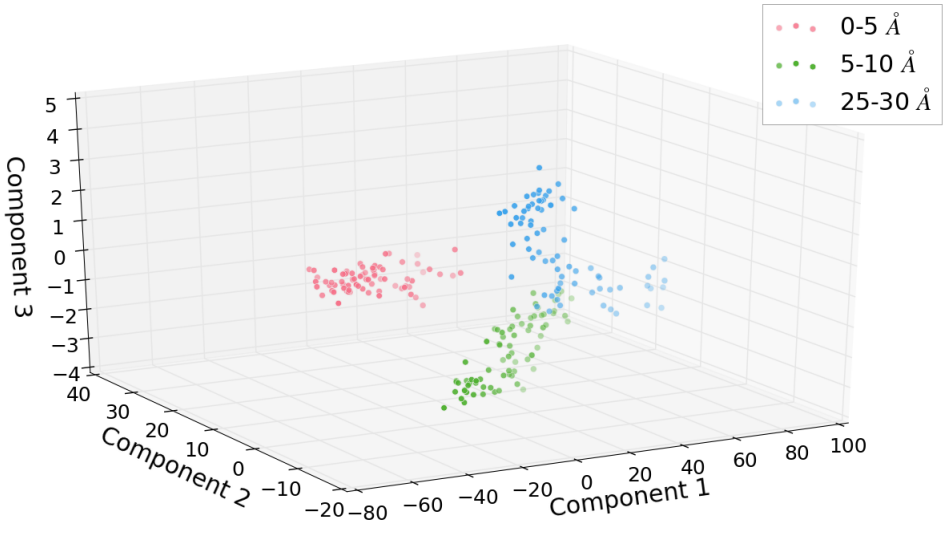

(b)

Figure 3.20: (a) First principal component as a function of temperature. The "bulk" epoxy well away from the graphene interface shows characteristic slope change at T_g while the interphase regions show minimal slope change. (b) Interface, near interface, and bulk matrix structures plotted in PCA space.

Table 3.4: Properties of Simulated Composite Systems

System	T_g (K)	E (GPa)	σ_y (MPa)	ϵ_y
1-layer	462	3.72	165.8	0.047
5-layer	510	4.56	180.8	0.042
10-layer	490	3.79	181.4	0.050
$CONH_2$ 1%	459	3.26	169.5	0.054
$CONH_2$ 5%	435	3.56	155.0	0.046
$CONH_2$ 10%	448	3.55	149.6	0.044
OH 1%	475	4.19	160.9	0.041
OH 5%	499	3.64	185.5	0.053
OH 10%	443	3.92	182.8	0.049

or heating a sample through the T_g region under the NPT ensemble and monitoring the system volume or density changes since the coefficient of thermal expansion is different above and below T_g, as shown in Figure 3.19. This method provides an overall T_g value and, as the slope change is often gradual in these systems, is sensitive to the slope change detection method. All samples were subject to cooling from 600 K to 300 K at 0.1 K/ps cooling rate. The specific volume was plotted against temperature and a piecewise linear fit was applied to detect where the slope change occurs. The obtained T_g values using this method with a standard piecewise linear fit are summarized in Table 3.4.

To understand the local structure changes as a result of cooling through glass transition in the interphase region of these composites, the correlations at the interface and in the bulk epoxy can be separated and analyzed through the use of MKS. Since cooling through T_g results in a structural change, building a model based on statistical representations of the microstructure should capture the point of change. The 5-layer graphene sample is selected here to demonstrate the process as the density profiles suggest a large interphase structure change. Graphing the first principal component versus temperature reveals the point at which the structure changes in the bulk

material, as represented by a change in slope in that graph, seen in Figure 3.20a. This slope change occurs at a temperature of 432 K, a shift of the bulk T_g of about -70 K from the overall system T_g as measured by system specific volume change. This suggests a drastic improvement in glass transition temperature as a result of adding in graphene. Part of the significant T_g increase is the high weight fraction of graphene with the 5 and 10 layer samples. The overall epoxy system was not modified between samples and thus 5-layer graphene had a higher weight fraction of graphene compared to most experimental studies.

Further, the interfacial structure (0-5 Å) and the near interface structure (5-10 Å) show no detectable deviation in their slopes. However, as shown in Figure 3.20b, the near interface and bulk samples are clustering near each other while the interface structure is clustered by itself. This shows that the further removed from the interface the more like bulk matrix material the structure becomes, but the near interface structure is still not exhibiting two distinct linear regions indicative of T_g. This suggests the interface and near interface regions are showing glassy-like structure throughout the temperature range 300-600 K as a result chains being frozen in place by the interaction with graphene.

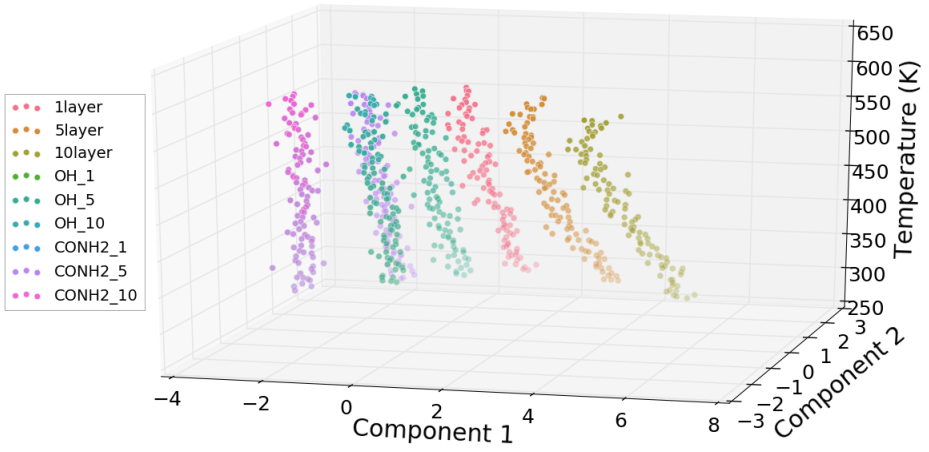

Figure 3.21: Interphase RDF with graphene as the central atom and epoxy as the distribution atoms

A regression model based on RDF with graphene atoms as central atom and graphene/interphase epoxy atoms as the distribution atoms was developed to correlate structure change to temperature. A model with polynomial degree of 2 and 3 components produced a prediction R^2 of 0.97. The structures in Temperature-PCA space are seen in Figure 3.21. The equation for the model is given by

$$\begin{aligned} T = &-19.01P_1 + 117.99P_2 + 39.4P_3 - 10.01P_1^2 + 5.72P_1P_2 + 15.62P_1P_3 \\ &+ 0.46P_2^2 + 0.57P_2P_3 + 9.21P_3 \end{aligned} \tag{3.8}$$

, where P_n represents principal component n and T is temperature.

3.5.3 Structure Changes during Tensile Strain

In this section, the structural changes as a result of normal tensile strain are analyzed. Each of the systems were subject to 20% strain at a strain rate of $2\text{x}10^8\,\text{s}^{-1}$ in the NPT ensemble with 0 atm pressure applied along the x and y axes. The stress and strain plots for each sample are seen in Figure 3.22. The modulus, yield stress and yield strain for all systems is given in Table 3.4. The yield strain is approximately 4-5% for all samples and the plastic region shows different behavior for each system type. The bare, multi-layered graphene systems show the greatest reduction in stress in the plastic region, whereas the amide functionalized samples show little stress decrease after yielding likely a result of covalent surface attachment. Figure 3.23 shows side views of a representative sample from each functionality type. The main failure location is shown through large void formation. The 10-layer sample fails well outside the interphase region in the bulk epoxy, the OH 10% sample shows failure in the interphase just beyond the interface, and the $CONH_2$ 10% sample shows the beginning of failure at the edge of the interphase region. The failure location away from the interface suggest that regardless of functionality type, the addition of graphene creates interphase regions which are stronger than the bulk epoxy, supported by the observed positive (attractive) interfacial energy values in the

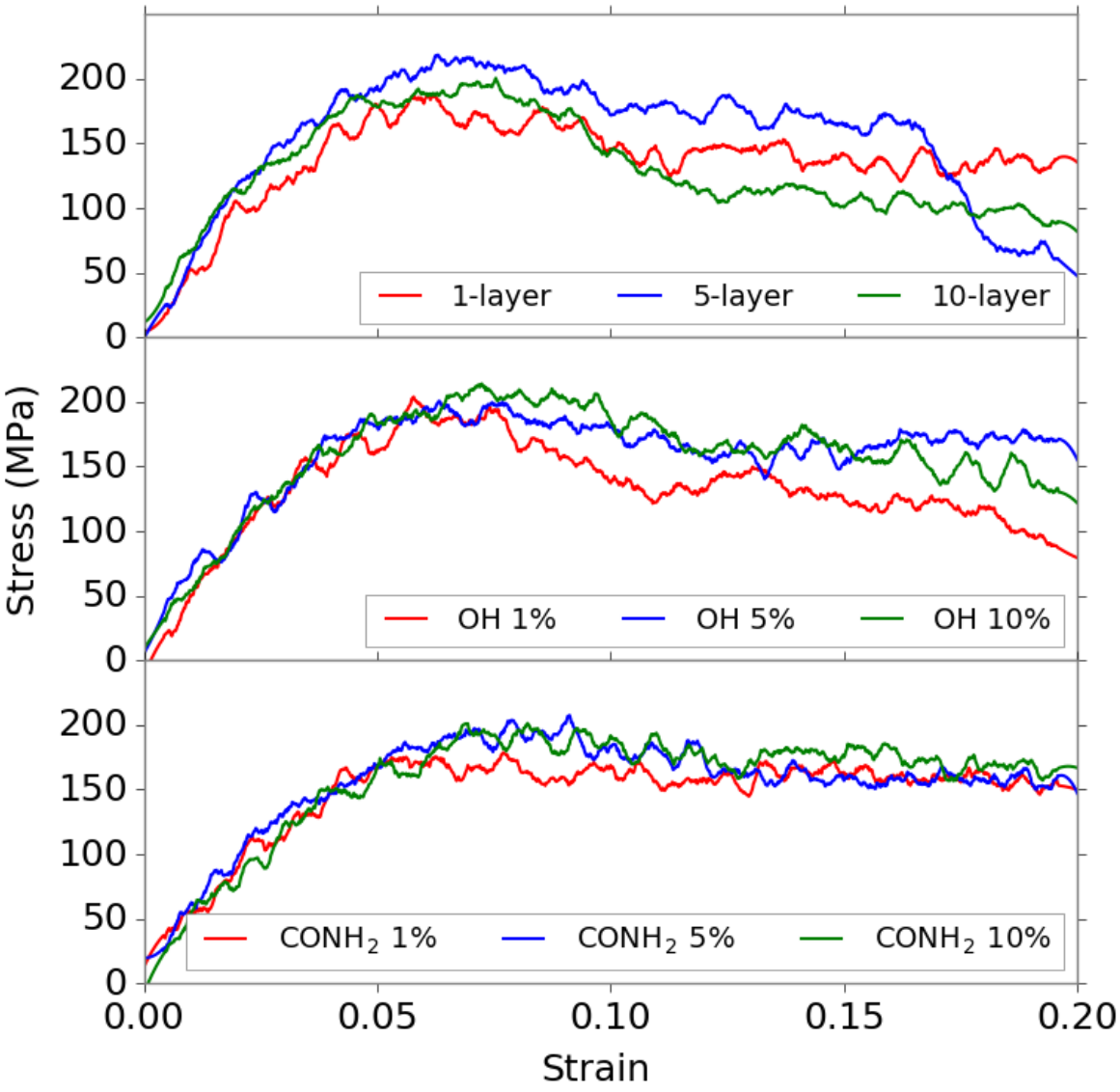

Figure 3.22: Stress versus strain plots for all systems.

composite system.

Here, it is assumed the bulk epoxy structure will be relatively constant across all samples. Thus, any differences in the stress strain behavior will be a result of the graphene surface functionality effect on the interphase structure. The overall system stress can be related to the structural properties through application of the

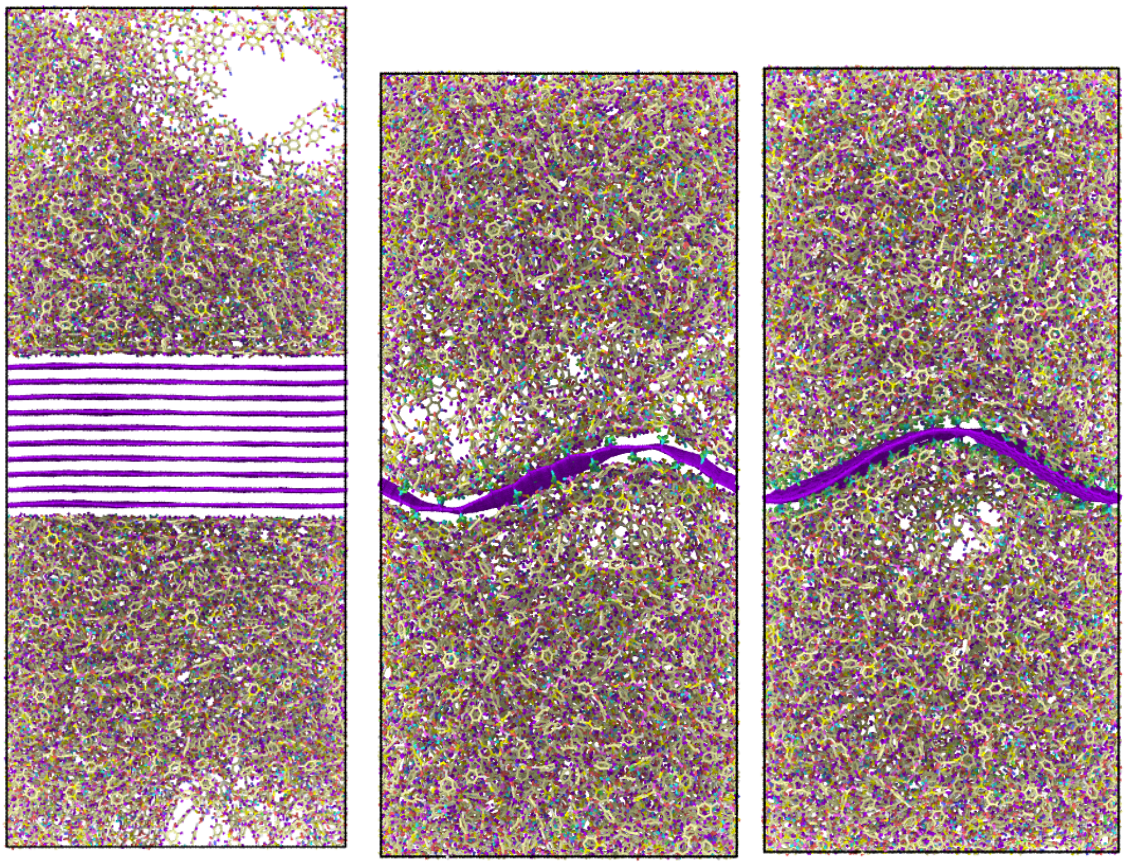

Figure 3.23: Images of (a) 10-layer, (b) OH 10%, and (c) $CONH_2$ 10% at 20% strain.

MKS framework. Since significant wrinkling of the graphene sheet occurs as a result of the stress obtaining an appropriate rectangular representative volume element is non-trivial. For this reason only radial distribution functions were analyzed with the MKS framework as opposed to the 2-point correlations. The RDF was measured from the graphene sheet to the graphene/epoxy atoms within 10 Å (the non-bonded interaction cutoff in these simulations) of the graphene sheet and with 100 bins, resulting in a radial bin distance of 0.1 Å and can be seen in Figure 3.24a. Additionally, only epoxy atoms from one side of the graphene sheet were analyzed to isolate a single interphase as opposed to the interphase on either side of the graphene sheet. RDF were calculated for each system every 0.2% strain resulting in 101 calculations for each of the 9 systems.

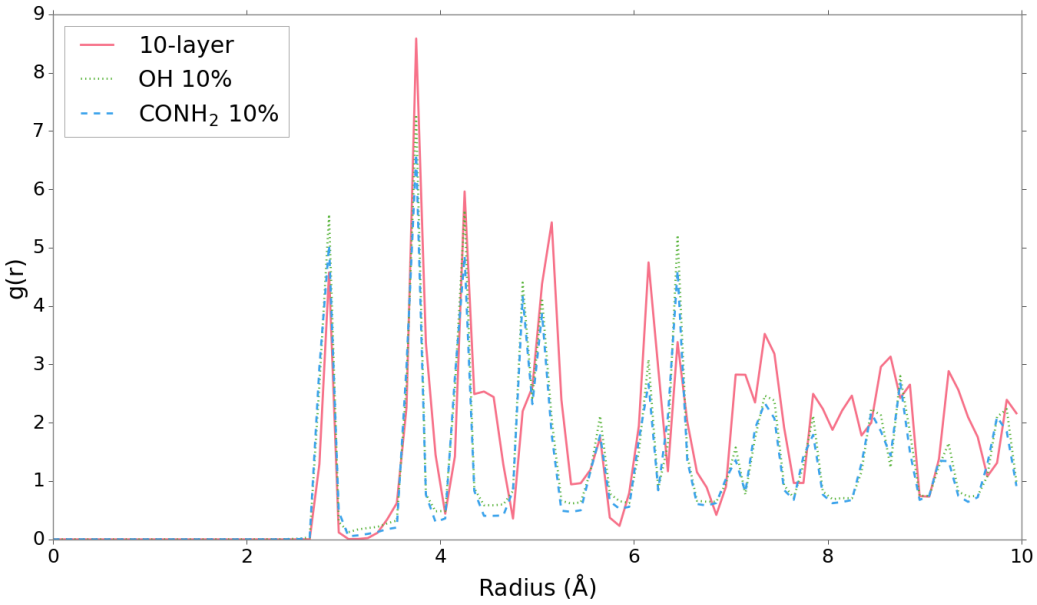

(a)

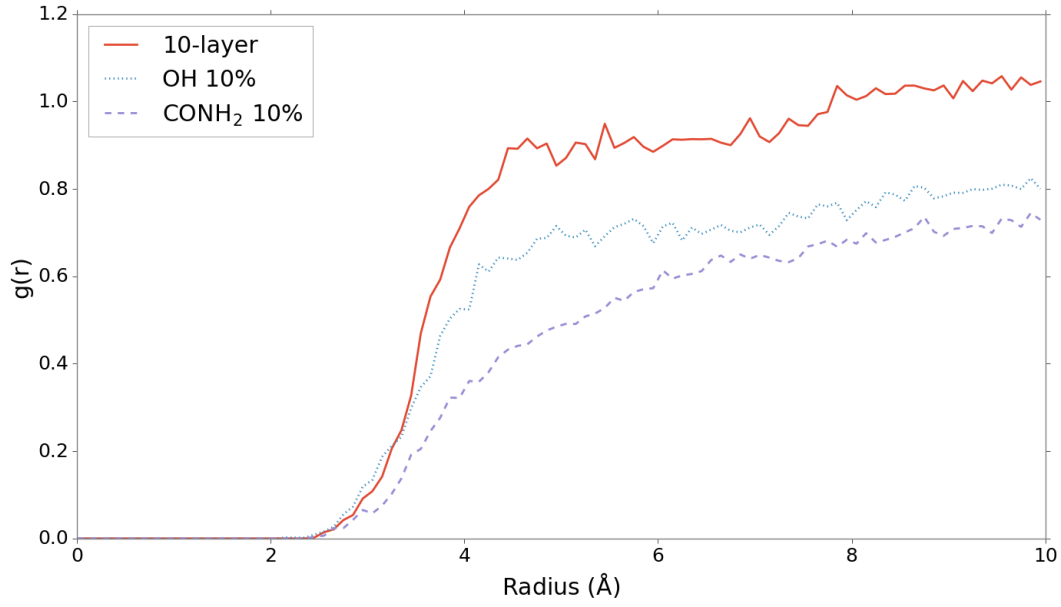

(b)

Figure 3.24: RDF for three systems studied at 0% strain using graphene atoms as central atom. (a) RDF with inclusion of graphene atoms in distribution atoms. (b) RDF with only interphase epoxy atoms in distribution atoms.

Figure 3.25 shows that approximately 95% of the interphase structure variance is explained with just 3 PCA components derived from the RDF. A simple ordinary

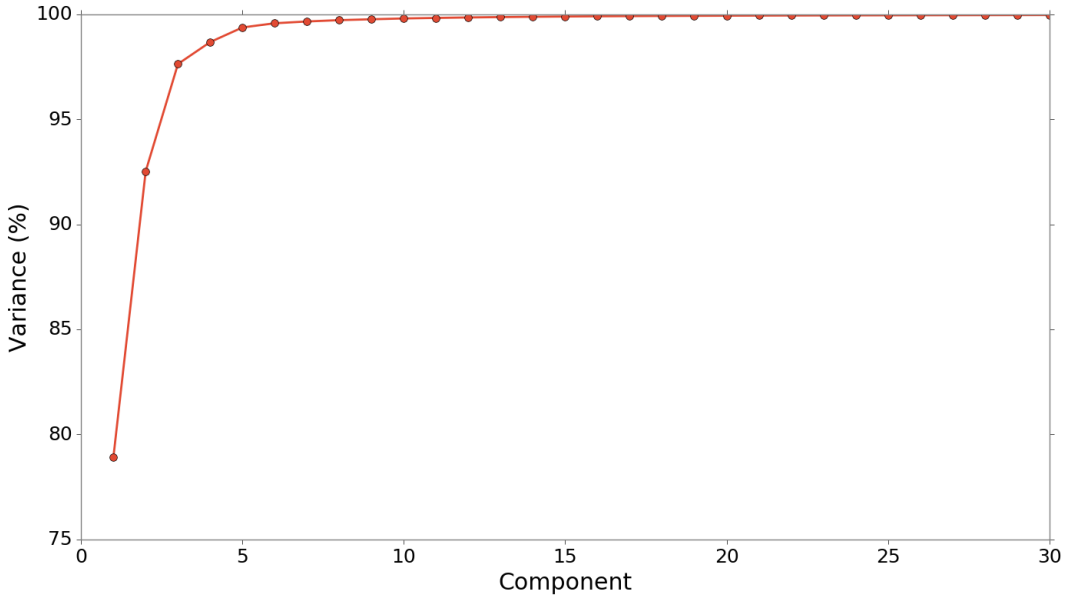

(a)

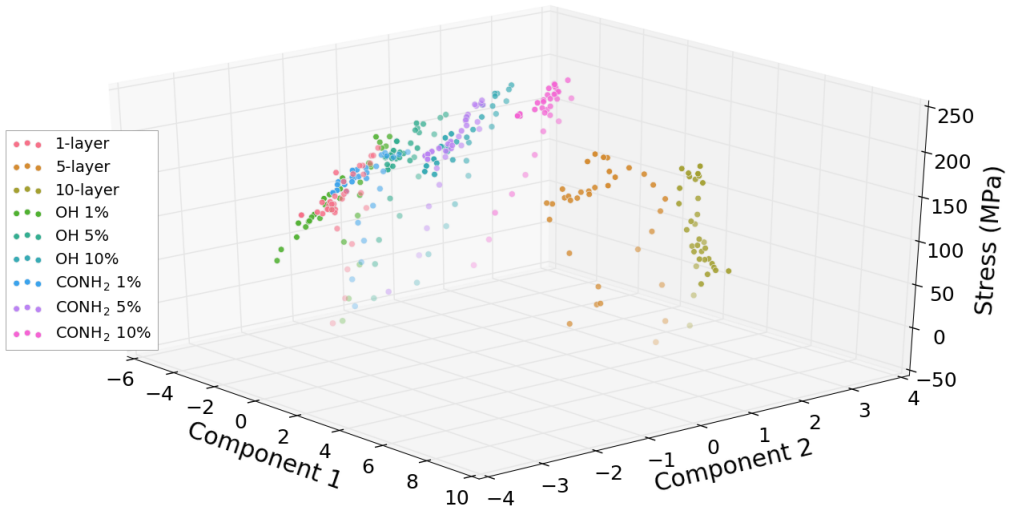

(b)

Figure 3.25: (a) Structural variance captured by PCA and (b) training data plotted in PCA space versus corresponding stress values.

least squares (OLS) model was then developed to correlate the reduced order structure representation to the macro system stress taken from the smoothed stress-strain plots. The degree of the model was varied from 1 to 4 and the number of PCA components to use varied from 2 to 11. It was determined a model with a 3rd order

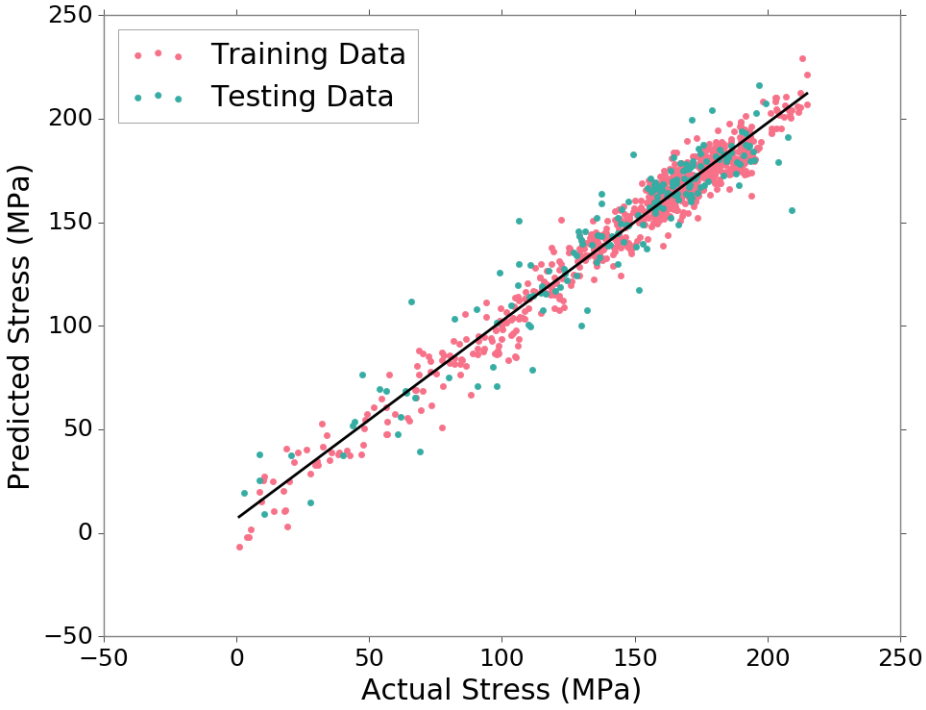

Figure 3.26: Goodness of fit of the model predictions and the actual stress values.

polynomial and 7 components best predicted the system stress, with an average R^2 of 0.92 using 3-fold cross-validation. Figure 3.25b plots the individual structures used to train the OLS model in PCA space versus stress. It shows individual clustering of the interphase region within the stress-PCA space, indicative that the model is appropriately able to separate the structures in low dimensional space and correlate them to stress. Figure 3.26 shows there is good agreement between the stress values predicted by the model and the actual data. Using this framework, the macro system stress response as a function of the interphase structure changes resulting from varying surface functionalization of graphene can be predicted. This framework can be adopted to other systems and used as a tool to predict effectiveness of surface functionalization type and attachment density using molecular dynamics.

3.6 Conclusions

This research explored the use of MD to characterize interphase structural changes in epoxy/graphene nanocomposites resulting from surface functionality type and density. 2-point statistical correlations and radial distribution functions were both found to adequately describe the structural change in epoxies resulting from differences in functionality, strain rate, and degree of crosslinking. This led to characterization of interphase changes in graphene/epoxy composites. Principal component analysis was able to describe the salient features of the interphase change during constant temperature, cooling, and tensile strain simulations. The principal components were then used to directly relate interphase structural change to temperature and bulk stress values.

This methodology can be used to predict values of stress or thermal response of nanoscale composites using MD. The vast space of possible surface attachment types, densities, and distributions creates a challenging and time consuming experimental problem. It is also difficult and expensive to experimentally characterize the interphase structural change resulting from these surface interactions. The prediction models presented in this research are important for rapid thermomechanical property prediction, screening of surface functionalities for their effectiveness using inexpensive computational techniques, and robust characterization of interphase structural change from filler addition. Future work in this area could look into different functionalities and different composite systems. Previous work for linear polymers has suggested the interphase as a region of high crystallinity and this method could potentially characterize the crystalline nature of that interphase for a thermoplastic polymer.

CHAPTER IV

COVALENT ADAPTABLE NETWORK DISSOLUTION BEHAVIOR AND THERMOMECHANICAL PROPERTIES

Thermoset matrix materials provide strength and stability at high temperatures due to the formation of covalent crosslinks. However, this rigidly formed network is not easily degraded, recycled, or reused leading to a plastic waste issue. A potential solution is through the use of covalent adaptable networks or CANs. This chapter will explore CANs that use transesterification reactions. By forming a network structure with ester groups at the crosslinking sites it is possible, with application of heat and a catalyst, to allow crosslinking sites to interchange. This rearranges the structure and allows for material relaxation as well as reaction with some solvents leading to a potential route for recycling and re-use of a thermoset. This chapter will use MD to explore the mechanism involved when dissolving a CAN in ethylene glycol and resulting effects on thermomechanical properties.

4.1 Structure Generation and Bond Exchange Reaction Modeling

4.1.1 Initial System Creation

The CAN system used for these simulations is a diglycidyl ether of bisphenol A (DGEBA) resin and a tricarballylic acid (TCA) crosslinker, seen in Figure 4.1. The system was chosen based on previous experimental work exploring the dissolution of this material. Although this particular system may not be stable for structural applications it is of interest for electronics encapsulation and will lay the groundwork for simulating other systems with enhanced thermomechanical properties. The

crosslinking process reacts secondary linking carbons on DGEBA to the activated carboxylic oxygen on the tricarballylic acid, seen in Figure 2.8. Generation of the initial, crosslinked structure follows a crosslinking procedure similar to Chapter 3.2 and is summarized in Figure 4.2. The equilibration and crosslinking processes are performed with periodic boundaries in the x and y axes and non-periodic in z in preparation for creating one simulation box with ethylene glycol. Crosslinking and final system temperature was 450 K to be consistent with experimental diffusion studies. The degree of crosslinking was 85% for all systems using a search radius of 9 Å. A probability factor was incorporated to limit the number of crosslinks throughout the crosslinking process. At the beginning if a pair was found, it had only 10% chance of bonding. The probability gradually was increased as more bonding occurred until 100% probability in the last few iterations of the crosslinking process. The system was modeled with the OPLS-united atom forcefield [20], which has been used previously for other epoxy systems. The final bulk system density was approximately 1.06 g/cm^3 which is slightly lower than experimental values of 1.1 to 1.2 g/cm^3 found in most room temperature epoxies; however, the higher temperature and non-periodic z-axis would both contribute to a lower system density. The initial CAN system maintains perfect 3:2 stoichiometry with 540 DGEBA molecules and 360 TCA molecules or 32,400 total united atoms.

To create the ethylene glycol system, 3975 EG monomers (Figure 4.1c) were created and packed into a low density simulation volume in the same manner as with the CAN and then slowly compressed over 5 ns to match the x and y dimensions of the final CAN system and the z-axis was changed to give a system density of 1.1 g/cm^3. The two systems were then stacked into one complete system with 2 Å spacing between them. Figure 4.3 shows the final system consisting of 47,280 united atoms representing 74,490 total atoms. The catalyst is not explicitly modeled and

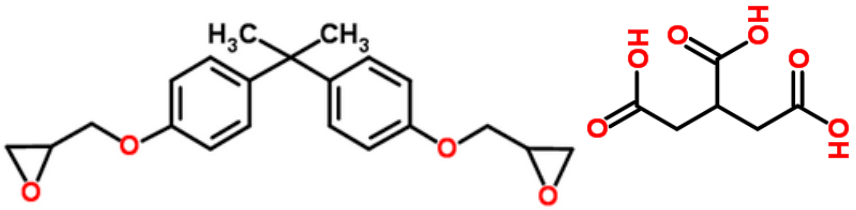

(a) (b)

(c)

Figure 4.1: DGEBA (a) and tricarballylic acid (b) monomers used in the creation of the covalent adaptable network and (c) ethylene glycol used as solvent.

is assumed to be evenly distributed throughout the system. To equilibrate the final system a 100 ps NPT equilibration was performed restricting the CAN and EG from diffusing across the initial boundary line between the two systems but allowing interactions. The wall restriction was removed for final BER process simulation.

4.1.2 Modeling the Bond Exchange Reaction and Dissolution Processes

The bond exchange reaction process is detailed in Figure 4.4. Modeling the bond exchange reaction process follows the work of [77] with minor differences. The main difference is the potential energy of the crosslinked oxygen is compared rather than just the crosslink-bond energies. The potential energy includes the oxygens' contribution to bond, angle, dihedral, and pairwise interactions. The BER process is performed under NPT conditions to allow for changes to the box shape as dissolution reactions are occurring and the system density is changing. The BER process follows a similar procedure to that of crosslinking using a distance based criteria to form bonds. A BER rate of approximately 1.5% of total possible bonds and relaxation time of 100 ps between bond checks has been shown to be appropriate for modeling the kinetics of this system. Carbonyl sites and secondary epoxide carbons that were

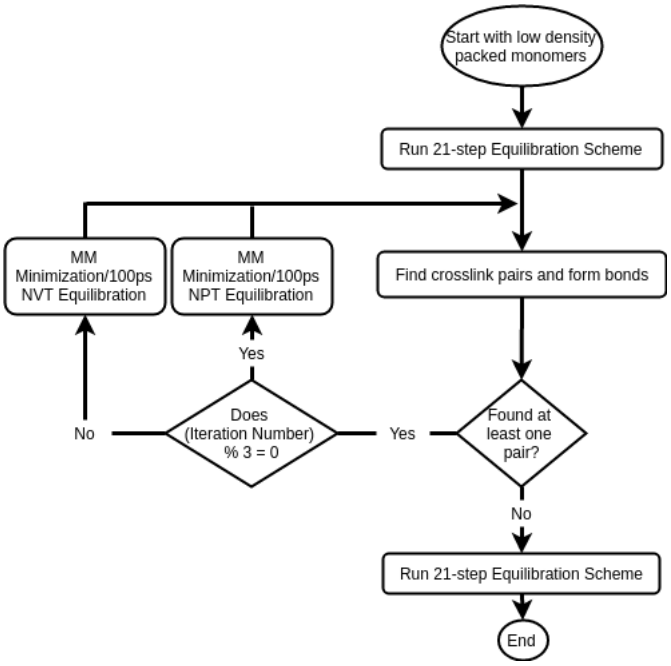

Figure 4.2: Flowchart outlining the crosslinking reaction process.

initially not crosslinked are excluded from taking place in the BER process. The total BER simulation time for these structures is 25 ns, or 125 iterations. Three different systems were created, each having 85% degree of crosslinking and the same number of EG molecules. Where applicable, data was averaged across all three runs. The scheme is summarized below and seen schematically in Figure 4.5:

1. Start with crosslinked structure.

2. Find carbonyl crosslinking site within a distance of 3.2 Å to an active oxygen. If found, bond the atoms, change double bonded oxygen to single bonded, and update all topology information.

3. Perform energy minimization and NPT equilibration for 100 ps.

4. Compare potential energies (PE) of crosslinked oxygens (the PE includes oxygen's contribution to bond, angle, dihedral, improper, and pairwise energies).

5. Break the crosslinking bond of the oxygen with higher PE and update topology

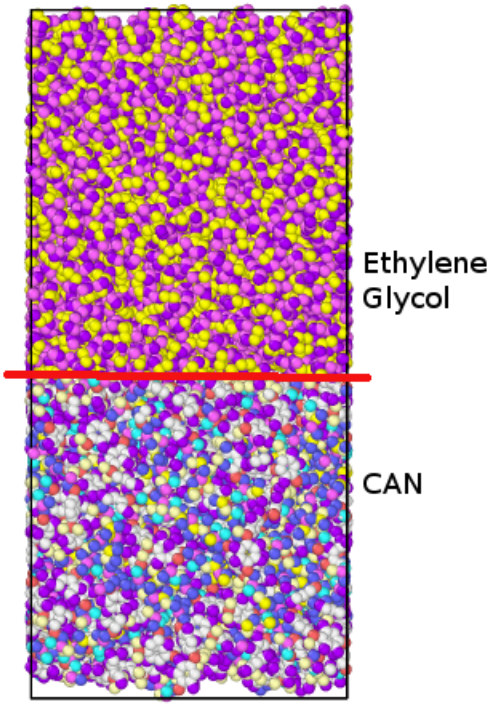

Figure 4.3: Initial configuration of the simulation box, with periodic boundary conditions in the xy directions and non-periodic in the z direction.

information (including redefining the double bonded oxygen).

6. Perform energy minimization and NPT equilibration for 100 ps.

7. Repeat steps 2-5 for N number of iterations.

Performing the dissolution reactions uses the same search radius, 3.2 Å, as the BER reactions. The only difference is that once dissolution bonds form they are permanent. This reduces the number of potential crosslinking sites to participate in a transesterification reaction. In contrast, an exchange reaction keeps the number of potential crosslinking sites constant throughout the simulation. If both a potential BER and dissolution reaction are found within the search radius, the bond is formed with the atom at a shorter distance to the crosslinking point. After each 100 ps NPT equilibration atom trajectories, bonding between atoms, density profiles, BER locations and atoms involved in BER, dissolution bond locations and atoms involved are output to

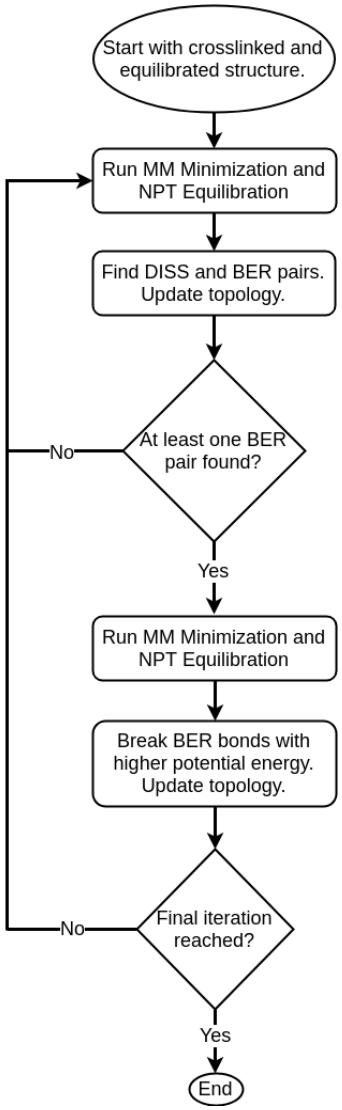

Figure 4.4: Flowchart outlining the scheme for MD simulation of bond exchange reactions.

analyze network degradation.

4.1.3 Structure Creation for Thermomechanical Models

Thermomechanical modeling to obtain stress-strain relationships, glass transition temperatures, and solvent effect on these properties has slightly different structure creation procedure. For models only analyzing BER and with no solvent present, the same 21-step equilibration scheme and crosslinking procedure is used as before but with periodic axes in all directions. During the scheme, structures are output at

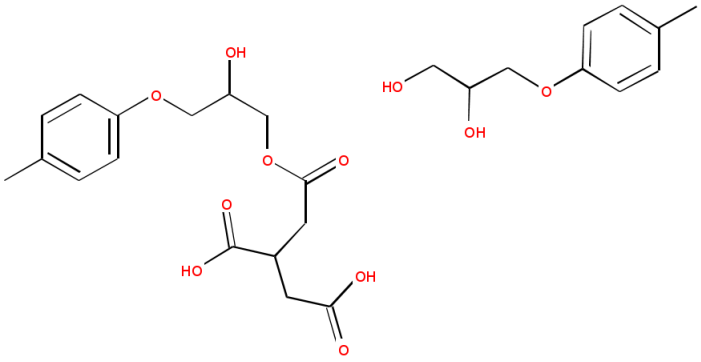

(a)

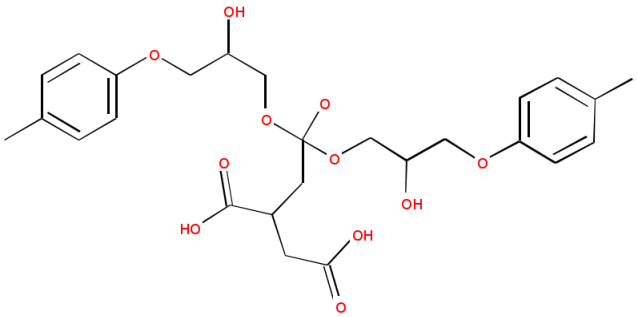

(b)

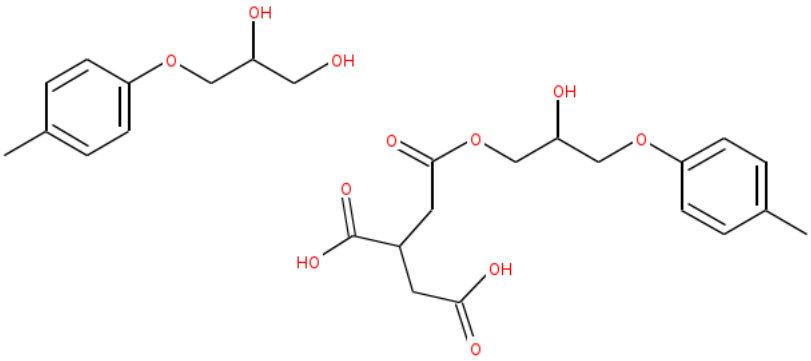

(c)

Figure 4.5: Schematic of BER reaction process shown with one half of interacting DGEBA monomers for simplicity. (a) crosslinked DGEBA and TCA molecule and dangling end on another DGEBA molecule comes within distance r of carbonyl crosslinking site. (b) Temporary triple bonded structure formed, all topology updated, and structure equilibrated. (c) Initial bonded oxygen had higher energy after equilibration and is broken, all topology is updated.

25%, 50%, 75%, and 90% degree of crosslinking. When analyzing solvent effects on properties and diffusional properties, EG molecules are embedded during initial low density monomer packing. The crosslinking reaction occurs in the presence of EG but no chemical reactions with the solvent are created. An example structure without solvent is seen in Figure 4.6.

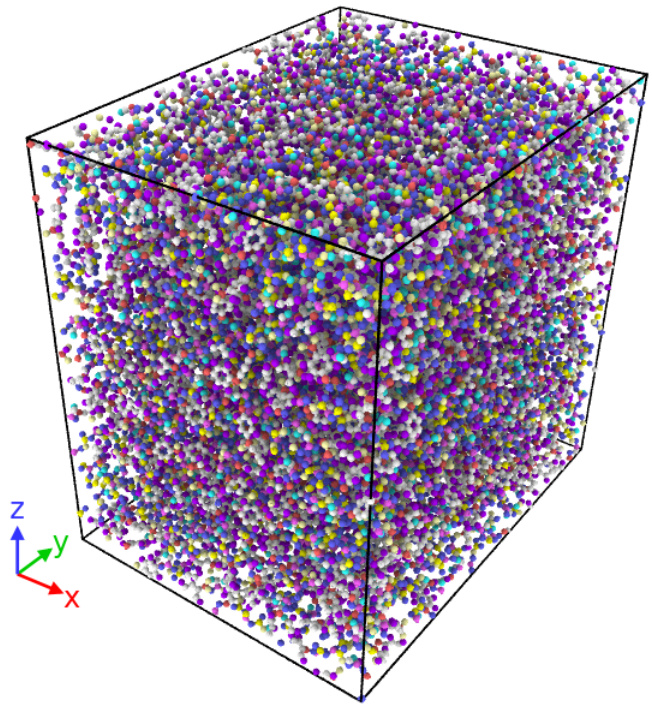

Figure 4.6: Initial crosslinked CAN simulation structure for use during thermomechanical modeling. Boundaries are periodic in all x, y, and z.

4.2 Bond Exchange Reaction Rate Effect on Ethylene Glycol Diffusion

Diffusion of solvent in a network polymer is generally slower compared to non-crosslinked polymers. Crosslinking imposes network constraints that restrict mobility of individual segments of the polymer. The network is unable to rearrange to accommodate solvent molecules, thereby slowing diffusion. However, the exchange reactions in CANs allow network rearrangement and faster relaxation times than typically seen for network polymers providing an opportunity for solvent molecules to penetrate the

network as rearrangement is occurring. Furthermore, in the case of EG and CAN, the EG reacts with crosslinking sites in the CAN to gradually lower the crosslinking density of the system, allowing faster diffusion. Figure 4.7 shows polymer density profiles of the simulated system at 100 ps, 8 ns, 16 ns, and 24 ns into the simulation for when BER and DISS are allowed to occur. The profiles show gradual intermixing between the polymer and solvent, blending the interface between the two materials.

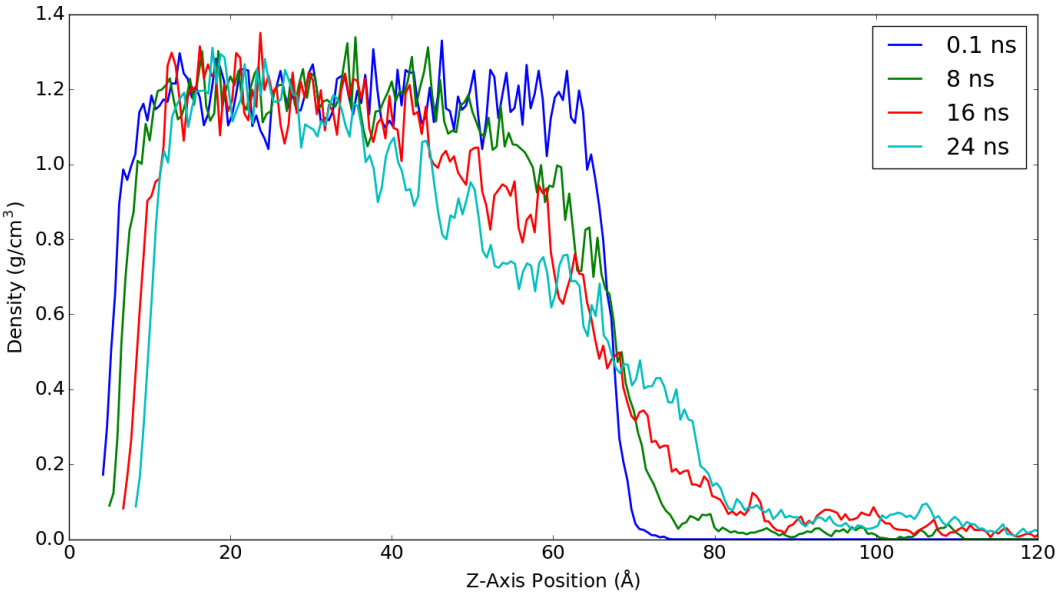

Figure 4.7: Density profile of the CAN polymer at 100 ps and 8, 16, and 24 ns into the simulation at a BER rate of 3.1%

Experimentally, the rate of BERs for a given CAN system is a function of the concentration of the catalyst and/or temperature. Although catalyst is assumed to be uniformly distributed in our simulation, by altering the pair search radius, r, different BER rates can be achieved. The BER rate is defined as the number of BER reactions that occur per iteration as a percentage of the total number of crosslinked sites. Pair search radii were changed from 0.0 (or disallowing BER reactions), 3.0, 3.2, 3.3, 3.4, and 3.5 Å, which corresponded to BER rates of 0%, 0.3%, 3.1%, 6.3%, 9.0%, and 12.6%, respectively. Figure 4.10 compares the diffusion profiles of EG 10

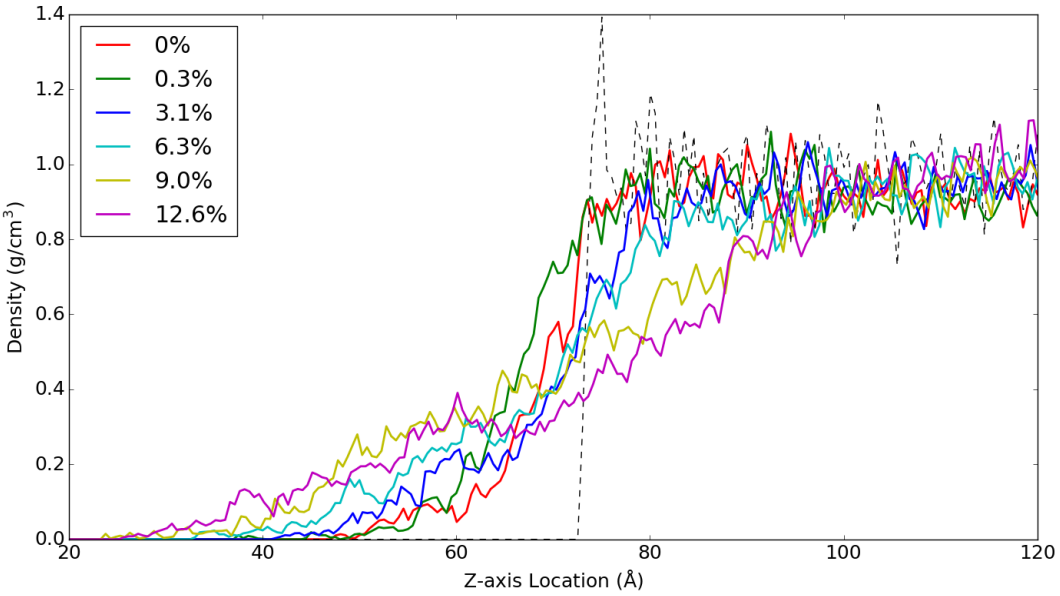

(a)

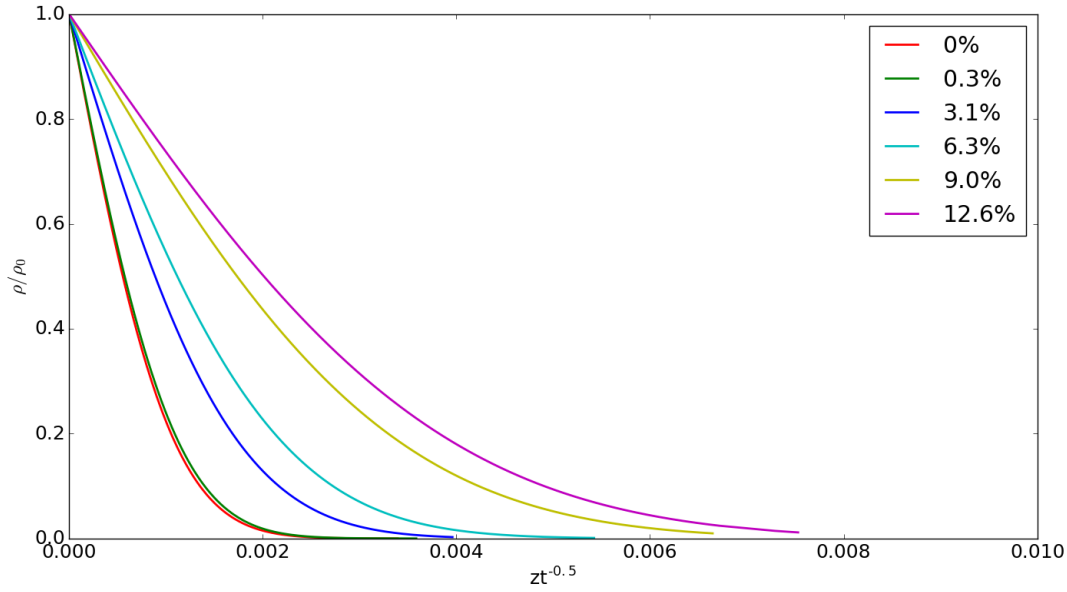

(b)

Figure 4.8: (a) Density profile plots for ethylene glycol at 10 ns for different BER rates. The dotted line is the profile at 0 ns. (b) Fickian fits of the ethylene glycol diffusion profiles.

ns into simulations in which reaction rates are modified. The density profiles show that for faster BER rates the EG is able to penetrate into the polymer at a faster

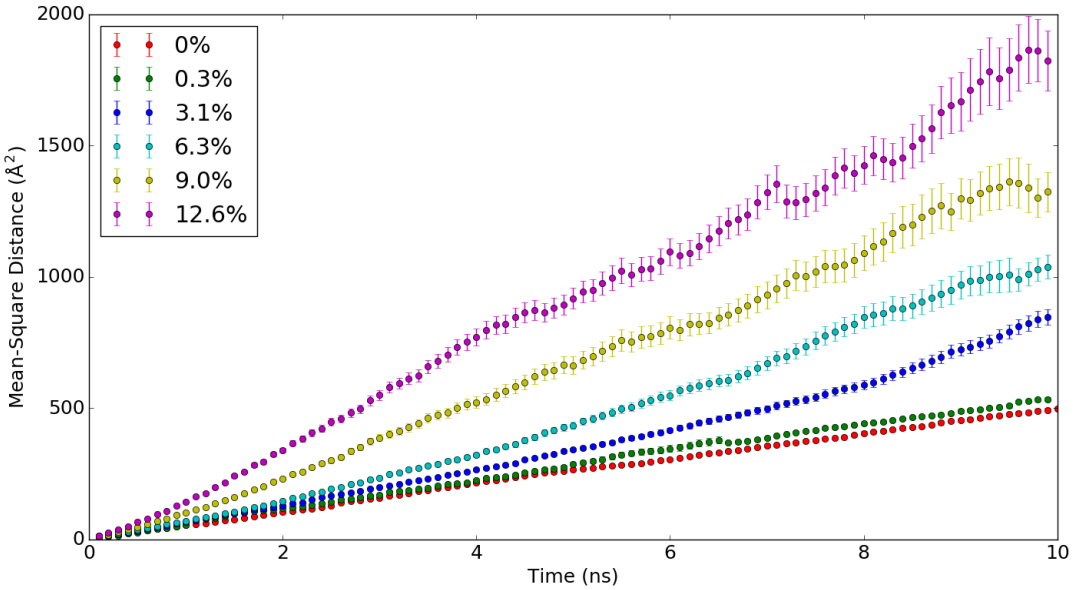

Figure 4.9: Diffusivity plots of the dangling ends within CANs at different BER rates showing that increasing the reaction rate increases chain mobility.

rate. The 1D Fickian diffusion equation can then be used to fit the density profiles to obtain diffusivity,

$$\rho(z,t) = \rho_0(1 - erf(\frac{z}{2\sqrt{Dt}})) \tag{4.1}$$

where ρ is the density at a penetration distance, z, and time, t, ρ_0 is the density at a penetration distance of 0, and D is the diffusivity. Plotting the EG diffusion data at 5, 6, 7, 8, 9, and 10 ns on a $\frac{\rho}{\rho_0}$ vs. $zt^{-\frac{1}{2}}$ masterplot allows fitting of the Fickian diffusion equation to obtain diffusivity. Table 4.1 gives the diffusion coefficients for the various systems. As BER rates increase so does the solvent diffusivity. At 9% BER rate, the solvent diffusivity is an order of magnitude greater than 0% BER rate.

Stress relaxation rates were determined by creating systems of CANs only. The systems consisted of 720 molecules of DGEBA and 480 molecules of TCA and crosslinked at 90%. They were stretched in the z-axis to 50% strain in the NPT ensemble with 0 atm pressure applied on the x and y axes to allow natural Poisson contraction. Stress relaxation simulations were run by holding the z-axis constant while applying 1 atm

Table 4.1: BER Rate Effect on Diffusivity

Search Radius (Å)	BER Rate (%/iteration)	k_e (MPa)	Relaxation Time at 450 K (ns)	EG Solvent Diffusivity (10^{-6} cm^2/s)	Dangling End Diffusivity (10^{-6} cm^2/s)
0.0	0.0	54.4	0.68	0.34	0.83
3.0	0.3	57.4	0.427	0.36	0.90
3.2	3.1	59.5	0.451	0.87	1.26
3.3	6.3	50.9	0.689	1.37	1.65
3.4	9.0	41.2	0.828	3.30	2.32
3.5	12.6	18.7	1.29	4.45	3.12

pressure on the x and y axes in the NPT ensemble [98] at 450 K and performing the BER reaction scheme for 25 iterations (5 ns total simulation time). At each pair search radius the characteristic relaxation time can be obtained from the Maxwell form of the standard linear solid model,

$$\frac{\sigma(t)}{\epsilon_0} = k_e + k_1 exp(-\frac{t}{\tau}) \tag{4.2}$$

where σ is the stress at time, t, ϵ_0 is the initial strain, k_e and k_1 are constants related to glassy and rubbery moduli of the material, and τ is the characteristic relaxation time. The characteristic relaxation time can be obtained through fitting this equation to the stress versus time graphs for each reaction rate. Table 4.1 gives the stress relaxation values for each BER rate and k_e or the elastic constant. It can be seen that with higher rate of BER the material flows more, behaving more viscous as the value of k_e falls.

4.3 The Role of CAN-CAN and CAN-EG Interactions in Diffusion

To isolate the role of network breakage through CAN-EG (DISS) bonds versus the role of CAN-CAN (BER) bonds in solvent diffusion, four simulations were run. One in which the BER bonds were turned off but DISS reactions could occur (decreasing crosslink percentage), one in which BER bonds were turned on but DISS reactions could not occur (constant crosslink percentage), one with no BER or DISS reactions

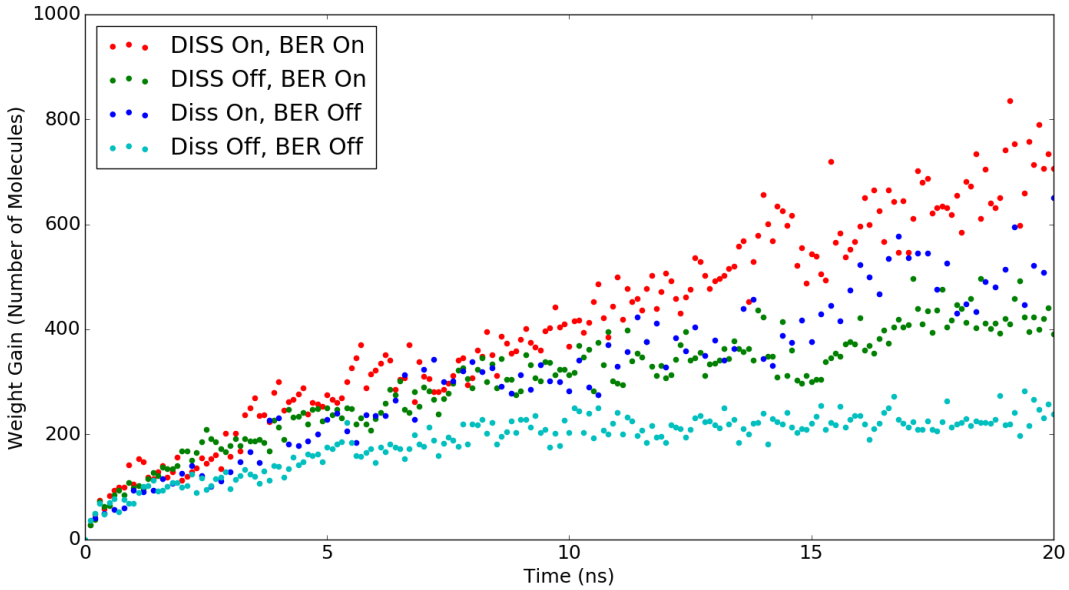

(a)

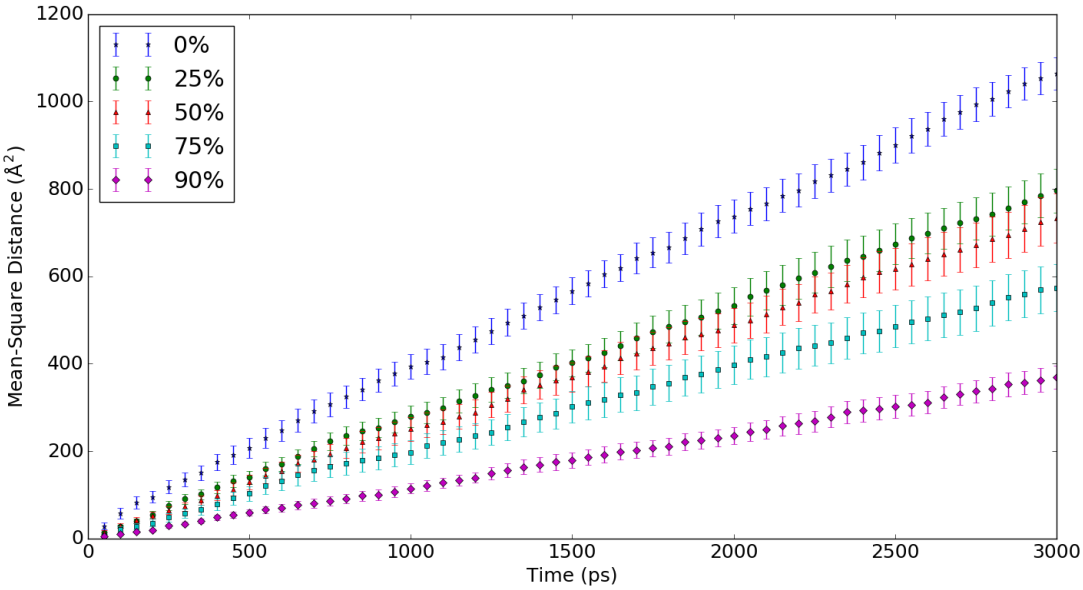

(b)

Figure 4.10: (a) Weight gain measured as number of molecules diffused past CAN front showing different effects of dissolution and BER reactions. (b) Ethylene glycol diffusivity increase as a function the degree of crosslinking.

allowed, and one with both allowed. Figure 4.10a shows the weight gain of EG for all situations as measured by the number of EG molecules beyond the polymer front.

It is found that weight gain in bulk CAN is roughly equivalent after 20 ns for BER on, DISS off and BER off, DISS on suggesting the increased mobility of dangling ends with BER turned on has a similar effect on EG diffusion as network degradation caused by DISS reactions. In this system, as the network bonds to diffused EG there is a gradual decrease in the crosslink density in the CAN. Without the constraining crosslink centers, the CAN chain mobility increases creating more free volume and allowing solvent molecules to diffuse faster. Figure 4.10b demonstrates the increased diffusivity of EG as a function of crosslink density. In contrast, forming BER bonds does not alter the crosslink density but allows faster EG diffusion through network mobility. These two simulations roughly mirror the two situations encountered in experimental studies. One in which catalyst is distributed throughout the CAN network and BER would be occurring throughout the entire dissolution process and one in which catalyst is only contained in the solvent and therefore reactions occur according to the concentration of solvent diffused into the CAN.

4.4 Network Degradation Mechanism

CANs have an infinite molecular weight if they have sufficient crosslink density to create a complete network, often called a gelation point. The gelation point is the critical crosslink percentage required for complete network formation and is described by,

$$p_{gel} = \frac{1}{\sqrt{r(f_a - 1)(f_b - 1)}} \tag{4.3}$$

where f_a and f_b are the functionalities of monomers a (DGEBA) and b (Tricarballylic acid), respectively, and r is the stoichiometric imbalance, or N_a/N_b. Using this equation the gel point of the system, with 85% degree crosslinking, is found to be 0.52. When modeling network degradation if the p-value, or the ratio of unreacted crosslinked sites to total crosslink sites, falls below 1-p_{gel} then the network is physically broken. As the EG diffuses into the CAN network it reacts with the crosslinked

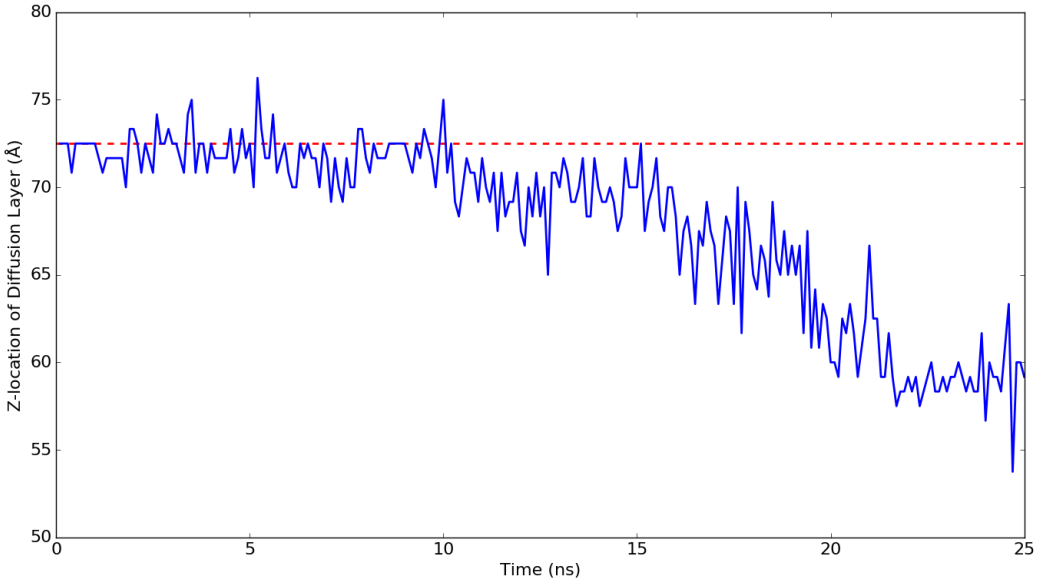

Figure 4.11: Location of the degradation front as measured by gel theory throughout dissolution simulation. The dotted red line is the initial boundary between solvent and polymer.

sites, breaking them and resulting in decreased p-value. The degradation front can be tracked by measuring the p-value at regular intervals throughout the simulation. The p-value is measured in 2.5 Å high slabs through the z-axis. The first slab in the CAN which has a p-value below 1-p_{gel} is taken as the degradation front location, shown in Figure 4.11. Figure 4.12 gives a snapshot of the simulation in which the network is partially broken.

In experimental results, an initial mass increase is indicative of initial polymer swelling and diffusion of EG with insufficient DISS bond reactions to result in a broken network. This behavior is also seen in Figure 4.11. There is an initial period in which insufficient bonds have been cut by DISS reactions and therefore the location of the broken slab in the network is at the original interface. During this process EG are diffusing into the network creating swelling. After some time, sufficient EG has diffused into the network to begin complete degradation and the polymer begins to have mass loss (network breaking).

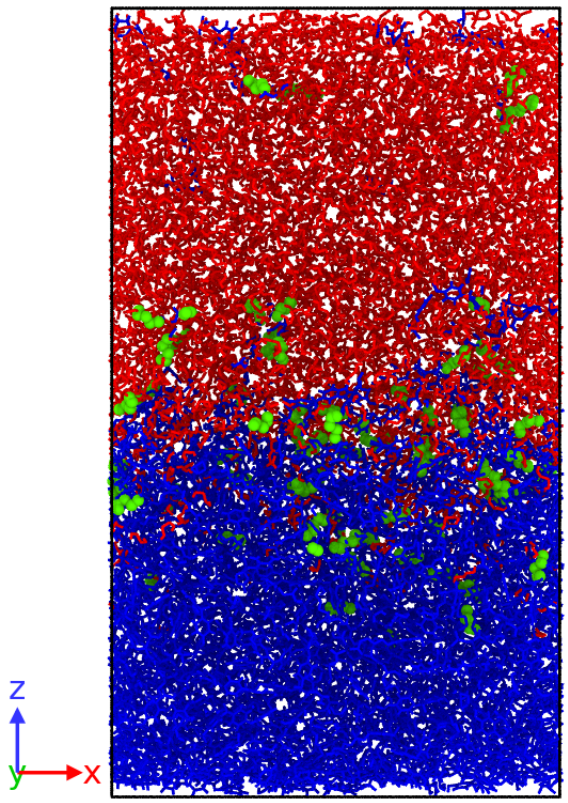

Figure 4.12: Snapshot of the simulation at 13 ns. Red bonds are the CAN network, blue are ethylene glycol, and green atoms are ethylene glycol molecules which have formed bonds with the CAN network. CANs and unreacted EG are represented with bonds only, while reacted EG is represented with bonds at atoms for visualization purposes.

The network swelling prior to degradation can be explained in two ways. Initially, when a crosslink center is cut by a DISS bond, the TCA molecule still has two other crosslinking centers where it can be attached to the rest of the network. As more DISS bonds occur the probability of a TCA molecule remaining attached to the network decreases until a critical point is reached in which mass loss will occur with each new DISS bond reaction. Similarly, a second possible explanation involves reforming of the network. If a polymer chunk is cut from the network by DISS bonding, it is still possible to form a BER and reattach to the network at a later time using a different, unreacted crosslinking center on the chunk. Since the chunk diffusion out of the network is even slower than EG diffusion into the network this likelihood is high, especially at the beginning of diffusion. As more and more of the network is broken the chunk diffusivity increases due to the increase of chain mobility with decreased number of crosslinks. Therefore, as time goes on the probability of reattaching to the network decreases and the mass loss becomes constant.

4.5 Critical EG Concentration for Dissolution

It is not necessary for all crosslink sites to bond with an ethylene glycol molecule to completely degrade the network. Larger chunks can diffuse away from the bulk network. The complicated topology of larger chunks means that it may take significant time to diffuse away from the polymer network, or may need to be degraded into smaller chunks. The size of the chunks freed from the network were monitored throughout the simulation and plotted as a histogram in Figure 4.13. A chunk was detected by using a tree-search algorithm that set the root as the crosslinking center that participated in a DISS reaction. The algorithm then uses the bond topology information to build the tree representing the potential chunk structure. A cutoff size of 30 molecules was used to eliminate capturing overly large portions of the total simulation size. The algorithm also takes into consideration BER reactions and

the possibility of a chunk rebonding to the bulk CAN network. The most frequent size of a freed chunk was approximately three to five molecules in total size. This is consistent with the theoretical value of 2.67 derived from gel theory.

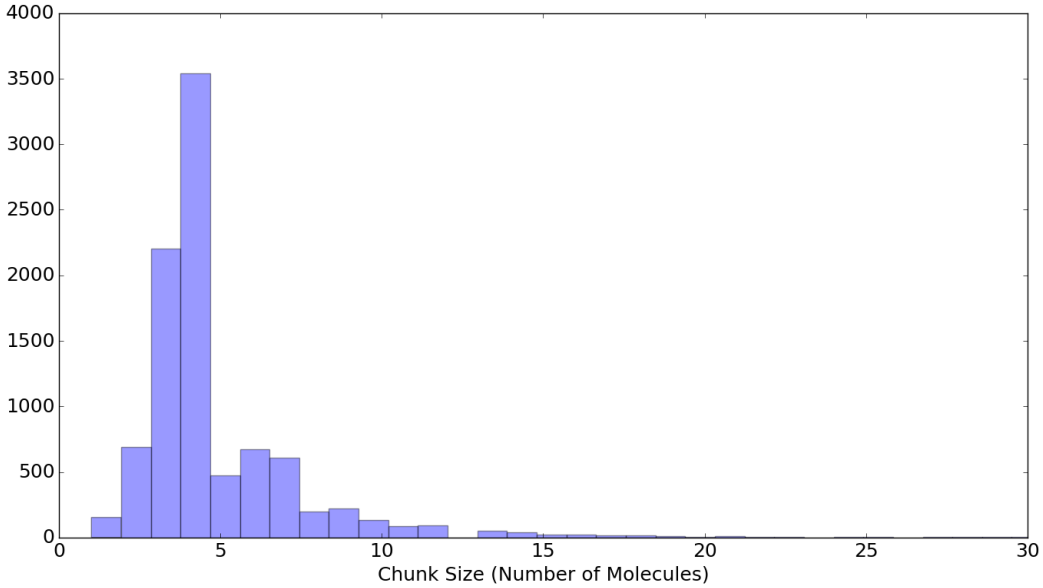

Figure 4.13: Histogram of the size of chunks freed from the network represented as the number of individual monomeric units within a chunk.

Furthermore, given that the probability of a chunk reforming to the network decreases as the crosslink density decreases from DISS bond formation and that typical chunk sizes are greater than a single molecule, there should be a critical concentration of EG that will degrade the network that does not correspond to a 1:1 ratio of crosslinking sites to EG hydroxyl groups. An understanding of the critical ethylene glycol concentration can be achieved by monitoring the concentration of EG as a function of the p-value within slabs during the simulation. Figure 4.14 shows as the ethylene glycol concentration within a slab increases the p-value decreases. Simply, if there is higher concentration of EG there is greater probability it will react with the network. At the critical p-value of 0.48, or 1-p_{gel}, the EG concentration is approximately 35-40%, indicating this may be the critical concentration to achieve a broken

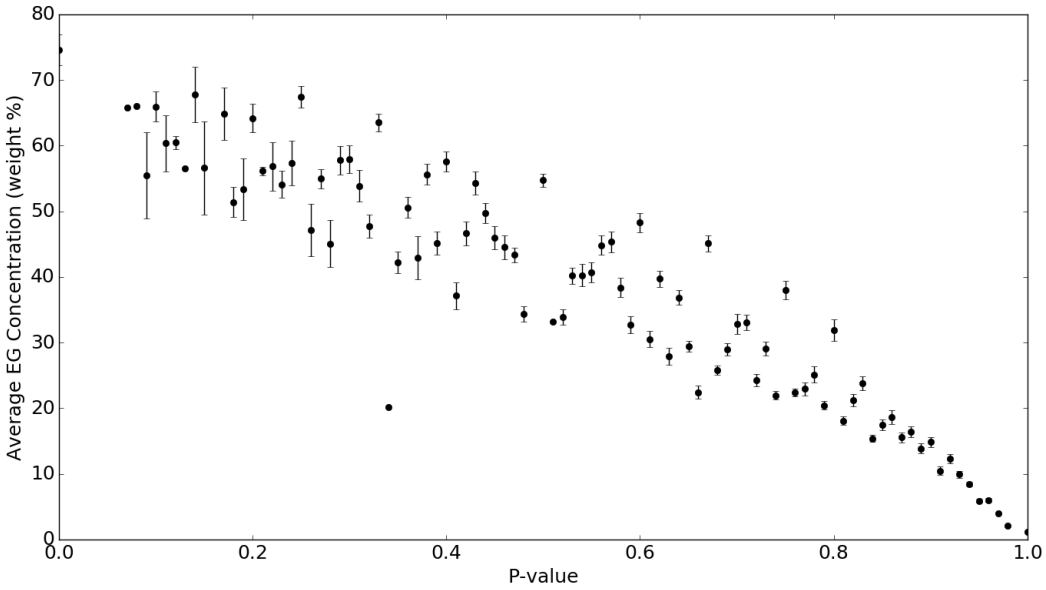

Figure 4.14: P-value as a function of the concentration of ethylene glycol.

network.

4.6 The Competing Roles of Crosslink Density and Bond Exchange Reactions

It is known that crosslink density plays a critical role in the thermomechanical properties of traditional thermosets and also affects CANs. However, there is a competing role that crosslinking and bond exchange reactions play in stress relaxation behavior and dissolution behavior within CANs. First, since exchange reactions occur at crosslinking sites, the higher the crosslinking density the more reactions that will take place under given conditions. This may contribute to faster, or more complete, relaxation behavior and faster dissolution rates as chain mobility will likely be higher with a higher BER rate. Second, lower initial crosslinking within the system will naturally produce higher chain mobility from the reduced network constraints. It is expected that at some critical crosslink density, the bond exchange reaction contribution to chain mobility overtakes the contribution from low crosslink density. The goal of this

section is to explore the role of crosslinking density and bond exchange reactions in the stress relaxation behavior and solvent diffusivity within a covalent adaptable network. The relationship between free volume, crosslinking, and diffusivity is developed.

4.6.1 Tensile Stress

For calculating tensile stress and glass transition three separate models were created as described in section 4.1.3. During the crosslinking process for each model a structure was output at 26%, 51%, 76%, and 90% degree of crosslinking. This created three different structures at each crosslink density. Tensile strain simulations were performed on all structures at 450 K. The strain rate was $10^9\,s^{-1}$ in the z-direction with 0 atm pressure applied in the x and y directions to allow natural Poisson contraction as the sample is strained. The total strain was 50%. Figure 4.15 shows the stress/strain curves generated for all degrees of crosslinking. Elastic modulus is higher

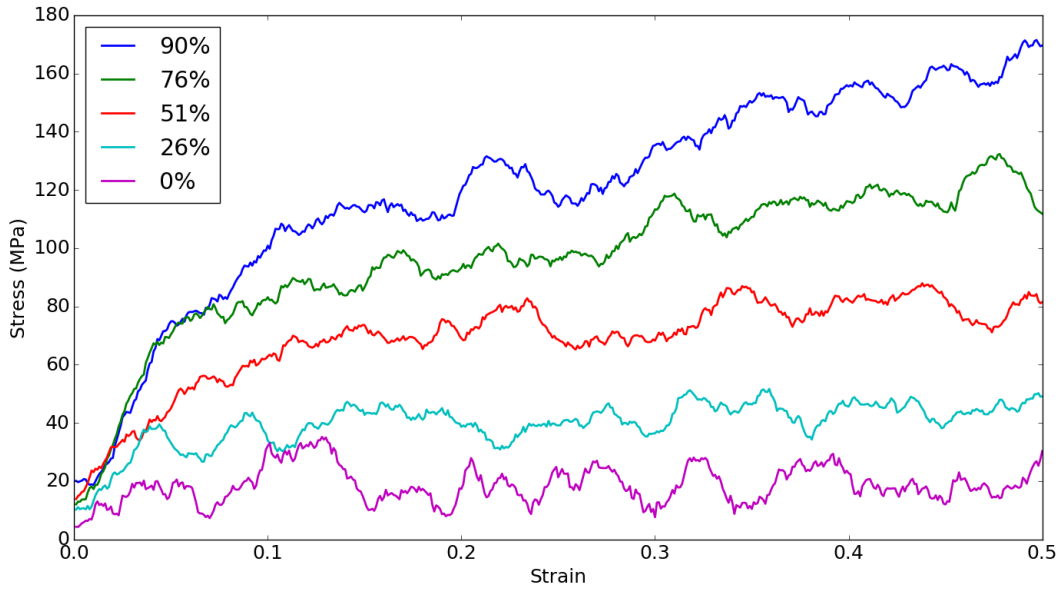

Figure 4.15: CAN stress/strain curve at different crosslink densities generated from averaging data across three different simulations and applying a Savgol Filter with polynomial degree of 3 for data smoothing.

for 76% and 90% crosslink. The ultimate stress and yield stress of each sample follow

the crosslinking degree, with 90% the highest and 0% the lowest. Not surprisingly the 26% sample exhibits low yield stress with near no strain hardening. The theoretical gel point is a crosslink degree of 58% and therefore this sample would perhaps contain a loose network with many unattached small molecules.

The free volume of a network has previously been related to the glass transition [99] and yield stress [100] in molecular dynamics simulation of polymers. In both studies there was good agreement correlating fractional free volume and void shape to thermomechanical system properties. The free volume can be measured using the hard sphere probe method throughout the tensile simulations [101]. The hard sphere probe method involves discretizing the simulation volume into small voxels. If a probe inserted at the voxel center is within a certain distance of an atom, the voxel is determined to contain the atom. The free volume fraction is the volume ratio of unoccupied voxels to total voxels. In this study, the distance from the center of an atom to determine the occupied state was $R = 0.88R_{vdw} + R_{probe}$, where the van der Waals radius was taken from the OPLS forcefield parameters. Both the voxel size and probe size can effect the overall measurement of free volume. In order to determine their effects free volume was calculated on one system with multiple parameters. Figure 4.16 shows the results. Little difference in free volume is seen for a probe size greater than approximately 1 Å. 1 Å is used hereafter as it is close to the probe size in the experimental free volume measurement technique, Positron Annhilation Light Spectroscopy (PALS). Voxel discretization did not see any significant free volume changes below approximately 0.25 Å and is used hereafter.

Figure 4.17a shows the change of free volume as a function of strain for the different crosslinked systems. The equilibrated structures, at 0% strain, show decreasing free volume with increasing crosslink degree. Interestingly as the systems are strained the free volume becomes greater with higher degree of crosslinking. At 50% strain, the trend has reversed from equilibrium, with 90% crosslinking showing the highest free

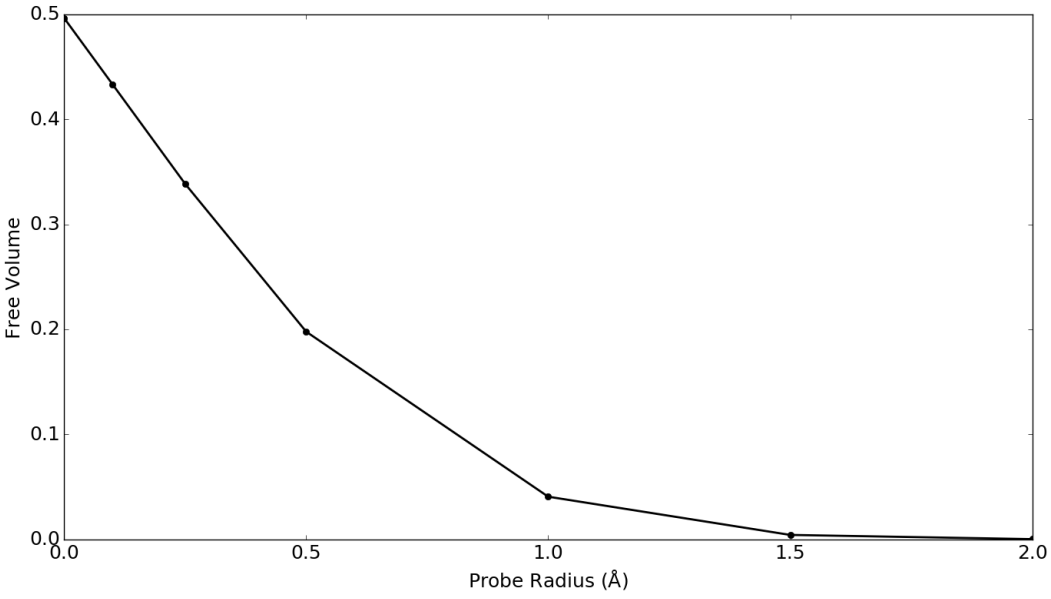

(a)

Figure 4.16: Determination of the free volume parameters (a) probe size and (b) voxel side length for the hard sphere probe method.

volume fraction and 25% the lowest. This can be attributed to the relaxation ability in lightly crosslinked structures. For example, the 26% degree is a loosely connected structure allowing individual molecular segments to rearrange. This is evident in the fact that free volume changes modestly with strain. The increase of free volume in highly crosslinked structures is likely from smaller voids coalescing to form larger voids.

Further, the size and shape of voids can be monitored. To monitor shape change, free voxels in euclidean space determined from the hard sphere probe method were clustered using the HDBSCAN algorithm implemented in Python [102]. This is an unsupervised clustering technique that does not require input of the number of clusters. The algorithm uses distance between points as the cluster separation criteria and allows the user to define the minimum acceptable cluster size. The volume of the clusters could be determined simply by multiplying the number of voxels in a given cluster by 0.25^3 Å^3. The surface area of the clusters was approximated by using the

Table 4.2: Void Shape Changes during Tensile Stress for the 90% Crosslinked System

Void Size (Å^3)	Number of Voids		SA to V Ratio		Shape Factor, w	
	0% Strain	50% Strain	0% Strain	50% Strain	0% Strain	50% Strain
<2.5	1755	3556	19.71	21.87	2.51	2.39
2.5-5	182	121	9.17	9.03	2.86	2.85
5-10	166	113	7.65	7.30	3.02	2.87
10-20	117	96	6.63	6.47	3.29	3.19
20-40	85	65	5.95	5.64	3.78	3.55
40-60	28	28	5.23	5.08	3.96	3.86
60-100	20	28	5.83	5.02	5.15	4.37
>100	22	44	5.42	4.54	5.81	5.84

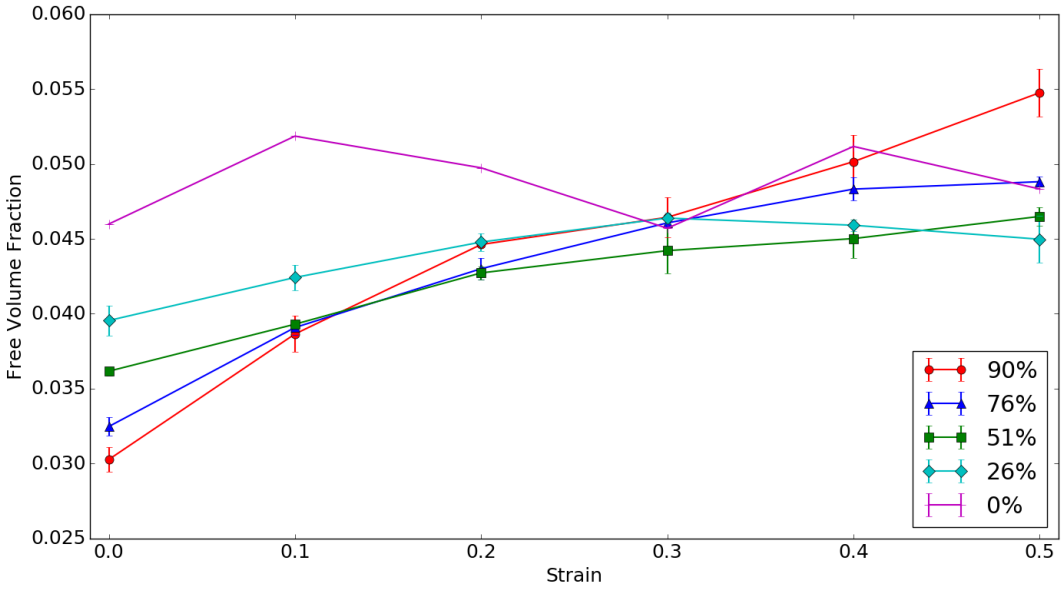

(a)

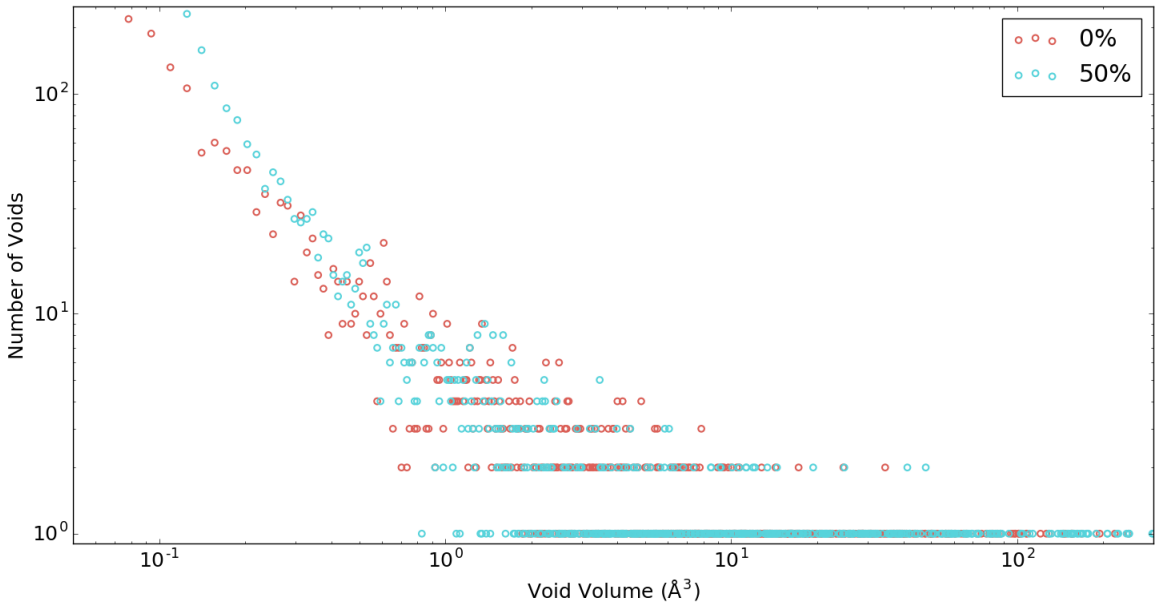

(b)

Figure 4.17: (a) Free volume as a function of strain for various degrees of crosslinking and (b) number of voids for a given void volume at different strains.

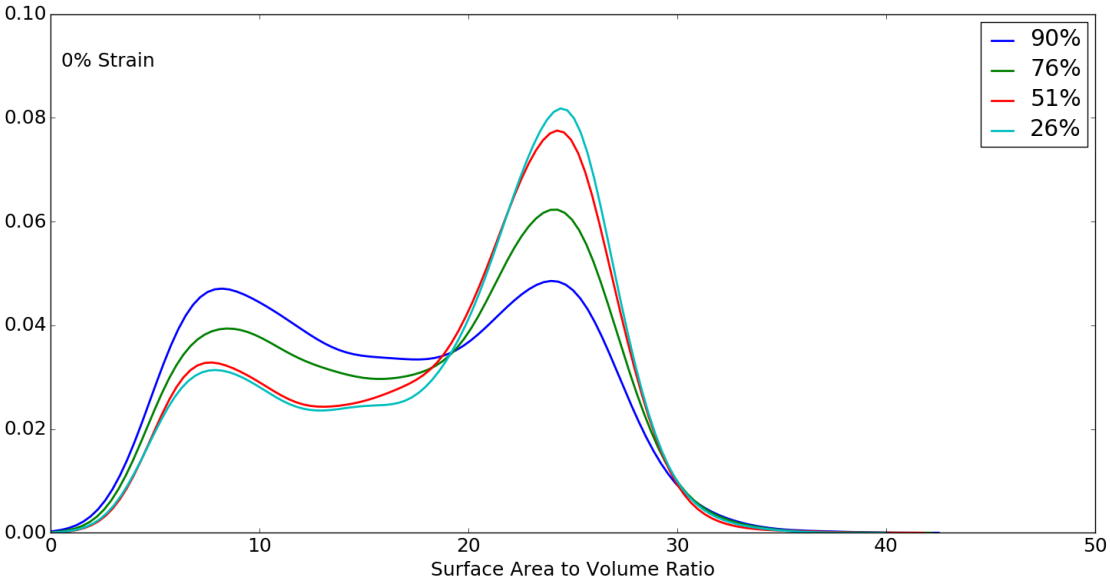

(a)

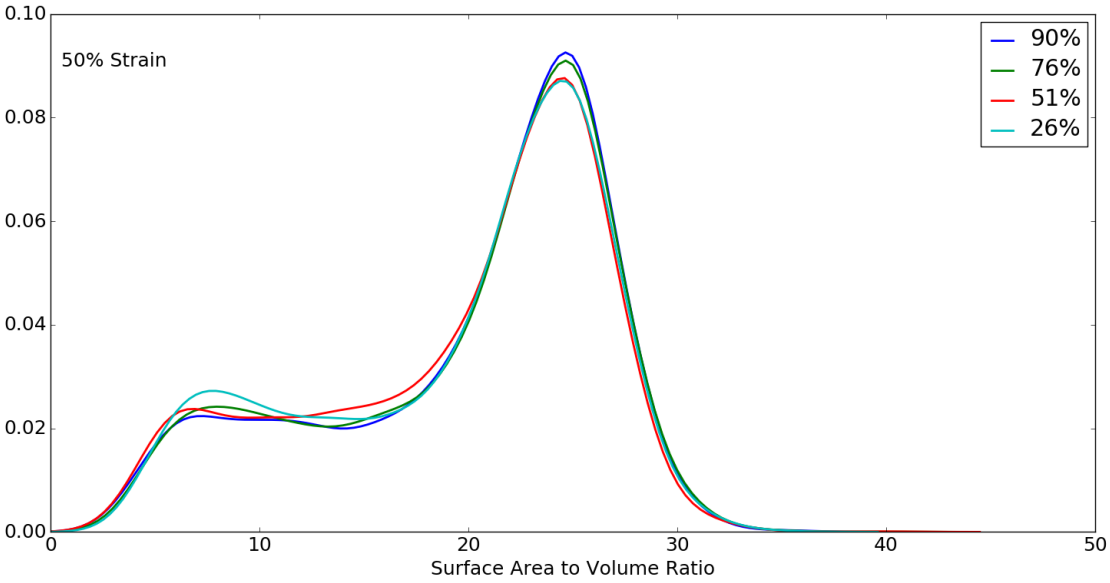

(b)

Figure 4.18: Surface area to volume ratio of individual voids for each of the crosslinked systems at (a) 0% strain and (b) 50% strain.

marching cubes algorithm of Lewiner [103] to create a surface mesh of the cluster (void). This method is reported to accurately assess surface area of concave voids

and the authors report a maximum of 4% error on a wide variety of shapes. A shape factor is determined taking the surface area to volume ratio of the void. In general, a large SA:V ratio indicates small or irregularly shaped clusters. A larger ratio also indicates higher deviation from spherical. Figure 4.18 shows the distribution of the surface area to volume ratio as a function of crosslinking and strain. At 0% strain there is a higher percentage of small SA to V ratio voids in the 90% sample. The 26% crosslinked sample has a higher percentage of large SA to V ratio voids. The distribution of void shapes and quantities are given in Table 4.2. The shape factor, w, in this table is given by the equation,

$$w = (SA/4\pi)/(3V/4\pi)^{2/3} \tag{4.4}$$

where SA is surface area and V is volume. The w factor is a way to measure deviation in void shape from spherical. The larger overall volume and loose network structure likely creates many small sized, irregularly shaped voids contributing to high SA:V ratio. When the system is strained to 50% all systems follow a somewhat similar SA:V ratio distribution with higher values of the ratio. The fact that the void shape factor distribution is nearly the same for all samples indicates that free volume shape may be dominated by the strain experienced by the system, not necessarily the system structure.

4.6.2 Glass Transition Temperature

The glass transition behavior is measured by cooling the sample from 450 K to 250 K at 0.1 K/ps cooling rate under NPT ensemble. Polymers experience different coefficients of thermal expansion above and below their glass transition temperature. The glass transition temperature is obtained by plotting specific volume versus temperature for each of the samples during the cooling simulation, seen in Figure 4.19. A piecewise linear fit with two regions is then used and the intersection of the two linear regions corresponds to the glass transition temperature. The glass transition

temperatures for the different crosslink degrees are given in Table 4.3. As expected, with more crosslinks the chains experience decreased mobility and, thus, the higher the crosslink density the higher the glass transition temperature. The values are approximately in the range of reported experimental values ranging from 30°C to 60°C. It is well documented that higher cooling rates in MD result in inflated T_g values. As Li and Strachan [44] report a 3 K correction per decade of increased cooling rate is an appropriate correction. This would correspond to a 30 K correction for the measured T_g values, which puts the values of Table 4.3 precisely in line with experimental work.

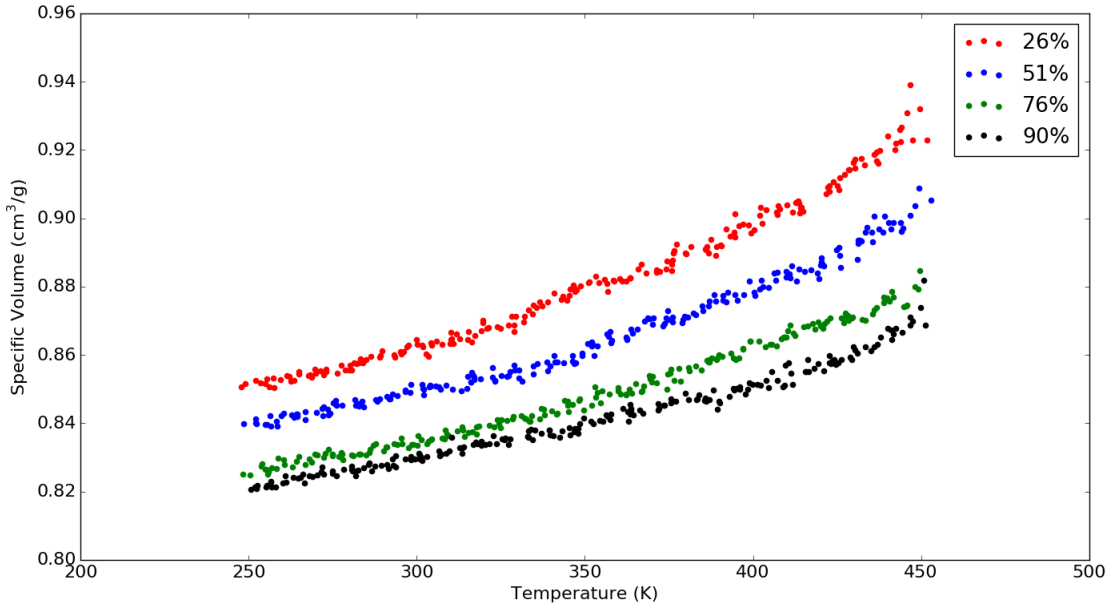

Figure 4.19: Specific volume versus temperature during cooling simulation of CAN at 0.1 K/ps cooling rate at different crosslink degrees.

It is also important to note that higher crosslink densities exhibited a lower specific volume. The network structure becomes more compact as free volume is reduced. Free volume distributions within the network can be measured using Voronoi tessellations. Voronoi tessellations create a polygon around each atom in which the faces represent nearest neighbors. The larger the volume of the polygon surrounding each atom, the more free volume surrounding the atom. A distribution of the free volumes for the DGEBA monomer helps explain the reduced specific volume with increasing crosslink

Table 4.3: Glass Transition Temperatures for CAN

Crosslink Degree	T_g
26%	326 K
51%	331 K
76%	335 K
90%	343 K

density. The distribution of tessellation volumes for backbone atoms versus epoxide end group atoms was created for 51% crosslink density. If the DGEBA epoxide end was crosslinked it was included as a backbone atom. As can be seen in Figure 4.20 the un-crosslinked end groups contribute to nearly all of the higher cell volumes throughout the distribution.

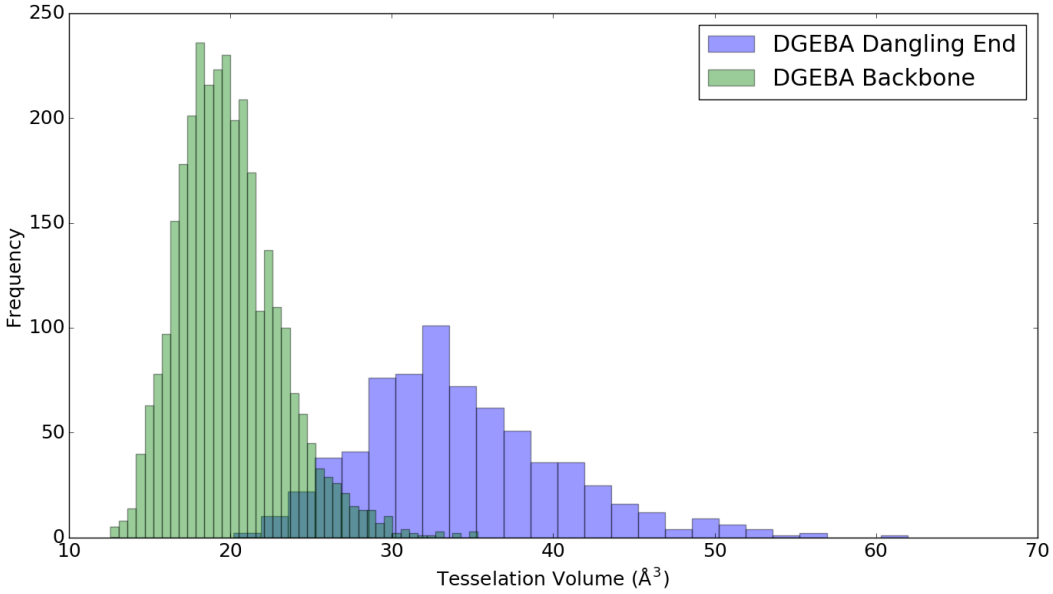

Figure 4.20: Distribution of Voronoi tessellation volumes for 51% crosslinked CAN DGEBA backbone and dangling end carbons.

4.6.3 Stress Relaxation Behavior

Simulations of the 50% strained samples underwent simulation with the BER turned on and off in the NPT ensemble at 450 K to measure stress relaxation behavior. The stress relaxation with the BER bonds turned off is seen in Figure 4.21 and was performed for 500 ps with 1 atm pressure applied in x and y and the z axis held fixed to mimic a typical stress relaxation test. The chain relaxation becomes stagnate after approximately 200 ps and the system retains significant stress values. For example, the 90% crosslinked sample maintains a stress above 100 MPa.

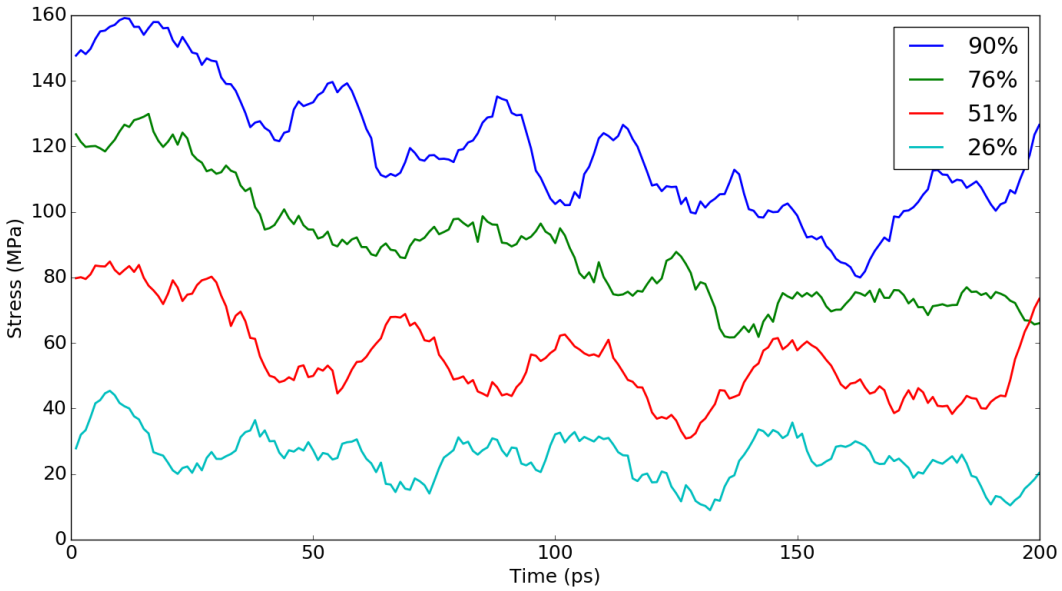

Figure 4.21: Stress relaxation with the BER turned off.

The stress relaxation for the 90% crosslinked sample was performed with BER turned on. The simulation was carried out for 10 ns with the NPT ensemble applying 1 atm pressure in the x and y directions and holding the z-direction fixed. Over the course of 10 ns the stress continues to gradually decrease approaching 20-40 MPa, as seen in Figure 4.22. The stress relaxation graph can then be fit to the Maxwell form

of the Standard Linear Solid model equation,

$$\sigma(t) = \epsilon_0 k_e + \epsilon_0 k_1 * exp(-t/\tau) \tag{4.5}$$

where ϵ_0 is the strain held during relaxation, t is time, τ is characteristic relaxation time, and k_e and k_1 are constants related to glassy and rubbery moduli of the material. The characteristic relaxation time, τ, is determined to be about 1.7 ns which is in line with previous work [77].

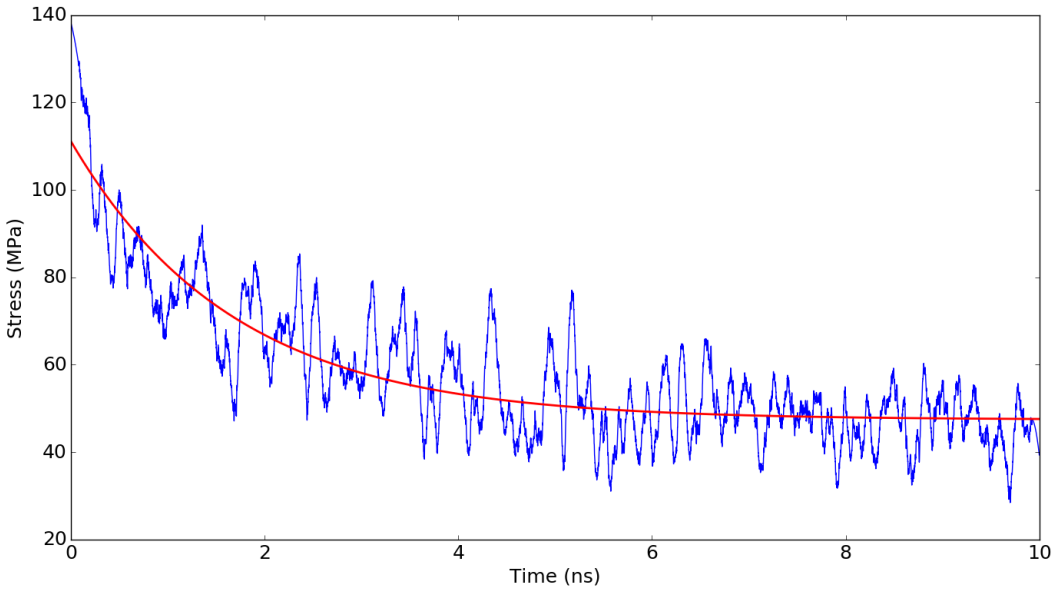

Figure 4.22: Stress relaxation with the BER turned on for the 90% crosslinked sample.

The free volume was measured at regular intervals during the BER simulation and is seen in Figure 4.23a. The free volume fraction drops over the course of 2 ns until is reaches steady state of approximately 0.035, which is approximately the value at 0% strain, indicative of stress recovery as evidenced by the majority of relaxation occurring within 2 ns in Figure 4.22. After relaxation without BER, the system showed free volume fraction of approximately 0.043, proving network rearrangement from the BER process leads to reduction in overall free volume fraction.

Further, the shape of voids is shown in Figure 4.23b. There is an initial return to smaller SA:V ratio values over the first 1 ns. At 10 ns the trend continues with

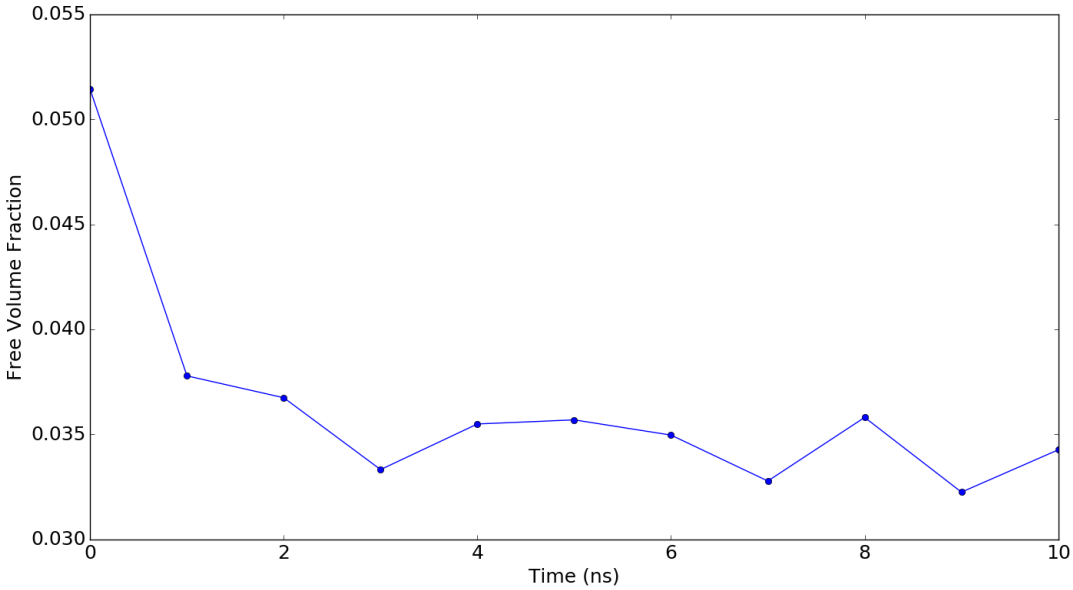

(a)

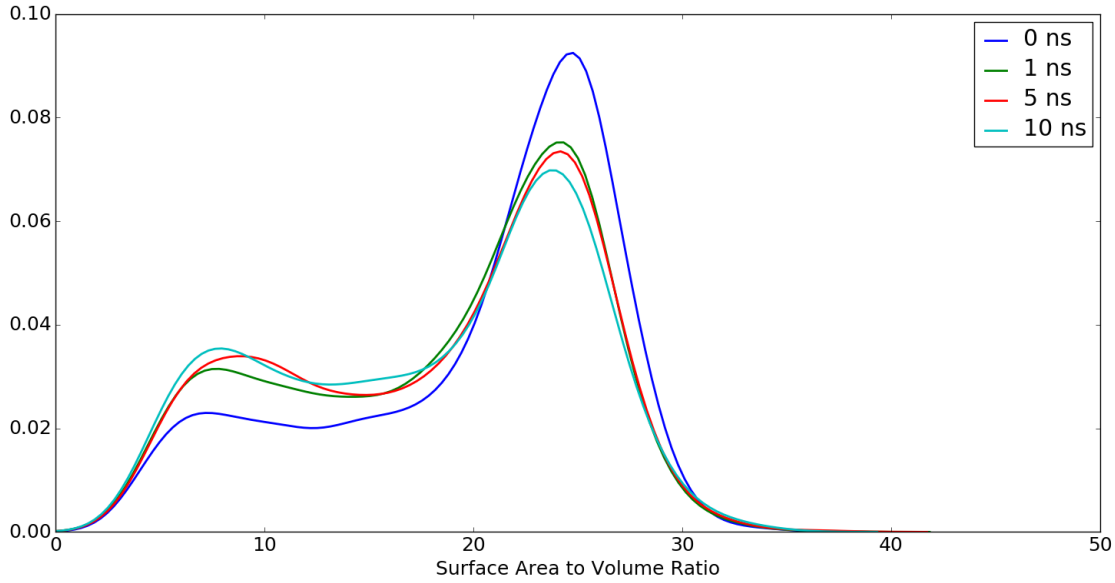

(b)

Figure 4.23: (a) Fractional free volume as a function of time during stress relaxation simulation and (b) surface area to volume ratio distribution plots during stress relaxation.

formation of smaller SA:V ratio voids, indicative of larger and more regularly shaped voids. Given significant time for network rearrangement the return to a distribution

Table 4.4: Void Shape Changes during Relaxation for the 90% Crosslinked System

Void Size (Å^3)	Number of Voids		SA to V Ratio		Shape Factor, w	
	50% Strain	10 ns Relaxation	50% Strain	10 ns Relaxation	50% Strain	10 ns Relaxation
<2.5	3556	2589	21.87	20.66	2.39	2.43
2.5-5	121	174	9.03	8.96	2.85	2.78
5-10	113	151	7.30	7.44	2.87	2.96
10-20	96	122	6.47	6.48	3.19	3.2
20-40	65	91	5.64	5.97	3.55	3.77
40-60	28	30	5.08	5.28	3.86	3.97
60-100	28	19	5.02	5.47	4.37	4.79
>100	44	30	4.54	4.91	5.84	5.45

similar to 0% strain (see Figure 4.18a) is likely. The free volume distribution and shape can thus be used as a metric for stress relaxation behavior in CANs. It is seen in Table 4.4 that small sized voids are most prevalent in the structure and contribute to the majority of larger SA:V ratio voids. At 0% strain these voids have an average SA:V ratio of 7.49, at 50% strain this rises to 9.62 as the voids become more irregularly shaped and smaller voids are produced. After 10 ns of relaxation the ratio drops to 8.63 as network rearrangement from BER reactions relaxes the system.

4.6.4 Solvent Diffusion

Thermomechanical models with 1 weight % EG concentration and at different crosslink degrees were created to measure differences in diffusivity due to BERs and crosslinking degree. The difference in diffusivity with crosslink degree was measured by allowing EG to diffuse freely without reaction while BER reactions were occurring in the CAN. Diffusivity plots are seen in Figure 4.24. The results show that lower degree of crosslinking contributes to higher mobility of EG from increased chain mobility. The diffusion coefficients can be calculated from MSD vs. time graphs according to the Einstein diffusion equation,

$$D = \frac{\langle [r_i(t) - r_i(0)^2 \rangle}{6t} \tag{4.6}$$

Table 4.5: Diffusivity and Free Volume in CANs

System	FFV	Diffusivity (x10^{-6} cm^2/s)	Diffusivity with BER Off (x10^{-6} cm^2/s)
0%	0.0476	5.79	5.79
26%	0.0405	4.39	4.81
51%	0.0365	4.06	3.70
76%	0.0336	3.19	3.05
90%	0.0319	2.05	1.92

The values of D are reported in Table 4.5.

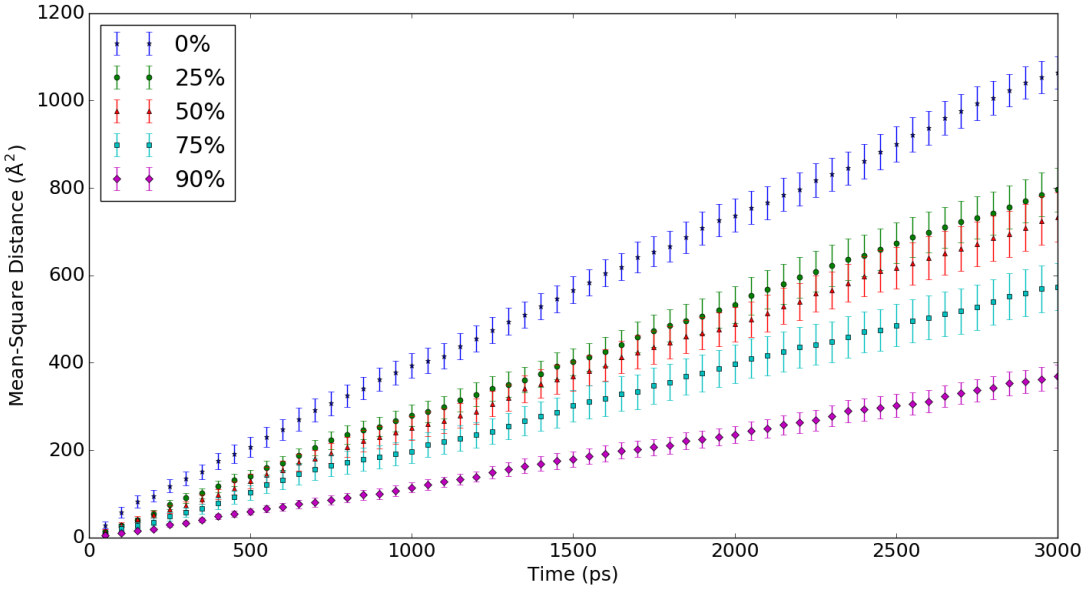

Figure 4.24: Dissolution behavior of EG in CAN with varying degree of crosslinking.

The role of BER in diffusion can be isolated by also measuring diffusivity of EG when the BER reactions are turned off at each of the varying crosslinked systems. The same systems were run for 1 ns in the NVT ensemble without BERs. The obtained diffusion coefficients are seen in Table 4.5. As the values show, BER increases the diffusivity for each system except the 0% and 26%. This suggests that BER has little benefit to the chain mobility with a loosely connected network that is well below the

gel point. The higher crosslinked structures show decreased diffusivity with the BER turned off suggesting that the network rearrangement contributes to higher diffusion rates.

One of the main useful qualities of CANs are their recyclability. They can be dissolved in solvent and then subsequently reformed for further use. However, some detriment of mechanical properties is likely as a result of residual solvent not completely evaporated from the network before the re-polymerization phase. Here, the effect of ethylene glycol solvent concentration on the mechanical properties was investigated to mimic possible structure detriment as a result of residual solvent during re-polymerization. The solvent concentration was varied from 0%, 1%, 10%, 25%, and 40% EG concentration. The solvent was not bonded to the network and simply its effect on presence within structure studied. The effect of cutting the network with solvent mirrors the previous studies with varying crosslink degrees. Only one structure for each EG concentration was created. In order to achieve multiple simulations for averaging of stress, the systems were strained in the x, y, and z directions separately and the results averaged for each system. Figure 4.25 shows 0% and 1% concentrations have approximately equal stress responses. At higher EG concentrations the system begins to see a detriment to mechanical properties. This suggests that some degree of residual solvent can remain in the re-polymerized CAN with minimal detriment to mechanical properties.

4.7 Conclusions

This chapter studied the macromolecular properties of covalent adaptable networks during dissolution, tensile strain, stress relaxation, and cooling through T_g. The dissolution research sought to show the mechanisms of solvent diffusion and network degradation during dissolution of a CAN network. Increasing the BER rate

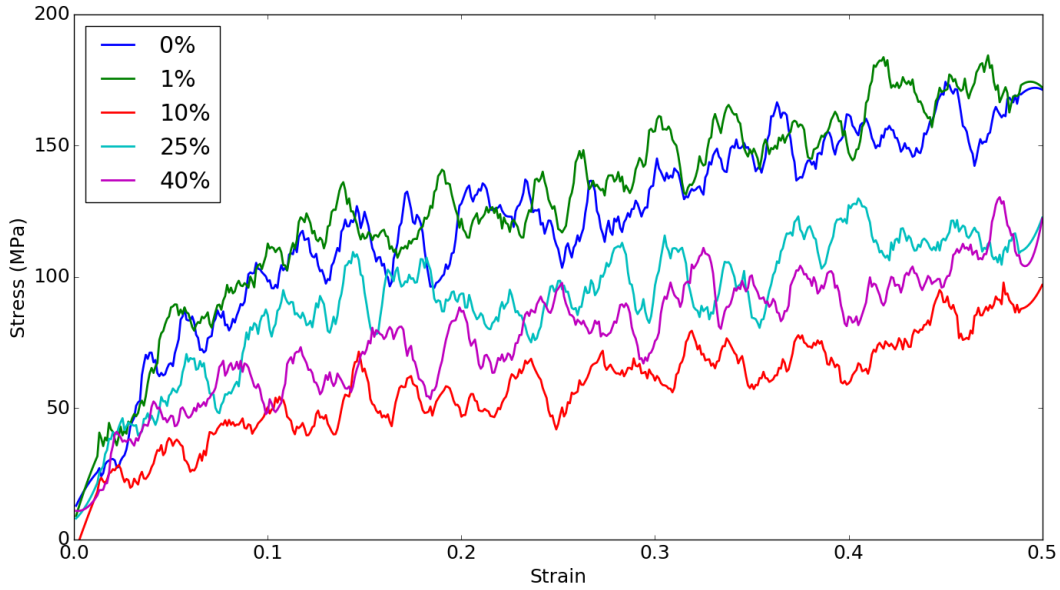

Figure 4.25: Tensile strain plots as a function of embedded ethylene glycol concentration.

was found to increase both dangling end intradiffusion and CAN-solvent interdiffusion. The BER rate can potentially be controlled through temperature or catalyst concentration. CAN-CAN (BER) and CAN-EG (DISS) bonding were found to approximately equally contribute to solvent penetration, while the network behaved like a traditional thermoset with no chemical reactions occurring. The degradation front was determined through use of gel theory and the size of chunks released from the CAN network matched theoretical predictions. This research is critical to understanding the diffusion mechanism within this new material class. Dissolution of these polymers presents the possibility of recyclable thermosetting polymers.

The thermomechanical properties research presented the foundation for understanding the competing roles of crosslink density and bond exchange reactions in covalent adaptable networks. FFV and the size and shape of voids was found to correlate with the stress of the system during tensile strain and stress relaxation. Additionally, the distribution of voids was found to change as a function of the degree

of crosslinking. BER leads to greater relaxation compared with traditional thermoset behavior as presented through a decrease in FFV and a gradual return to a non-strained SA:V ratio distribution. BER improved the solvent diffusivity within CAN only above the gelation point showing that enhanced chain mobility from BER is only beneficial in a highly crosslinked system. This work helps understand the topological underpinnings of covalent adaptable network behavior under different external stimuli.

Future work from this chapter could involve studying combinations of CAN/solvent systems to predict systems leading to efficient degradation. New systems have been proposed which result in network swelling before solvent reaction and the swelling behavior could be studied through this methodology. Additionally, CANs are being studied as potential matrices in composite systems to allow for recyclable or repairable composites. The interphase behavior of CANs in composites and the molecular topology during BER reactions in the presence of fillers should be studied to understand the macromolecular differences between CANs and a traditional matrix material.

CHAPTER V

STRUCTURE DEVELOPMENT IN REAXFF SIMULATIONS OF POLYACRYLONITRILE CARBONIZATION

Polyacrylonitrile (PAN) is the precursor used in most production of carbon fiber. Despite extensive experimental research there has been limited atomistic simulation work to understand the reaction mechanisms occurring during fiber production. However, reactive forcefields are well-suited to study high temperature pyrolysis and oxidation and provide detailed reaction pathways. Figure 5.1 gives a general reaction pathway from raw PAN to stabilized PAN and finally carbon fiber. It is a two step process first stabilizing the PAN through oxidation and then carbonization of the stabilized PAN to produce graphitic structures of carbon fiber. In this work bond-order based molecular dynamics through ReaxFF simulations will be used to study the reaction mechanisms and structure that results from carbonization of PAN. The influence of oxygen, molecular orientation, and temperature on the resultant structure will be compared.

Reactive forcefields have the benefit of modeling chemical reactions with bond forming and breaking. ReaxFF uses an energy computation at every timestep to determine the bond topology of the system. However, this means that timesteps must be on the order of fractions of a femtosecond so that atomic energy is updated faster than bond vibrations occur. ReaxFF is typically 10-50x slower than a standard Class I forcefield due to the small timesteps and force calculations. Furthermore, for many systems the rates of chemical reactions are not fast enough to yield meaningful results at realistic experimental temperatures during the nanosecond timescale that

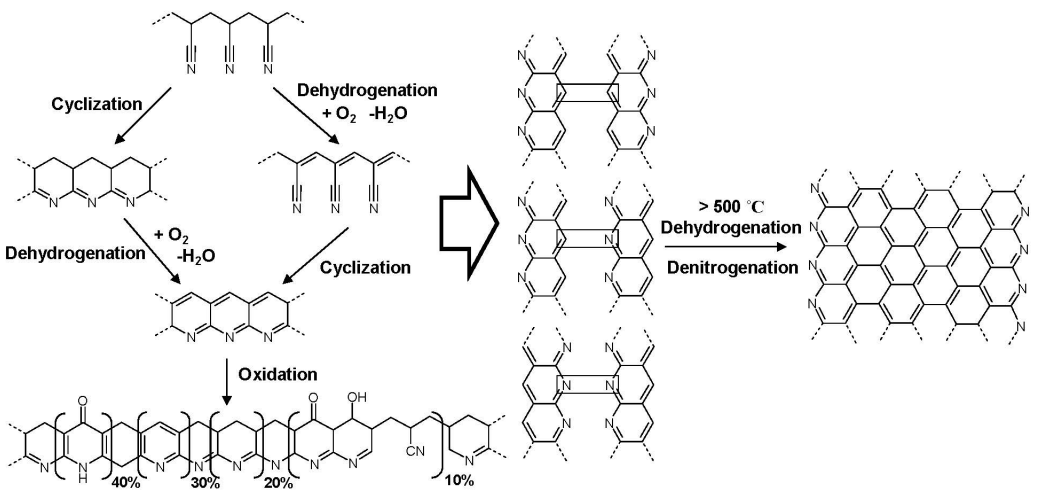

Figure 5.1: A proposed reaction pathway for obtaining carbon fiber from raw PAN.

ReaxFF simulations typically achieve.

There are different methods to address the issue of slow reaction kinetics. The most common technique is to use elevated temperatures to accelerate reactions. Lu et al. [104] used temperatures ranging from 2800-3800 K with ReaxFF to study pyrolysis mechanism in polyimide. Jiang et al. [105] used heating up to 4000 K to observe small molecule products during pyrolysis of phenolic resin. Whereas, experimental studies of phenolic resin decomposition show that the reaction is complete by approximately 1000°C [106]. Paajanen and Vaari [107] studied cellulose decomposition at temperatures from 1400-2200 K using ReaxFF. However, experimental studies have shown initial cellulose pyrolysis occurring near 300°C. It should be noted that using elevated temperatures in some cases has produced inaccurate intermediate species during reactions but typically achieve the final expected products, assuming an appropriate forcefield parameterization. This work will use elevated temperatures as the method to accelerate reactions.

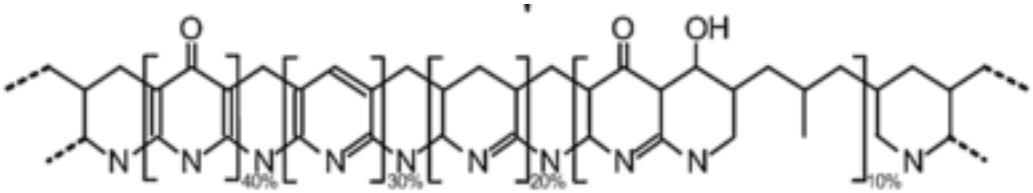

Figure 5.2: Concentrations of individual structures within stabilized PAN.

5.1 Structure Generation and Equilibration

Figure 5.2 shows the relative concentrations of different components of stabilized PAN (s-PAN). In this study, both the 40% and 30% concentration structures were used for carbonization simulations. For the oxygen content variation, s-PAN was varied with no oxygen, half of the individual rings containing oxygen, and all individual rings containing oxygen. The structures are seen in Figure 5.3. The stretch ratio and temperature variation simulations were performed with only the no-oxygen structure to simplify the model and to represent a significant percentage of the hypothesized s-PAN structure.

The s-PAN structures were each drawn and geometry optimized in Avogadro [30]. They were packed at a low density into a simulation volume with Packmol [31]. The packed structures were equilibrated with successive 50 ps simulations at 1 K, 100 K, and 300 K in the NPT ensemble. This resulted in final system density of approximately 1.55-1.6 g/cm^3.

Throughout this chapter simulations are run with Berendsen barostat and thermostat with 200 fs (1000 timesteps) and 20 fs (100 timesteps) damping constant, respectively. Berendsen has been shown to damp pressure and temperature oscillations during ReaxFF simulation better than Nose-Hoover due to its exponential velocity scaling, and is thus employed throughout. The timestep used was 0.2 fs because significant chemical product differences were not seen going to smaller timesteps. Charge equilibration was performed on each timestep with the method of Rappe and Goddard [108].

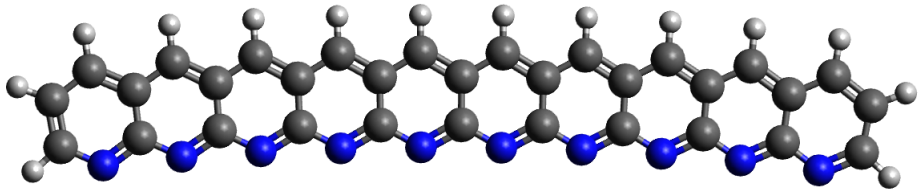

(a)

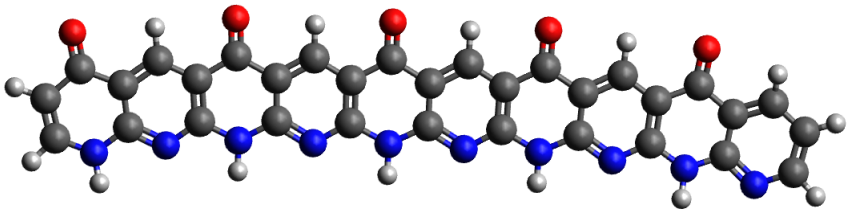

(b)

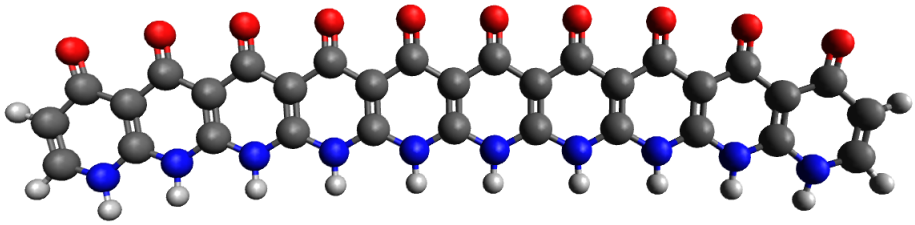

(c)

Figure 5.3: Stabilized PAN structures for (a) no oxygen content (no-O), (b) half oxygen content (half-O), and (c) all oxygen content (all-O).

The formulation of ReaxFF used was that of Liu, et al. [39]. This parameterization adds a low-gradient van der Waals correction factor which improves the description of long-range interactions for solids and leads to more accurate equilibrium densities for solids than the original parameterization. The parameter set builds upon the existing parameterization for hydrocarbon oxidation [89] and nitramine combustion reactions [109] making it particularly suited for studying s-PAN carbonization. The choice of parameter set was confirmed through correct bonding and number of molecules after equilibration to 300 K. At 300 K, 10 molecules of 10 C_5N rings were present. The s-PAN structures also had final system densities of 1.55 to 1.65 g/cm^3 which is in line with experimental studies that find s-PAN density of approximately 1.6 g/cm^3.

5.2 Determination of Reaction Parameters

Each individual equilibrated structure underwent a burn off simulation. For the burn off simulations equilibrated systems at 300 K were heated to 3000 K at 10 K/ps to determine the temperature at which significant reaction takes place. Trajectories were extracted from the burn off simulations at temperatures near the onset of degradation and used in annealing simulations.

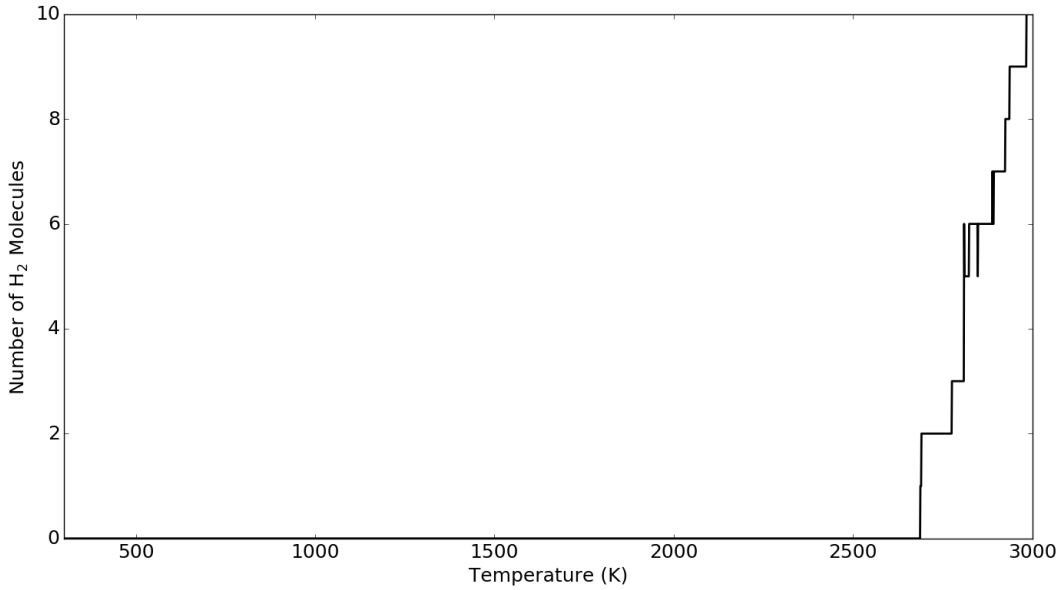

Figure 5.4: s-PAN heatup simulations showing H_2 elimination beginning at approximately 2800 K.

The s-PAN burn-off simulations showed stability until approximately 2800 K. H_2 gas elimination began occurring at approximately this temperature, see Figure 5.4. 2800 K is chosen as the annealing temperature for these reactions. To study the temperature effect on reaction mechanisms 2800 K, 3200 K, and 3600 K will be used.

5.3 Effect of Oxygen Concentration

The content of oxygen within a stabilized PAN structure can alter the reaction pathways and subsequent fiber structure during carbonization. For this section the oxygen

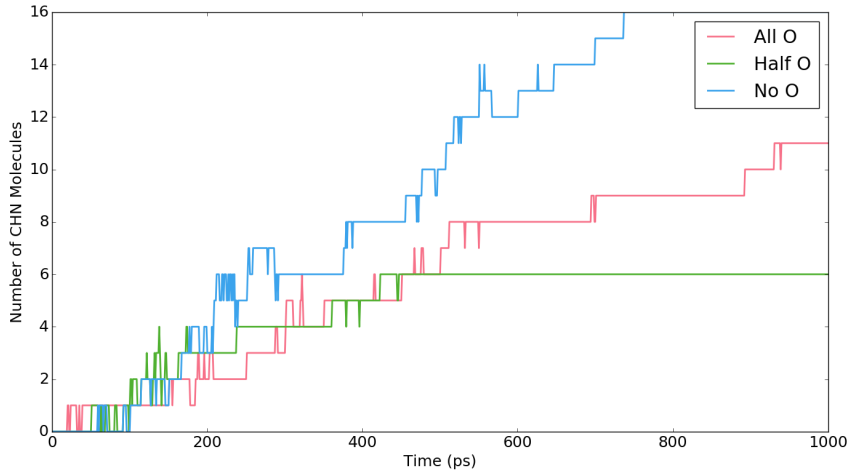

(a)

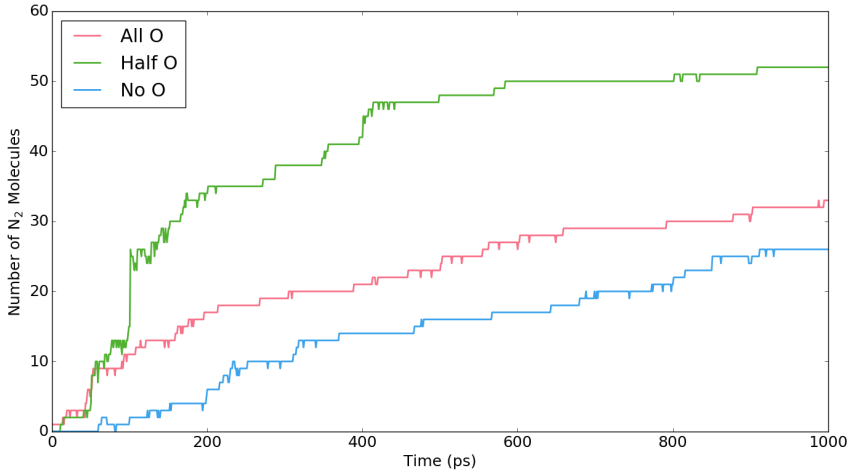

(b)

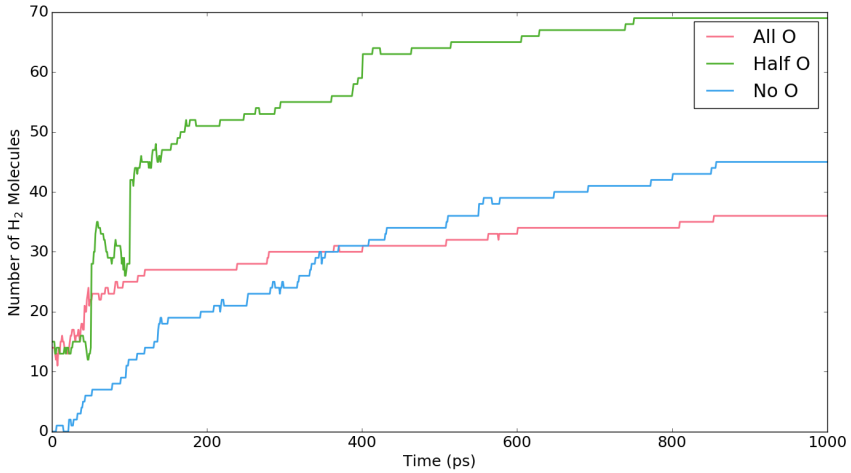

(c)

Figure 5.5: Species change during annealing simulations at 2800 K for (a) CHN, (b) N_2, and (c) H_2 gases.

content was varied in the fiber through using different molecule formulations as seen in Figure 5.3. In this section No-O refers to molecules with no double bonded oxygen, Half-O to molecules with half the rings having double bonded oxygen, and All-O to molecules with every ring having double bonded oxygen. Ten molecules were placed into the simulation volume with random orientation. The trajectories from heat ramp simulations were extracted at 2800 K and used for annealing simulations in the NVT ensemble for 1 ns. Removal of volatile gases, such as H_2O, N_2, H_2, NH_3, CO_2, CO, and HCN, was performed via a Python function call from within the LAMMPS script every 50 ps to emulate the carbonization process.

The formation of gaseous byproducts is one sign that s-PAN fiber is being reduced to high-carbon content fiber. Figure 5.5 shows the gaseous byproducts for each oxygen content type. H_2 and N_2 gases are produced most prevalently in the Half-O molecule, while the No-O and All-O molecules exhibit similar rates of production. HCN is produced most prevalently in the No-O structure.

Over-stabilization is a concern during the stabilization process. Over-stabilization results from high heating or too much time undergoing oxidation reaction which leads to a large proportion of C=O bonds in the structure. This was emulated using the All-O structure. During carbonization, most C=O bonds are eliminated and produce water vapor, as seen in Figure 5.20. The water vapor elimination produces a carbon radical that promotes crosslinking through either C-C or C-N bonds between s-PAN molecules. However, when there are too many C=O bonds, the likelihood of CO_2 and CO gas elimination increases. The removal of carbon from the structure reduces the aromatization and crosslinking potential, which has been shown to produce lower tensile strength in the final fiber [110].

Figure 5.6 shows the evolution of H_2O, CO_2, and CO gases during the simulation. Increasing the oxygen content results in larger numbers of all three gases and especially increases the production of CO_2 from the Half-O structure. The bond changes

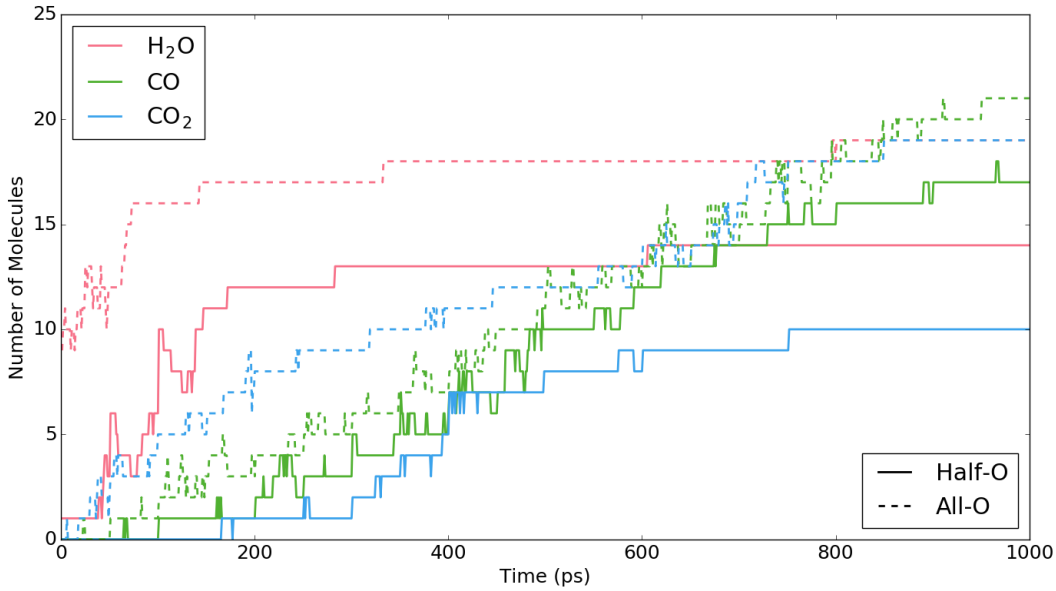

Figure 5.6: Evolution of H_2O, CO_2, and CO gases during carbonization of the half-O and all-O structures.

throughout the simulation show decreases in the C-C bonds of any order in both the No-O and All-O systems. Figure 5.7 shows the bond changes for both C-C and C-N bonds. The Half-O structure produces more C-C bonds and less C-N bonds than the all-O structure. Thus, Figures 5.5, 5.6, and 5.7 together show evidence that over-stabilization results in high CO and CO_2 production, which disrupts the N_2 and H_2 elimination mechanisms resulting in lower rates of gas elimination than the half-O molecule. In contrast, insufficient oxidation (No-O structure) has high HCN production which also disrupts the elimination mechanisms of H_2 and N_2. In both under and over oxidized cases the crosslinking would decrease from carbon being removed from the structure.

5.4 Effect of Molecular Orientation

Graphitic alignment along the fiber axis gives the final carbon fiber high modulus and strength properties. To create oriented graphite the PAN is often highly drawn before the stabilization phase to create chain alignment. The PAN chain alignment

would then produce aligned s-PAN molecules after stabilization. This section creates structures with different alignments of s-PAN molecules to study the effect of alignment on reaction pathways and final structure. An aligned structure was created using Packmol scripting to restrict molecule rotation along the x-axis. The average Herman's orientation parameter relating s-PAN orientation along its length to the x-axis after equilibration is used to distinguish between the different structures. The three created structures had average Herman's orientation values relative to the x-axis of 0.37, 0.86, 0.97. In this section structures will be referred to as H-37, H-86, or H-97 to correspond to their alignment.

As seen in Figure 5.8, all orientations had approximately the same number of both C_5 and C_6 rings, suggesting that alignment of chains does not significantly contribute to the concentration of graphitic structure within the fiber. High strength, high modulus fibers are produced when the graphitic planes are oriented along the fiber axis. To find the orientation of the graphite to the x-axis (fiber axis in the simulations) the angle between individual rings and the x-axis was found. Herman's Orientation was then used as the parameter describing alignment of graphite planes to the x-axis. Experimental research has found that beyond a critical draw ratio there is minimal improvement in mechanical properties or graphite crystal size and orientation relative to the fiber axis [111]. The researchers found decreasing orientation of graphite crystals with the fiber axis after carbonization. The result of Figure 5.9 suggests the carbonization reaction limits the final achievable graphite orientation. A Herman's orientation of -0.5 means the ring is perpendicular to the fiber axis, 1 is perfectly aligned, and 0 is completely random orientation. The H-37 structure starts out with rings slightly perpendicular to the fiber axis while the H-97 system has rings more aligned with the fiber axis. During the carbonization the H-97 system regresses toward a Herman's orientation of 0 while the H-37 also moves toward 0, suggesting carbonization disrupts the original molecular alignment and moves the resulting

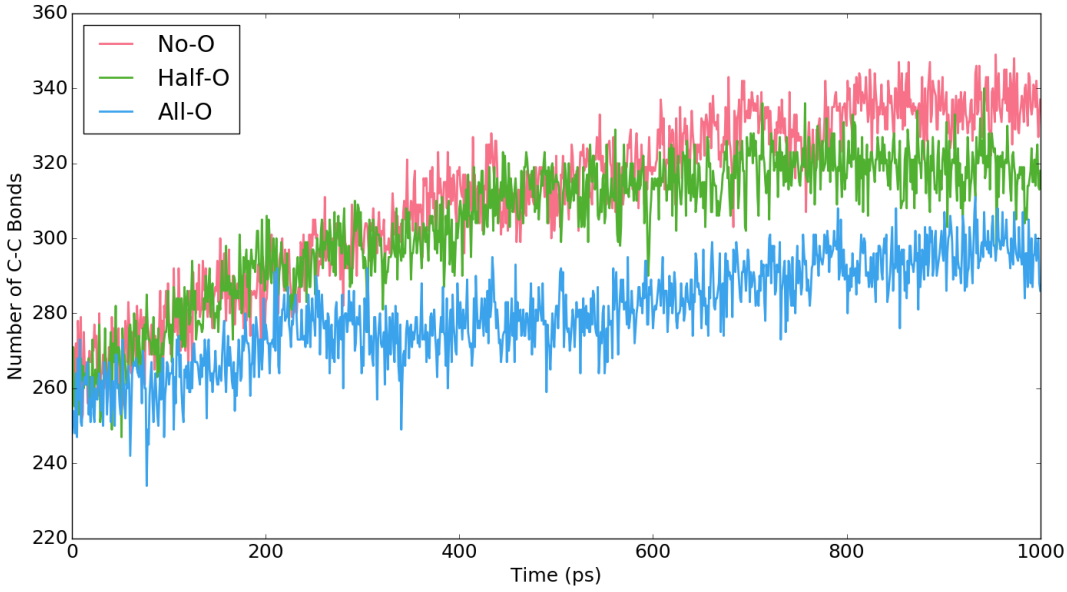

(a)

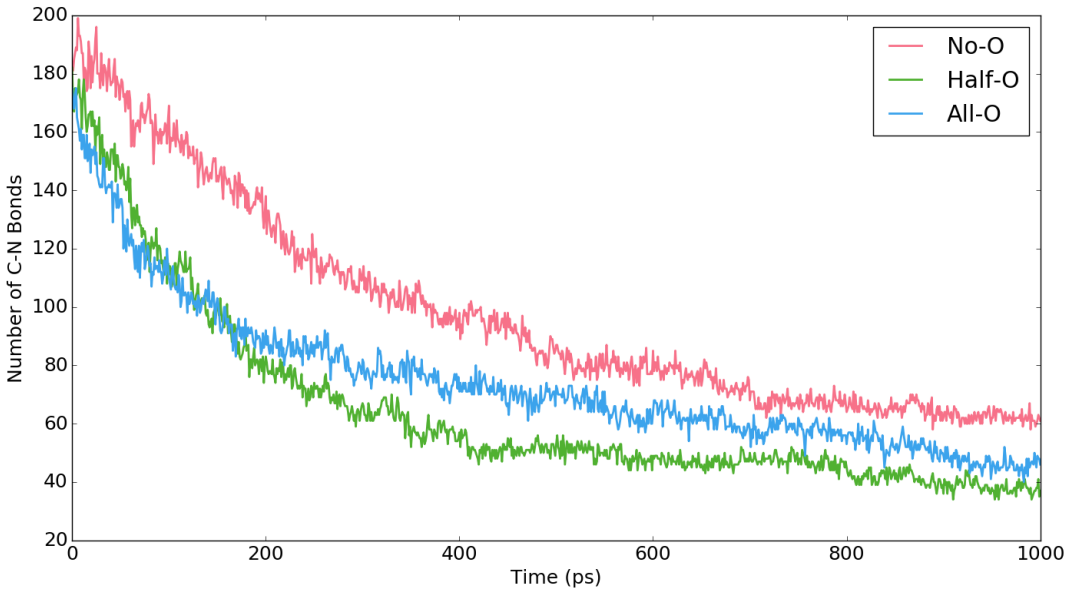

(b)

Figure 5.7: Changes in bonding for (a) C-C and (b) C-N bonds of all order throughout the simulation.

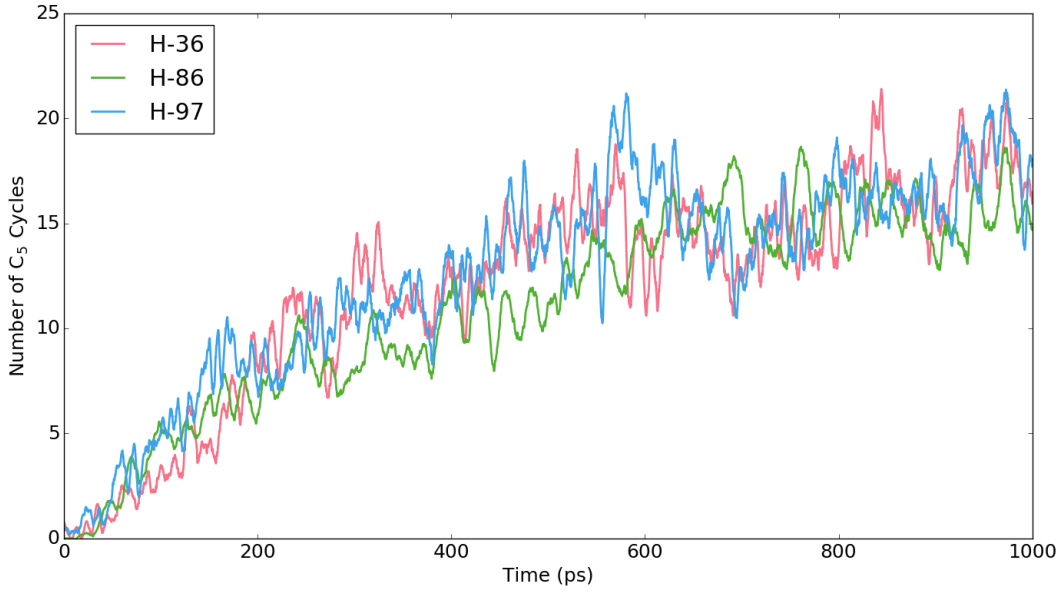

(a)

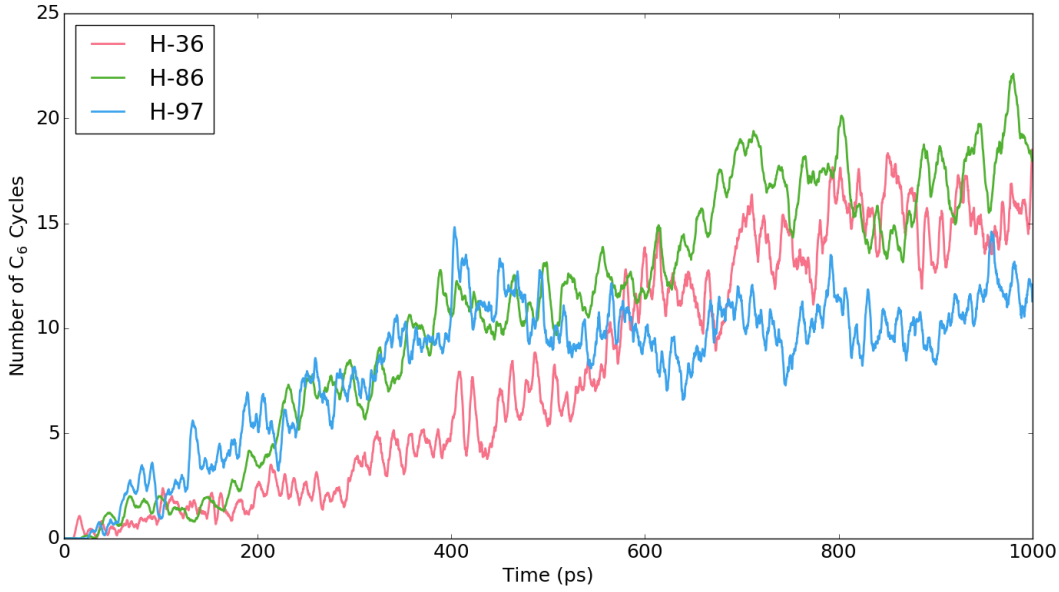

(b)

Figure 5.8: The number of (a) C_5 and (b) C_6 rings during carbonization of stabilized PAN fibers with different orientation.

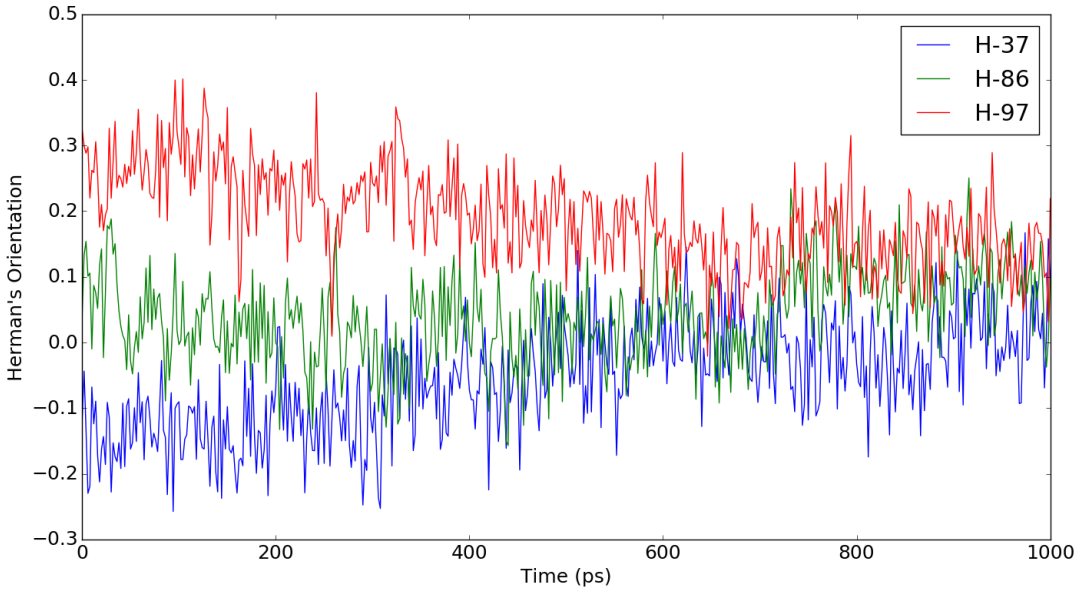

Figure 5.9: Average Herman's Orientation factor for all rings within the fiber throughout carbonization simulation.

graphitic structure toward random alignment. However, it should be noted that the simulation was run in NVT conditions with gas molecules being deleted resulting in a gradual decrease of density. In reality, carbonization helps to create higher density fiber. If density was maintained in the simulation through box compression after gas deletion the alignment of graphite planes may be altered.

5.5 Effect of Temperature

The H-97 structure was simulated at 2800 K, 3200 K, and 3600 K for 500 ps to investigate the role of temperature on gaseous byproduct formation and aromatization. Higher carbonization temperatures are known to lead to higher carbon content fibers. In fact, many fibers undergo a graphitization step after carbonization. Graphitization involves heating to 2000-3000°C to promote aromatization and is often used to produce high-modulus carbon fibers.

The rates of NH_3 and HCN gas elimination are nearly constant across all three temperatures and are shown in Figure 5.10. However, N_2 and H_2 gas elimination is

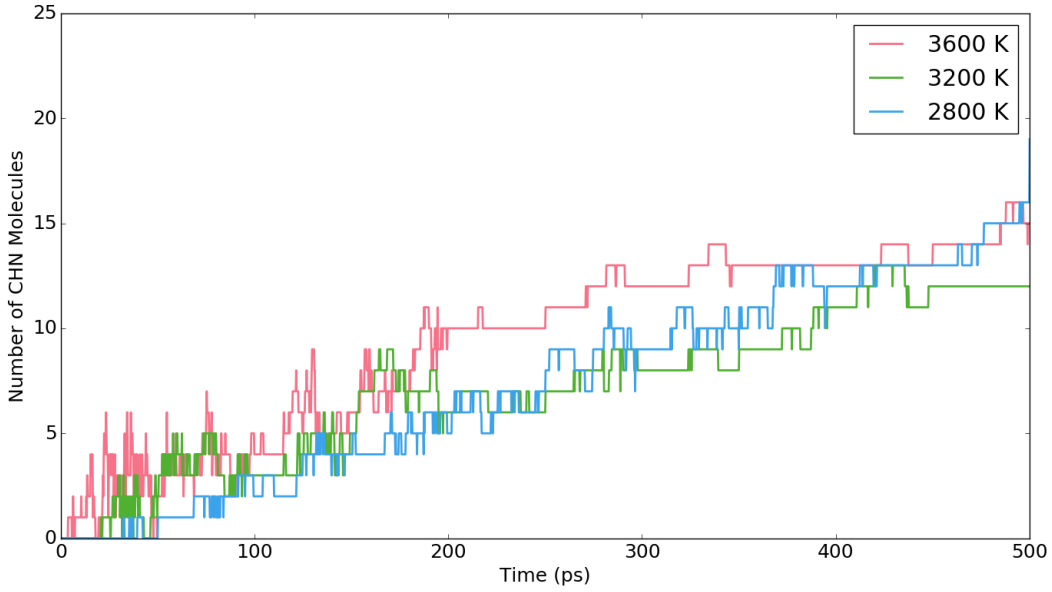

(a)

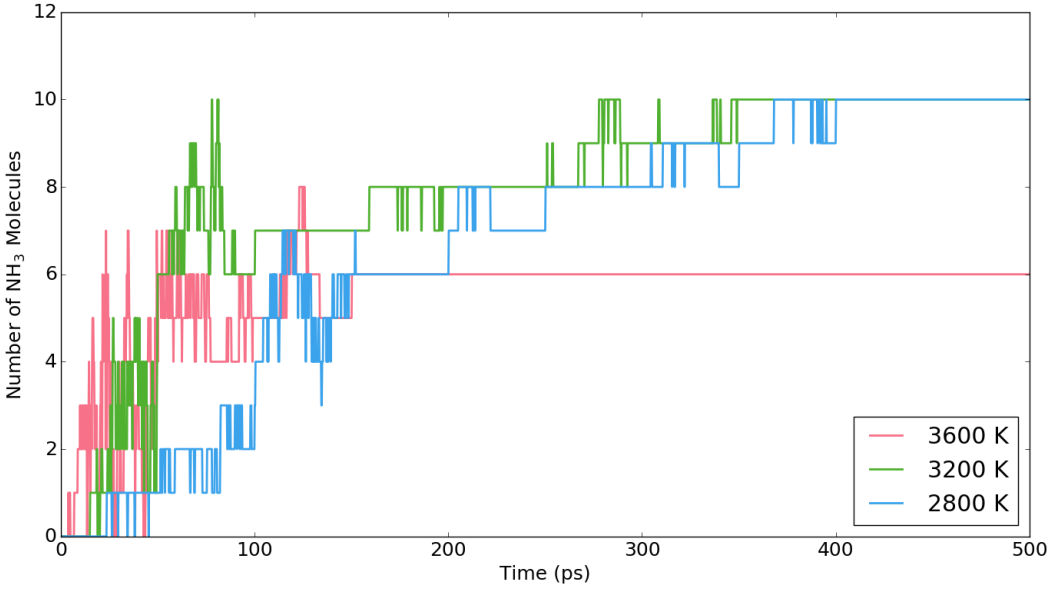

(b)

Figure 5.10: Gas elimination of (a) HCN and (b) NH_3 as a function of temperature.

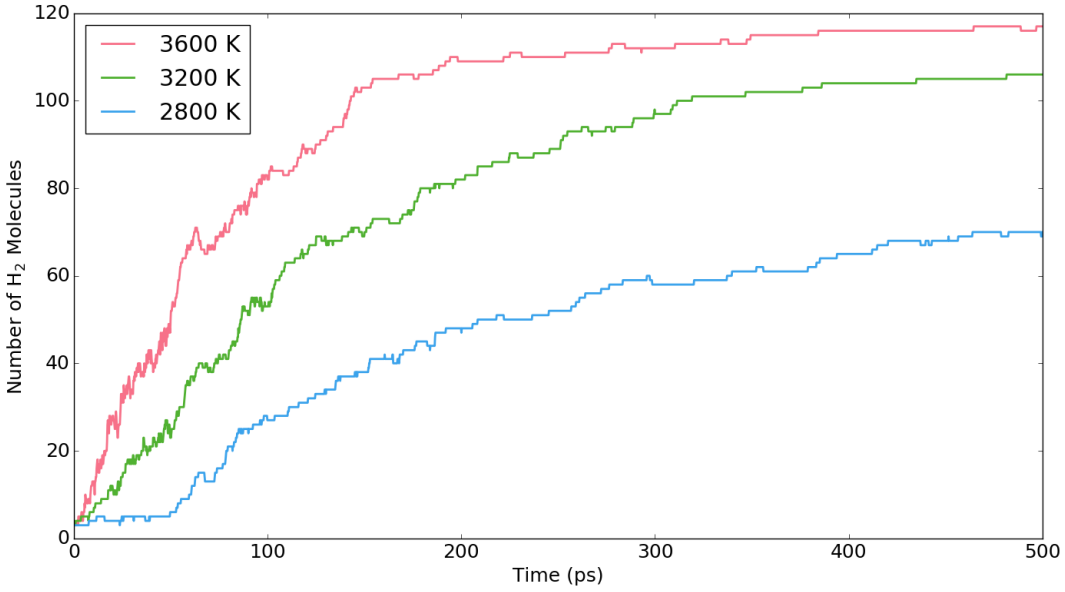

(a)

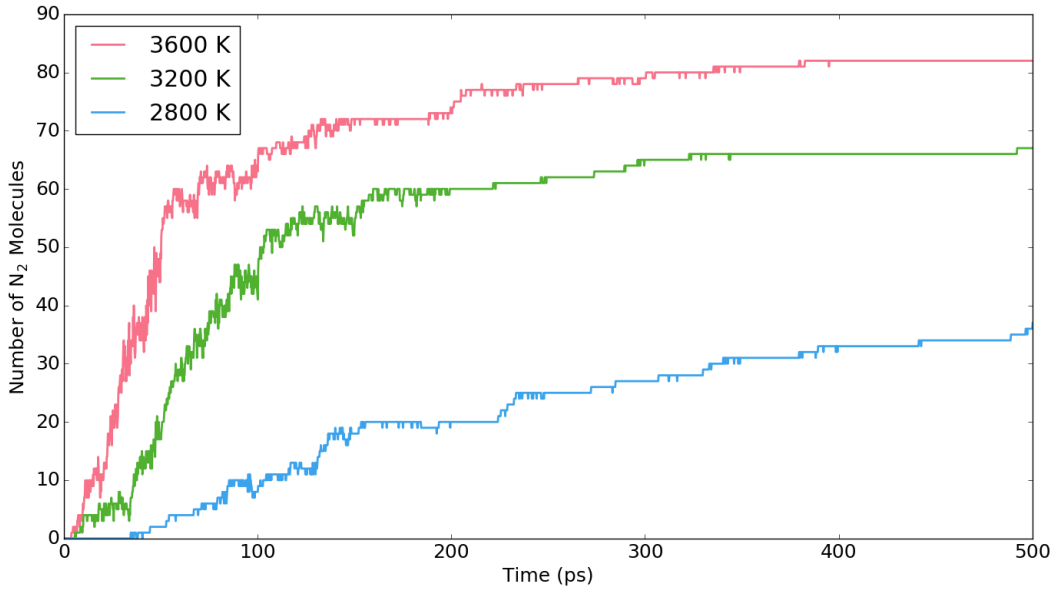

(b)

Figure 5.11: Gas elimination of (a) H_2 and (b) N_2 as a function of temperature.

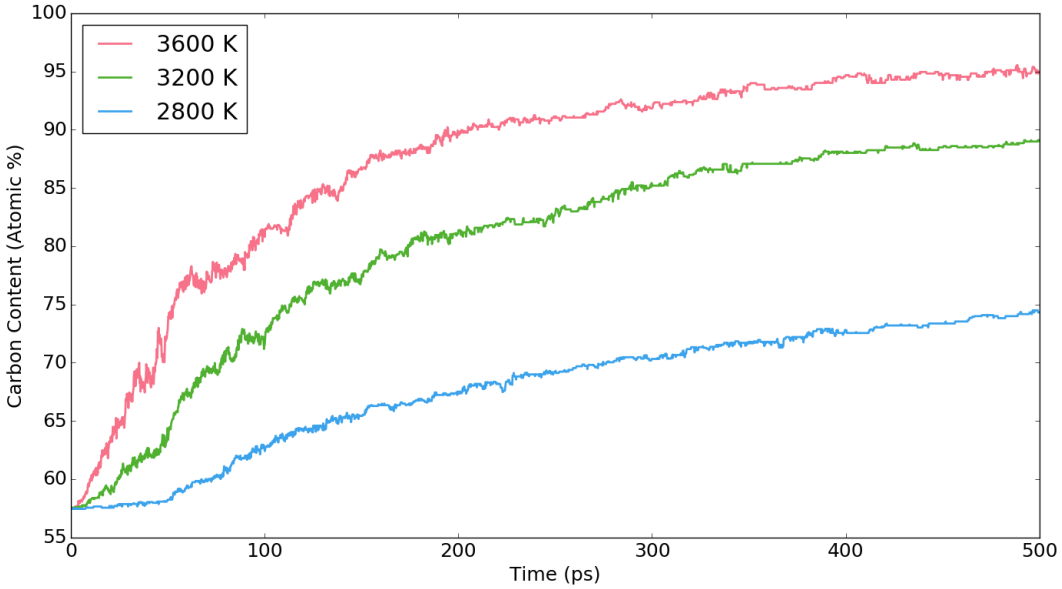

(a)

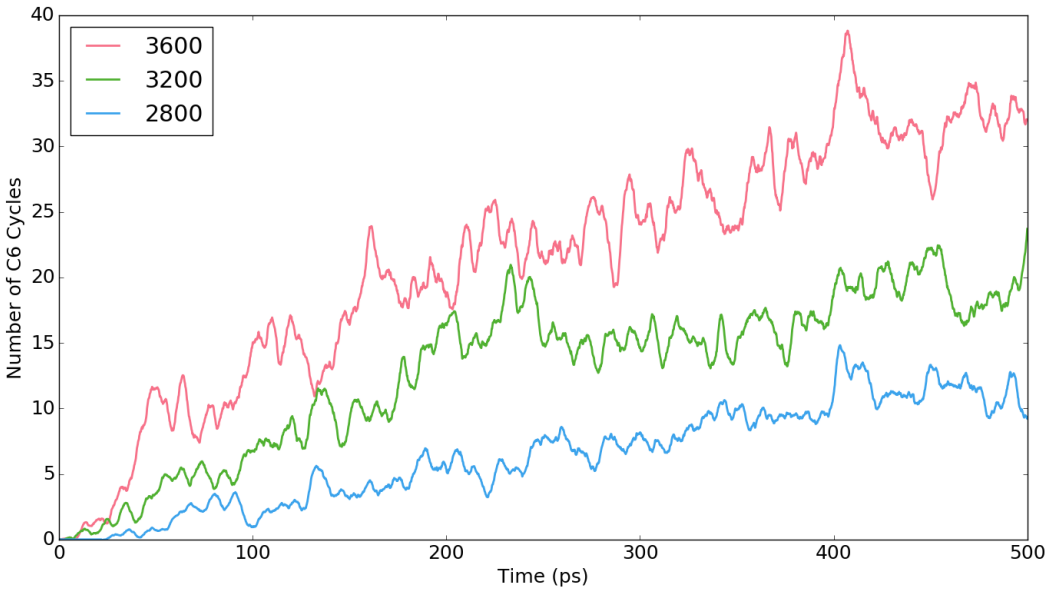

(b)

Figure 5.12: (a) Carbon content in the fiber during carbonization simulation at 2800, 3200, and 3600 K. (b) Evolution of C_6 rings during carbonization of s-PAN at 2800 K, 3200 K, and 3600 K.

Table 5.1: Gas Elimination Rate Constant (ns^{-1})

Gas Species	2800 K	3200 K	3600 K
H_2	1.38	3.96	6.84
N_2	0.809	3.62	7.14

dependent on temperature and follows a first-order reaction rate as seen in Figure 5.11. The reaction rates, k, are seen in Table 5.1.

Since major gas elimination follows a first-order reaction process it is also found that the conversion of the fiber to a high carbon content follows first-order kinetics as seen in Figure 5.12a. Further, the 3600 K simulation achieves carbon content of approximately 95%. The conversion to a high carbon content fiber also promotes aromatization in the fiber leading to high-modulus fibers. Aromatization can be seen in Figure 5.12b and a simulation snapshot showing graphitic structure is seen in Figure 5.13. C_5 ring evolution was nearly constant across all temperatures. The number of stable C_6 rings increased with temperature. Thus, shorter heating schedules at higher temperatures will promote higher carbon content and stable C_6 ring formation leading to more complete conversion of PAN to carbon fiber.

5.6 Gaseous Byproduct Elimination Mechanisms

This section details the reaction mechanisms leading to gaseous products during carbonization reactions. Reaction mechanisms are first determined using an in-house Python package. This code uses the ReaxFF bonding matrix and loops back in time from a single gas molecule to find all reactions that the atoms in the gas molecule undergo from the beginning of the simulation. The reactions are tracked using NetworkX graph theory package [112] to represent individual molecules as graphs at each timestep. A change in the bonding (graph edges) from one timestep to the next for a given atom in the final gas molecule represents a reaction. It then outputs a chemical reaction equation, timestep of reaction, and SMILES representation of the molecule

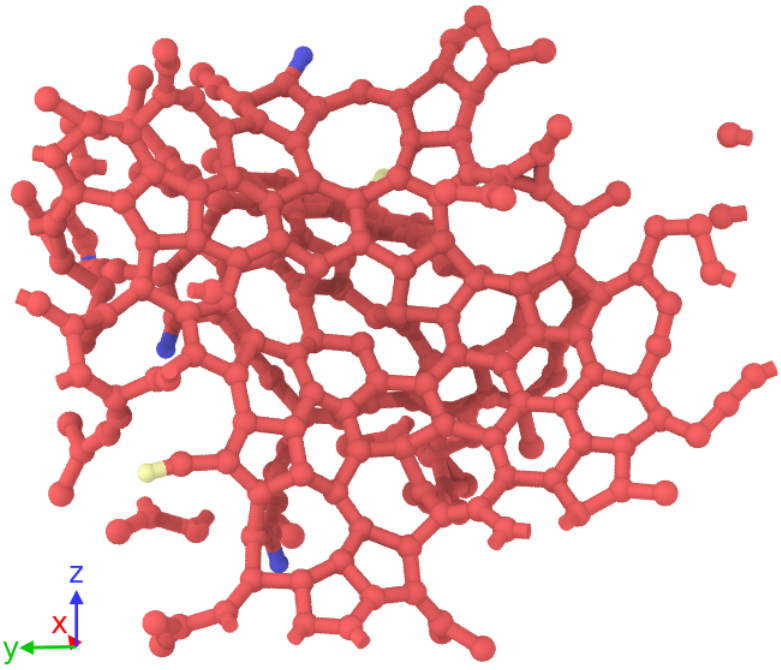

Figure 5.13: Snapshot from end of 3600 K carbonization simulation showing graphite structure. Only a portion of the total simulation atoms are shown for viewing clarity.

fragments involved in the reaction. OpenBabel [113] is used to convert NetworkX graphs to SMILES representations. These reactions are analyzed and the 3D depictions are generated in OVITO. For viewing clarity the 3D depictions show only those fragments of the overall system that participate in the reaction.

H_2 gases were produced at higher rates and at higher amounts than any other gas byproducts. Dehydrogenation is an important first step in the carbonization process. Production of H_2 increases the carbon content within the fiber and also promotes crosslinking between S-PAN molecules, which increases fiber density. Figures 5.14 and 5.15 show two examples of H_2 elimination mechanisms. Figure 5.14 step 1 shows H-abstraction to form an N-H bond. The N-H and C-H from two different pyridine rings combine to form H_2. Figure 5.15 step 1 to 2 shows the dominant H_2 elimination mechanism. In this mechanism H_2 forms by breaking two C-H bonds in the pyridine structure. This then leaves two carbon radicals on the s-PAN molecule that later

form crosslinks (step 3). Step 3 shows crosslinking that can either occur with C-N or C-C bonding.

N_2 reactions were found to be either intermolecular or intramolecular. Figure 5.16 shows intermolecular N_2 production. Steps 1 to 2 involve ring opening through CN bond breakage in the C_5N ring. Steps 2 to 3 show H-abstraction and N-N bond formation. Step 3 is the final step in which C-N bond breaking leads to N_2 gas formation and a C radical which can then form a bond to another nearby C radical. The intramolecular N_2 production involves opening of the C_5N rings adjacent to one another through C-N bond breakage seen in Figure 5.17. In step 3, the nitrogens bond to one another forming a C_5N_2 ring. Concurrent C-N bond breakage produces an N_2 molecule and two adjacent C radicals. The C radicals bond creating a C_5 ring. N_2 is the second most prevalent gas produced in the simulations. The production of N_2 gas leads to C radicals in the simulations. These C radicals can then either crosslink to other s-PAN chains or form intramolecular bonds which often creates the ring structures of graphitic carbon fiber.

HCN gas content was lower than that of H_2 and N_2 during the simulations. A likely explanation is the C=C bond breaking required for HCN; C=C bonds require more energy to break than C-N or C-H bonds required for H_2 and N_2 elimination. An example reaction mechanism is seen in Figure 5.18. Step 1 involves pyridine ring opening creating a carbon radical. Step 2 then shows H-abstraction to create a C-H bond. HCN is created by then breaking a C-C and C-N bond in the neighboring pyridine ring leaving a mostly carbon chain.

NH_3 reaction mechanism is shown in Figure 5.19. The first step involves pyridine ring opening and C-N crosslink bond formation. A C-N bond break in the crosslinked structure then produces an aniline on a pyridine ring. Two subsequent H-abstractions from nearby pyridine rings leads to the formation of NH_3. The production of NH_3 helps to drive up the carbon content of the fiber. H-abstraction to produce NH_3 also

creates carbon radicals and promotes crosslinking.

Water vapor eliminates hydrogens from the structure creating a high carbon content fiber. An example H_2O elimination mechanism is seen in Figure 5.20. A N-H bond is broken to produce an O-H bond. step 3 shows the reaction of the hydroxyl group with hydrogen on an adjacent s-PAN molecule that produces a water molecule and leaves a pyridine ring with no attached oxygen.

5.7 Conclusion

Carbon fiber production has been studied for decades, but only recently has the ReaxFF simulation methodology allowed for detailed reaction mechanism analysis during PAN carbonization. This chapter used ReaxFF to determine the effects of oxygen content, molecular orientation, and carbonization temperature on the resultant structure of carbon fiber from stabilized PAN precursor. Additionally, reaction mechanisms for gas byproduct elimination were proposed. The oxygen content did not significantly affect C_5 and C_6 graphitic ring formation. However, higher oxygen content did promote formation of CO and CO_2 gases which lower the final fiber carbon content. The carbonization process was found to shift the graphitic structures toward a random orientation with the fiber axis, regardless of the initial molecular orientation of s-PAN. Higher temperature was found to significantly improve the numbers of graphite rings in the final structure. This confirms experimental results and production methodologies which use high temperature graphitization after carbonization to produce high-modulus fibers with high carbon content and large crystallites. H_2 and N_2 gases were produced most prevalently during carbonization simulations. Detailed reaction mechanism analysis shows that H_2 and N_2 elimination produce carbon radicals that can then form crosslinks with other s-PAN molecules and eventually lead to ring formation and fiber densification.

Future work could include a study of fiber stabilization reactions. A ReaxFF

parameterization suitable toward low temperature oxidation may be needed to carry this out. Additionally, long simulation times or accelerated MD techniques could allow study of carbonization at realistic temperatures. Techniques such as bond-order based parallel replica dynamics [114] would allow for simulations on the order of hundreds of nanoseconds. A caveat with parallel replica dynamics is that the reaction processes must follow first order reaction kinetics. This chapter proved overall first order kinetics of PAN conversion to high carbon content fiber. Further, different precursors, such as Rayon, could be studied to elucidate the differences in structure or reaction mechanisms from different carbon fiber precursors.

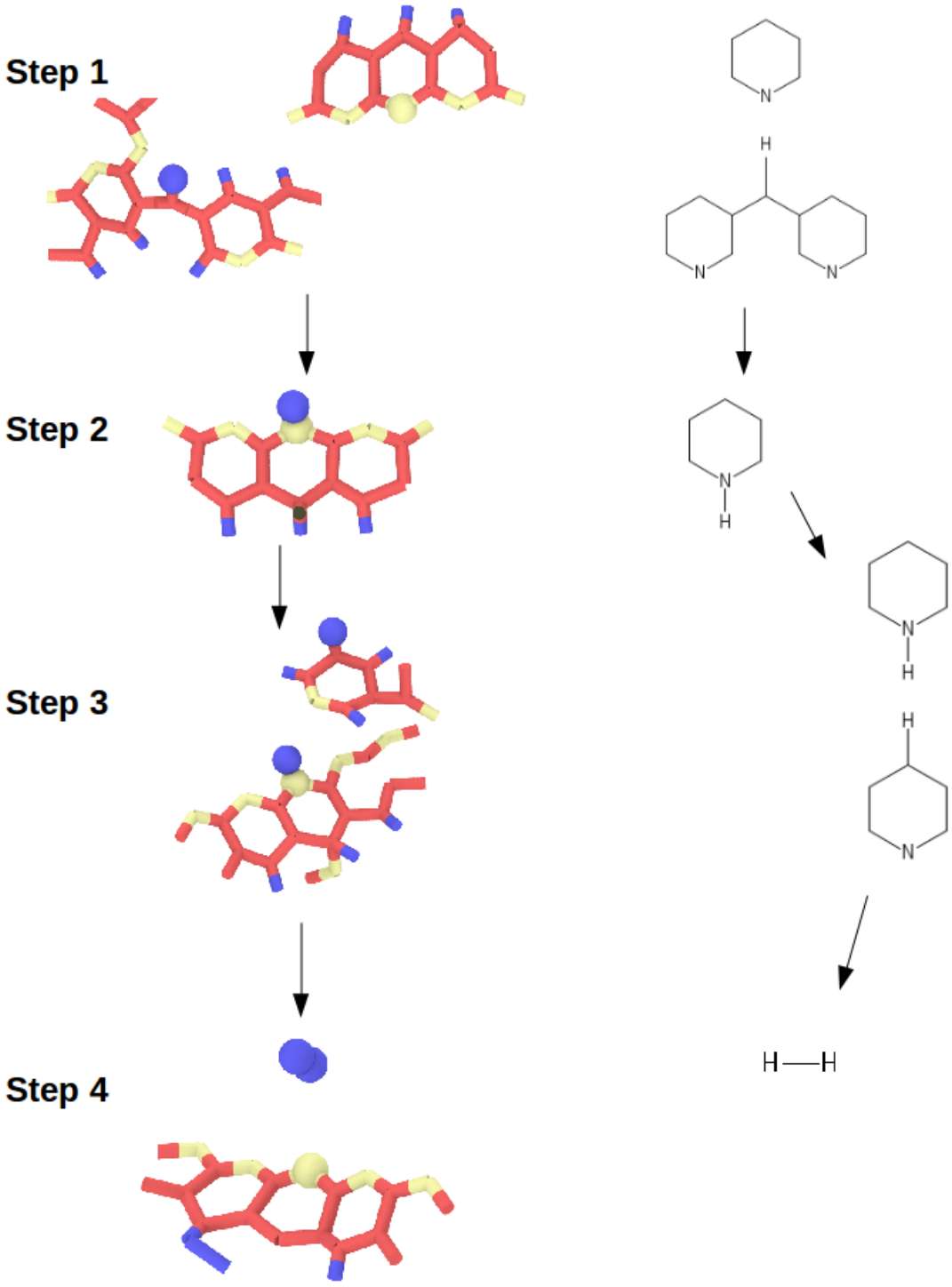

Figure 5.14: A representative reaction mechanism for H_2 elimination. Nitrogen is white, carbon is red, and hydrogen is blue.

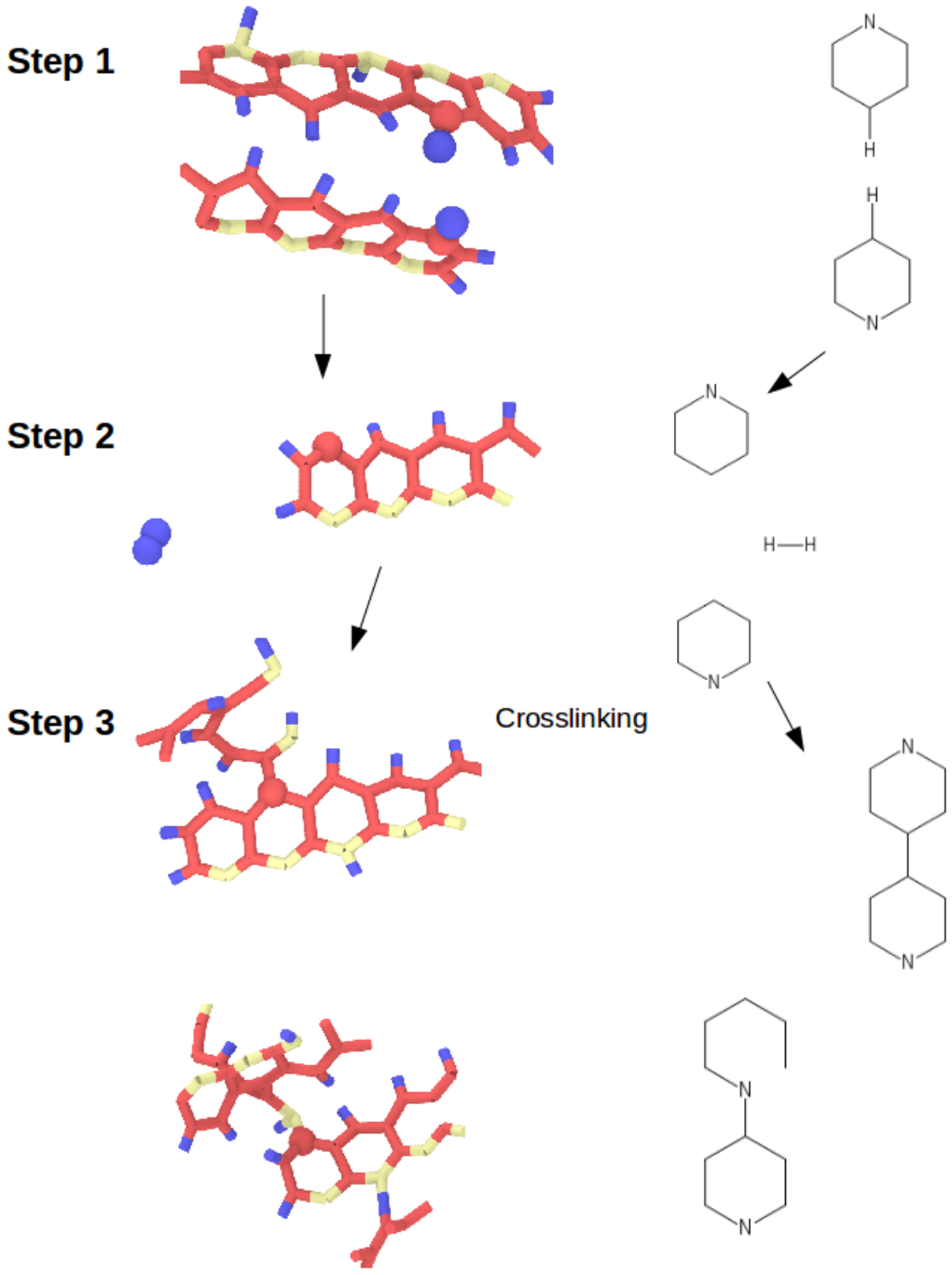

Figure 5.15: A representative reaction mechanism for H_2 elimination. Mechanism is taken one step further to show that carbon radicals produced from H_2 elimination are then able to crosslink to other s-PAN molecules via either C-N or C-C bonding. Nitrogen is white, carbon is red, and hydrogen is blue.

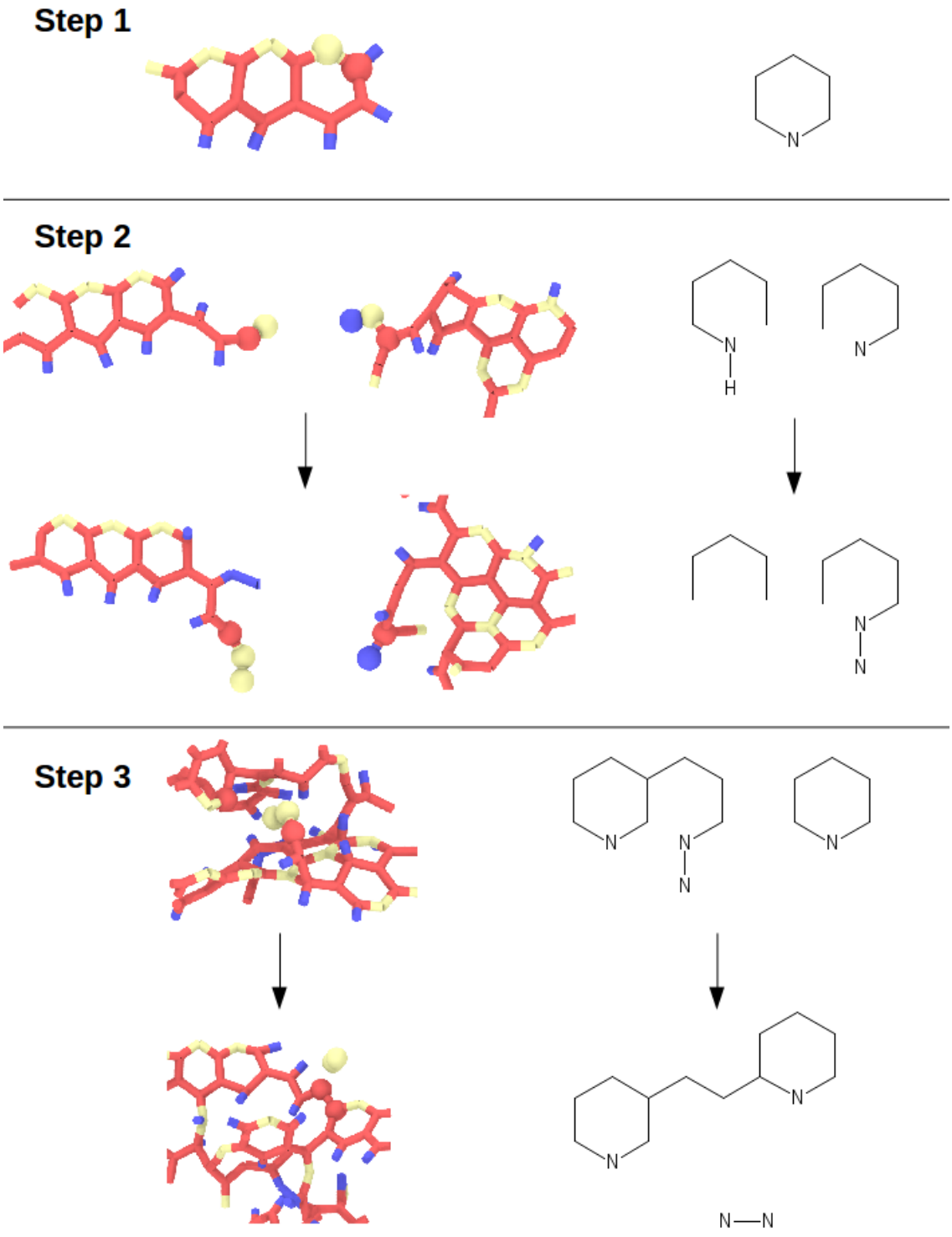

Figure 5.16: A representative reaction mechanism for N_2 elimination. Nitrogen is white, carbon is red, and hydrogen is blue.

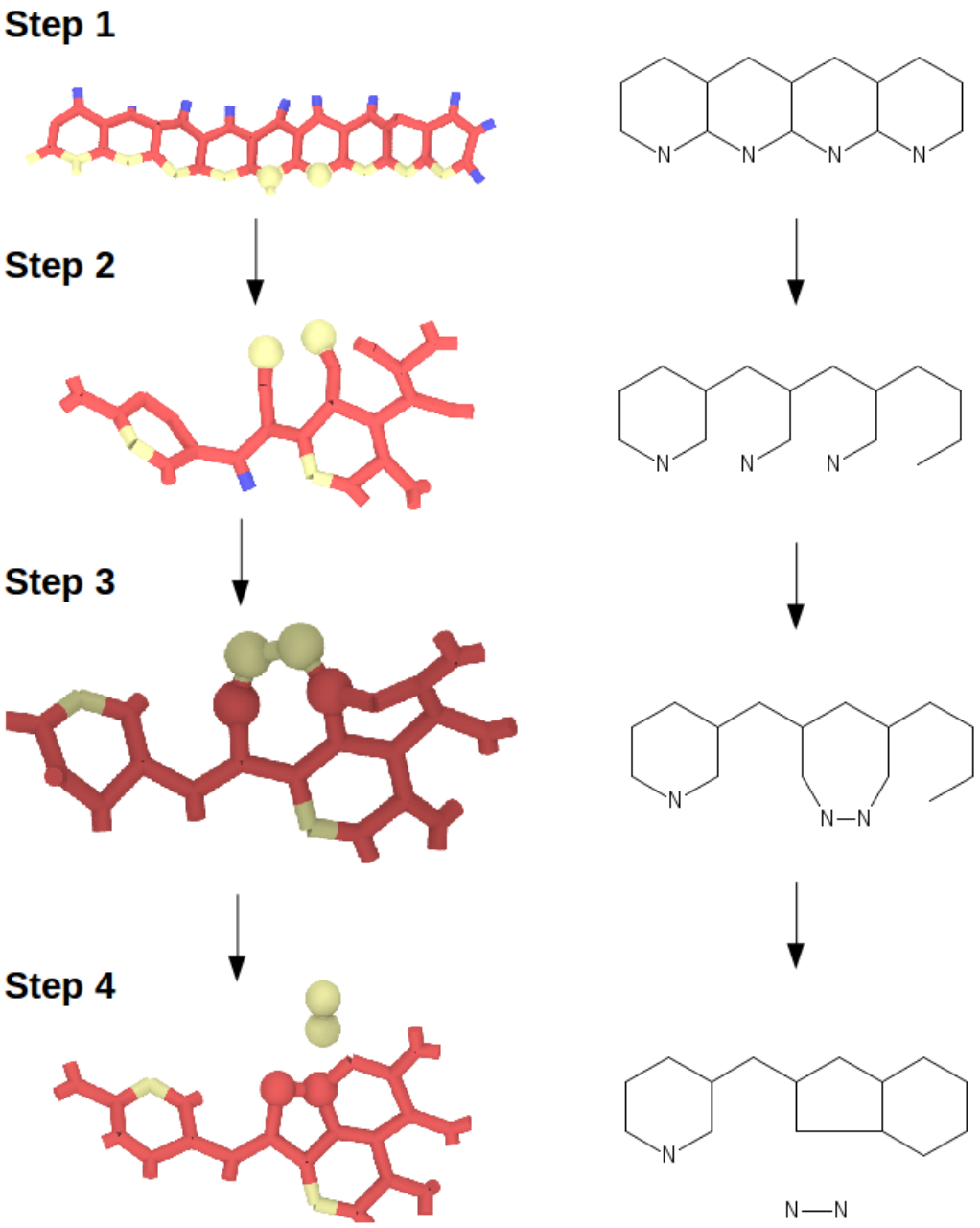

Figure 5.17: A representative reaction mechanism for N_2 elimination. Nitrogen is white, carbon is red, and hydrogen is blue.

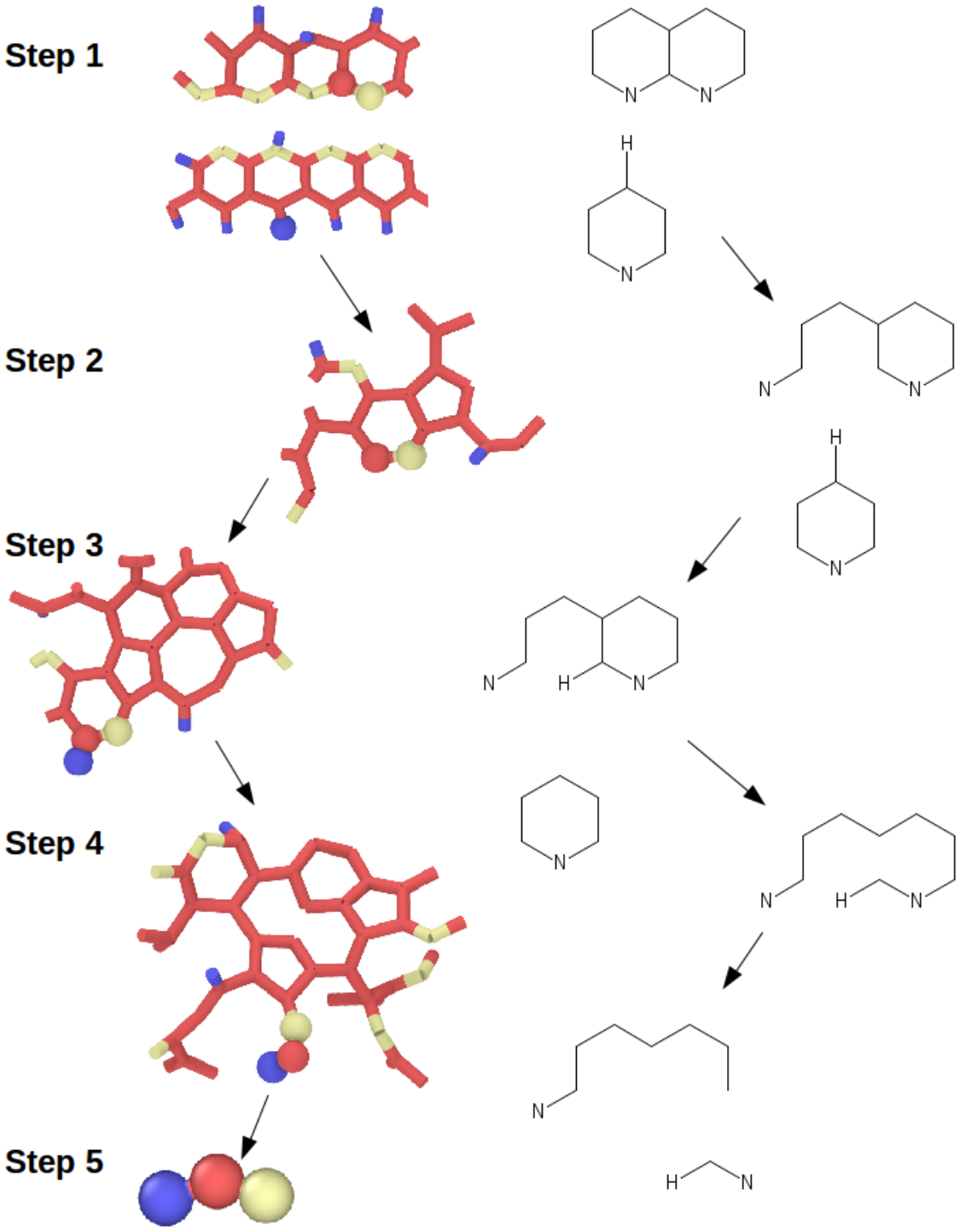

Figure 5.18: A representative reaction mechanism for HCN elimination. Nitrogen is white, carbon is red, and hydrogen is blue.

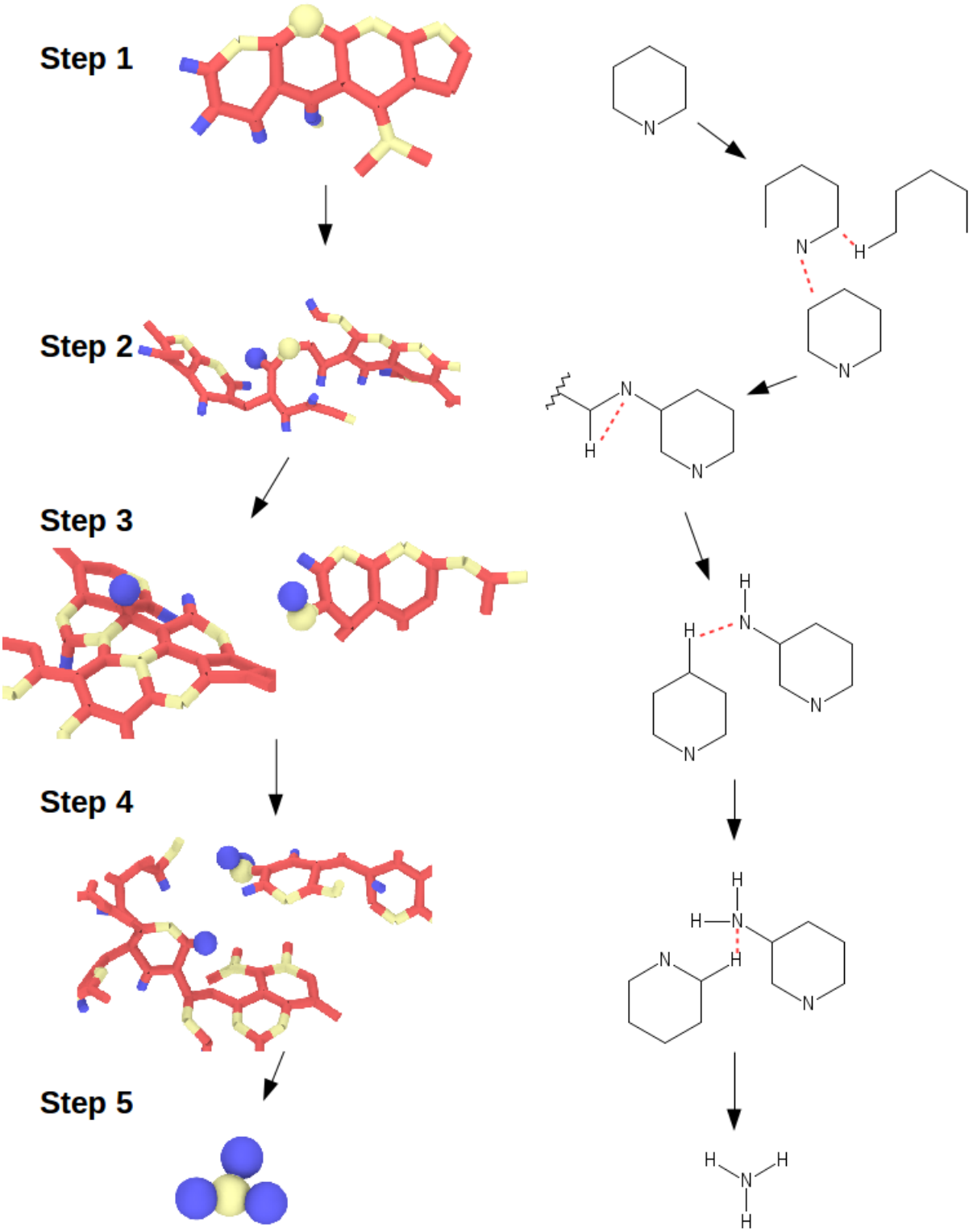

Figure 5.19: A representative reaction mechanism for NH_3 elimination. Nitrogen is white, carbon is red, and hydrogen is blue.

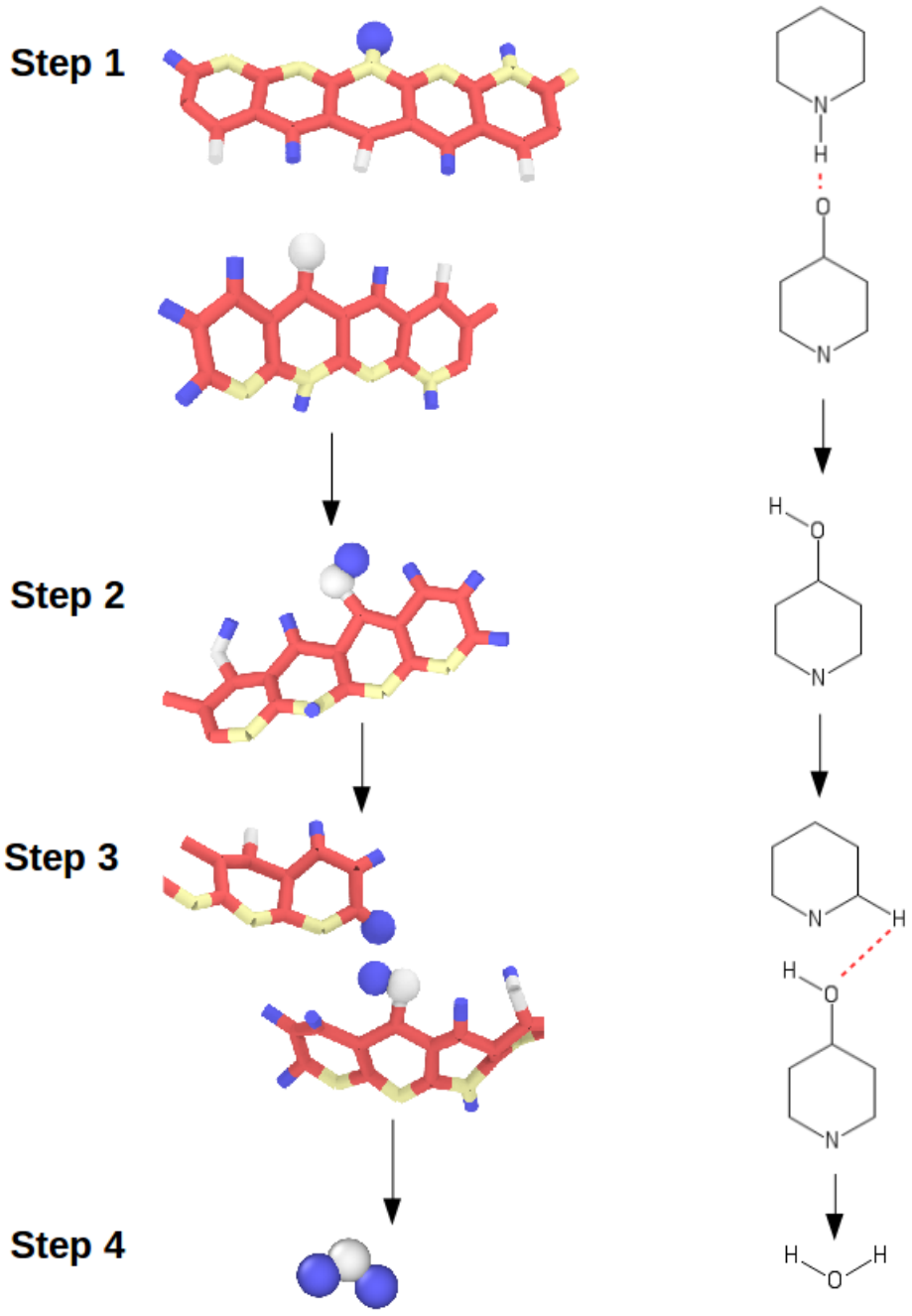

Figure 5.20: A representative reaction mechanism for H_2O elimination. Nitrogen is white, carbon is red, and hydrogen is blue.

CHAPTER VI

CONCLUSIONS AND FUTURE RECOMMENDATIONS

Overall this dissertation presented new methodologies for developing structure-property linkages in epoxies, fibers, and their composites through the use of molecular dynamics. Three different methods for modeling chemical reactions, including distance-based bond formation and energy-based bond dissociation in classical MD and ReaxFF modeling of bond changes in reactive MD, allowed structure-property linkages to be studied.

Robust characterization of the interphase change as a result of surface functionality was accomplished through application of spatial correlations and principal component analysis. The interphase structure of epoxy in an epoxy/graphene composite was determined to correlate to stress and temperature through an ordinary least squares regression with the interphase PCA structural descriptors. Furthermore, this methodology captured structural changes as a result of strain rate, functionality, and degree of crosslinking in bulk multifunctional epoxy structures. The number of surface attachment types, surface densities, and surface distributions present a difficult and arduous experimental problem to solve. Additionally, analytical techniques cannot accurately assess structure changes in the interphase at the atomic level. The models and methodology developed in this research could aid in developing prediction models for a host of surface functionalities. Future work in this area could include characterization of linear polymer response in the presence of nanofiller. ReaxFF simulations would also be better suited to assess structure changes in tensile strain as the forcefield will capture bond breakage. Experimental validation of the prediction accuracy would also be important to validate the molecular models. AFM could

be used to find interfacial strength in a pullout simulation and then compared to molecular simulations. Further refinement of the MKS methodology as applied to MD could also be performed. Due to the method of structure voxelization, a certain amount of data about the actual molecular topology is lost. A different structural description may be more appropriate, perhaps one that uses a distribution function to assign probabilities of atom locations within space as a function of distance away from the atom center. In this way the structure is not represented as binary 0 or 1 but as a probability between 0 and 1 that may better convey the polymer topology.

The network topology of covalent adaptable networks was studied under different external stimuli. Interaction with an ethylene glycol solvent modeled dissolution of CAN. The BER rate which can be controlled via catalyst concentration or temperature was found to significantly affect degradation rate. Because exchange reactions occur between dangling ends and crosslinked chains the rate of BER and molecular topology is affected by the degree of cure. The degree of cure and the stress on a system was found to correlate to fractional free volume. The distribution of individual surface area to volume ratio of voids was found to correlate with stress during relaxation simulations. Diffusivity of ethylene glycol was enhanced by bond exchange reaction but only above the gelation point. It is hypothesized that the benefit from bond exchange reactions within CANs is realized above the gelation point, while below the gelation point the higher chain mobility from low crosslink density negates the effects of bond exchange reactions. This research laid the foundation for studying many different CAN/solvent systems and thermomechanical properties of different CAN systems. Experimental work that varies catalyst concentration within CAN samples undergoing dissolution in EG would be able to confirm findings of increasing degradation with increasing BER rates. Future molecular dynamics simulation work could be performed to understand the role of different solvents on the CAN as a prediction tool. Additionally, a simulation methodology similar to the epoxy/graphene

work in this dissertation could be used to understand the effectiveness of CANs as a matrix material for nanocomposites. A more realistic simulation methodology could also be developed. As part of developing the methodology in this work, an analytics approach to bonding was developed and tested with some success. This approach used initial simulations of the CAN system, capturing the neighborhood (locations and velocities of atoms in the vicinity) surrounding a crosslink center when bonding occurred. After the equilibration stage, whether that local topology created a BER or not was recorded. From this data, a simple logistic regression model was trained on this data and subsequently used to predict whether a BER bond would result from the topology surrounding a crosslink center. Thus, the equilibration stage was eliminated and replaced with a predictive model. This idea showed promise but with limitations given molecular dynamics data was used to predict bonding outcomes. A suggestion would be to perform a density functional theory study of transesterification bonding in this system. From that local topology data, a more effective prediction of potential bonding could likely be developed. This would open up a potentially new method for MD simulation of bonding that would be more accurate than current distance based or MD/Monte Carlo methods that are used.

Production methods for carbon fiber have been studied for decades; however, experimental analytical techniques can only provide a certain level of insight into reaction mechanism that create the fiber structure. Reactive molecular dynamics simulations were performed to elucidate the reaction mechanism during carbonization of stabilized polyacrylonitrile with varying oxygen content, molecular orientation, and carbonization temperature. The oxygen content was not found to significantly affect the rate of graphitic ring formation; however, over-stabilization (high oxygen content) promoted formation of CO and CO_2 which reduces the carbon content of the fiber and reduces the crosslinking potential between individual stabilized PAN molecules. The molecular orientation of stabilized PAN was found to play little role

in the final graphitic alignment of graphite, suggesting the carbonization process moves the graphite planes toward a random orientation. Temperature played a significant role in the production of graphite structure. While C_5 structures showed no difference between the temperatures studies, the more stable C_6 rings were more prevalent with higher temperature carbonization. This confirms experimental results and current production methods which use a high temperature graphitization step after carbonization to promote aromatization and produce high-modulus fibers. Reaction mechanisms for the most common gaseous byproducts in carbonization were developed using a semi-automated reaction analysis code written in Python. Elimination of H_2 and N_2 were most prevalent in all simulations and also lead to carbon radicals that can form crosslinks to other s-PAN molecules. Crosslinking and high carbon content fiber then leads to ring formation and the graphitic structure of carbon fiber. The ReaxFF simulations in this work could be validated experimentally through partial carbonization studies of s-PAN fiber at different temperatures. Analyzing structure with x-ray scattering or FTIR could be compared directly to simulated XRD or FTIR plots. Chemical composition of the resultant fibers could allow determination of reaction rates and activation energies that could be compared with simulation. Future work in this area could include fiber stabilization reaction mechanisms. A different parameterization of ReaxFF may allow for study of low temperature oxidation. Additionally, studying the carbonization reaction mechanism with accelerated MD techniques such as bond-order based parallel replica dynamics would allow realistic temperatures and longer timescales (potentially hundreds of nanoseconds) to be achieved. One further area of research could use different precursors, such as Rayon or PAN copolymers, to understand the effect of precursor material on reaction mechanisms that produce final carbon fiber structure. Recent experimental work has begun looking at the benefit of introducing cellulose nanocrystals into a PAN matrix prior to creation of carbon fiber. Although attempted as part

of this work, the differences in decomposition temperatures between cellulose and PAN could not be reconciled in simulation. As mentioned previously, an accelerated timescale technique coupled with a different ReaxFF parameterization could allow simulation of a PAN/CNC composite at realistic decomposition temperatures. In this way reaction mechanisms and stability of this system could be studied.

APPENDIX A

SELECTION OF LAMMPS INPUT FILES

```
### 21 STEP EQUILIBRATION SCHEME ###

# GENERAL \\
   units real \\
   atom_style full \\
   dimension 3 \\
   newton on \\
   boundary p p p \\

# STYLES
   pair_style lj/cut/coul/cut 10.0
   pair_modify mix geometric
   #kspace_style pppm 1.0e-4
   bond_style harmonic
   angle_style harmonic
   dihedral_style opls
   special_bonds lj/coul 0.0 0.0 0.5

# VARIABLE
   variable t equal 300

# DEFINE SYSTEM
   read_data un-equilibrated.lmps

# SETTINGS
   dielectric 1.0
   neighbor 2.0 bin
   neigh_modify delay 0 every 5 check yes
   timestep 1.0
   run_style verlet

# OUTPUT
   dump 1 all custom 1560000 compress.lammpstrj id xu yu zu vx vy vz ix iy iz

# THERMO STYLE
   thermo_style custom step vol temp press etotal evdwl ecoul ebond eangle edihed eimp density
   thermo 10000

# INITIAL HIGH TEMPERATURE
   velocity all scale 600

# INITIAL MINIMIZATION
   min_style cg
   min_modify line quadratic
   minimize 1e-6 1e-6 10000 100000

#######
# 1
   fix 1 all nvt temp 600 600 100
```

```
   velocity all scale 600
   run 50000
   unfix 1

# 2
   fix 1 all nvt temp $t $t 100
   velocity all scale $t
   run 50000
   unfix 1

# 3 0.02*Pmax
   fix 1 all npt temp $t $t 100 iso 1000 1000 1000
   run 50000
   unfix 1

# 4
   fix 1 all nvt temp 600 600 100
   velocity all scale 600
   run 50000
   unfix 1

# 5
   fix 1 all nvt temp $t $t 100
   velocity all scale $t
   run 100000
   unfix 1

# 6 0.6*Pmax
   fix 1 all npt temp $t $t 100 iso 30000 30000 1000
   run 50000
   unfix 1

# 7
   fix 1 all nvt temp 600 600 100
   velocity all scale 600
   run 50000
   unfix 1

# 8
   fix 1 all nvt temp $t $t 100
   velocity all scale $t
   run 100000
   unfix 1

# 9 Pmax=50000
   fix 1 all npt temp $t $t 100 iso 50000 50000 1000
   run 50000
   unfix 1
```

```
# 10
   fix 1 all nvt temp 600 600 100
   velocity all scale 600
   run 50000
   unfix 1

# 11
   fix 1 all nvt temp $t $t 100
   velocity all scale $t
   run 100000
   unfix 1

# 12 0.5*Pmax
   fix 1 all npt temp $t $t 100 iso 25000 25000 1000
   run 5000
   unfix 1

# 13
   fix 1 all nvt temp 600 600 100
   velocity all scale 600
   run 5000
   unfix 1

# 14
   fix 1 all nvt temp $t $t 100
   velocity all scale $t
   run 10000
   unfix 1

# 15 0.1*Pmax
   fix 1 all npt temp $t $t 100 iso 5000 5000 1000
   run 5000
   unfix 1

# 16
   fix 1 all nvt temp 600 600 100
   velocity all scale 600
   run 5000
   unfix 1

# 17
   fix 1 all nvt temp $t $t 100
   velocity all scale $t
   run 10000
   unfix 1

# 18 0.01*Pmax
   fix 1 all npt temp $t $t 100 iso 500 500 1000
   run 5000
```

```
   unfix 1

# 19
   fix 1 all nvt temp 600 600 100
   velocity all scale 600
   run 5000
   unfix 1

# 20
   fix 1 all nvt temp $t $t 100
   velocity all scale $t
   run 10000
   unfix 1

# 21 Pfinal=1 bar
   fix 1 all npt temp $t $t 100 iso 1 1 1000
   run 800000
   unfix 1

write_data equilibrated.lmps
```

```
### DYNAMIC TENSILE STRAIN ###

# GENERAL

units           real
atom_style      full
dimension       3
newton          on
boundary        p p p

# STYLE

pair_style      lj/cut/coul/cut 10.0
pair_modify     mix geometric
special_bonds   lj/coul 0 0 0.5
bond_style      harmonic
angle_style     harmonic
dihedral_style  opls

# SETTINGS

dielectric      1.0
neighbor        2.0 bin
neigh_modify    delay 0 every 1 check yes
timestep        1.0

# READ IN LAMMPS FILE

read_data tri_x1230c.lmps

# THERMO DATA

run_style verlet
thermo_style custom step vol temp press etotal pe ke density
thermo 10000
log log.tri_x1230c

# GROUP MOLECULES

group epoxy molecule <= 1800
group graphene molecule > 1800

# VARIABLES

variable    lx equal lx
variable    ly equal ly
variable    lz equal lz
variable    lx0 equal ${lx}
variable    ly0 equal ${ly}
```

```
variable    lz0 equal ${lz}
# STRAIN CALCULATION
variable    esxx equal (v_lx-v_lx0)/v_lx0
variable    esyy equal (v_ly-v_ly0)/v_ly0
variable    eszz equal (v_lz-v_lz0)/v_lz0
# STRESS CALCULATION
compute     stress all stress/atom NULL
compute     totsig all reduce sum c_stress[1] c_stress[2] c_stress[3] c_stress[4] c_stress[5] c_stress[6]
# PER ATOM STRESS
variable    spaxx atom c_stress[1]/vol*0.101325
variable    spayy atom c_stress[2]/vol*0.101325
variable    spazz atom c_stress[3]/vol*0.101325
# TOTAL STRESS
variable    totsxx equal c_totsig[1]/vol*0.101325
variable    totsyy equal c_totsig[2]/vol*0.101325
variable    totszz equal c_totsig[3]/vol*0.101325

variable totpe equal pe
variable dens equal density

# OTHER COMPUTES

compute rho epoxy chunk/atom bin/1d z lower 0.5 units box
compute rhoall all chunk/atom bin/1d z lower 0.5 units box
compute pot all pe/atom
compute epot epoxy pe/atom
compute voro all voronoi/atom

# MAIN RUN DYNAMICS
fix dens epoxy ave/chunk 5 2 4000 rho density/mass file density.txt
fix pnrg all ave/chunk 5 2 4000 rhoall c_pot file all_pe.txt
fix epnrg epoxy ave/chunk 5 2 4000 rho c_epot file epoxy_pe.txt

fix 1 all npt temp 300 300 100 y 0 0 1000 z 0 0 1000
fix 2 all deform 1 x scale 1.2 remap x  # deform to 20% strain
fix 3 all ave/time 2 50 500 v_esxx v_esyy v_eszz v_totsxx v_totsyy v_totszz v_totpe v_dens file
stress_strain.txt
# Simulation snapshot
dump 1 all custom 4000 tri_x1230c_xstraine8.lammpstrj id mol type q x y z ix iy iz c_pot c_stress[1]
# Snapshot with per-atom stress and Voronoi Cell data
dump 2 all custom 100000 10layer-voro.lammpstrj id mol type q x y z c_stress[1] c_stress[2]
c_stress[3] c_stress[4] c_stress[5] c_stress[6] voro[1] voro[2]
run 400000

write_data tri_x1230c_strained.lmps
```

```
### REAXFF SIMULATION FOR PAN CARBONIZATION ###

units           real
boundary        p p p

atom_style      full
read_data       pan_stable.lmps
log log.pan_stable

pair_style      reax/c control.reax_lg_stabilized lgvdw yes safezone 3.0 mincap 200
pair_coeff      * * ffield.reax.lg C H N O

neighbor        2 bin
neigh_modify every 1 delay 0 check yes

# THERMODYNAMIC DATA
thermo_style custom step vol temp press etotal pe ke density
thermo_modify lost warn
thermo 1000

run_style verlet
timestep 0.2

# VARIABLES AND COMPUTES
variable bondfile string pan_stable.bonds
variable foo python deletion
variable dens equal density
compute pe all pe/atom
compute xray all xrd 1.541838 C H N O 2Theta 1 50 echo
compute ep all pe/atom pair

# READ IN DUMPFILE SNAPSHOT FROM BURNOFF SIMULATION
read_dump dump.pan_stable_heatup.lammpstrj 1250000 x y z q vx vy vz ix iy iz box yes replace yes

reset_timestep 0

# CHARGE EQUILIBRATION
fix     chg all qeq/reax 1 0.0 10.0 1e-4 reax/c

# DYNAMICS LOOP WITH GAS DELETION EVERY 50 PS

variable ii loop 20

# ANNEAL
fix     2 all reax/c/bonds 5000 pan_stable.bonds
fix     3 all reax/c/species 1 1 5000 pan_stable.species element C H N O cutoff 1 2 0.25 cutoff 1 4 0.25
dump    1 all custom 5000 dump.pan_stable.lammpstrj id mol type q x y z ix iy iz vx vy vz c_pe
python deletion input 1 v_bondfile format s file delete_atoms.py
```

```
label begin

fix     1 all nve
fix     2 all temp/berendsen 2800 2800 20
fix     mom all momentum 1 linear 1 1 1
run     250000
unfix   1
unfix   2
unfix   mom

# CHECK FOR GAS MOLECULE ELIMINATION AND DELETE IF NECESSARY
python deletion invoke
include delete_atoms_include.in
shell rm delete_atoms_include.in

write_data pan_stable_anneal_loop.lmps

next ii
jump SELF begin
```

REFERENCES

[1] S. Goodman, "Epoxy Resins," in *Handb. Thermoset Plast.*, ch. 6, pp. 193–268, 1988.

[2] D. Adolf, J. E. Martin, and J. P. Wilcoxon, "Evolution of Structure and Viscoelasticity in an Epoxy Near the Sol-Gel Transition," *Macromolecules*, vol. 23, no. 2, pp. 527–531, 1990.

[3] B. Arash, Q. Wang, and V. K. Varadan, "Mechanical properties of carbon nanotube/polymer composites.," *Sci. Rep.*, vol. 4, p. 6479, jan 2014.

[4] M. Fang, Z. Zhang, J. Li, H. Zhang, H. Lu, and Y. Yang, "Constructing hierarchically structured interphases for strong and tough epoxy nanocomposites by amine-rich graphene surfaces," *J. Mater. Chem.*, vol. 20, no. 43, p. 9635, 2010.

[5] V. Georgakilas, M. Otyepka, A. B. Bourlinos, V. Chandra, N. Kim, K. C. Kemp, P. Hobza, R. Zboril, and K. S. Kim, "Functionalization of graphene: covalent and non-covalent approaches, derivatives and applications.," *Chem. Rev.*, vol. 112, pp. 6156–214, nov 2012.

[6] R. J. Moon, A. Martini, J. Nairn, J. Simonsen, and J. Youngblood, "Cellulose nanomaterials review: structure, properties and nanocomposites.," *Chem. Soc. Rev.*, vol. 40, pp. 3941–94, jul 2011.

[7] H.-m. Ng, L. Tin, T.-t. Tee, S.-t. Bee, D. Hui, C.-y. Low, and A. R. Rahmat, "Extraction of cellulose nanocrystals from plant sources for application as reinforcing agent in polymers," *Compos. Part B*, vol. 75, pp. 176–200, 2015.

[8] Y. Habibi, L. Lucia, and O. J. Rojas, "Cellulose nanocrystals: chemistry, self-assembly, and applications.," *Chem. Rev.*, vol. 110, pp. 3479–500, jun 2010.

[9] H. Abdul Khalil, A. Bhat, and A. Ireana Yusra, "Green composites from sustainable cellulose nanofibrils: A review," *Carbohydr. Polym.*, vol. 87, pp. 963–979, jan 2012.

[10] M. R. Kamal and V. Khoshkava, "Effect of cellulose nanocrystals (CNC) on rheological and mechanical properties and crystallization behavior of PLA / CNC nanocomposites," *Carbohydr. Polym.*, vol. 123, pp. 105–114, 2015.

[11] M. M. Tang and R. Bacon, "Carbonization of Cellulose Fibers-I: Low temperature pyrolysis," *Carbon N. Y.*, vol. 2, pp. 211–220, 1964.

[12] L. Törk, G. Jiménez-Osés, C. Doubleday, F. Liu, and K. N. Houk, "Molecular Dynamics of the Diels-Alder Reactions of Tetrazines with Alkenes and N2 Extrusions from Adducts," *J. Am. Chem. Soc.*, vol. 137, no. 14, pp. 4749–4758, 2015.

[13] M. Allen, "Introduction to molecular dynamics simulation," in *Comput. Soft Matter From Synth. Polym. to ...*, vol. 23, pp. 1–28, 2004.

[14] Q. Zeng, a.B. Yu, and G. Lu, "Multiscale modeling and simulation of polymer nanocomposites," *Prog. Polym. Sci.*, vol. 33, pp. 191–269, feb 2008.

[15] F. Escobedo and J. de Pablo, "Monte Carlo simulation of branched and crosslinked polymers," *J. Chem. Phys.*, vol. 104, no. 12, pp. 4788–4801, 1996.

[16] J. E. Shepherd, *Multiscale Modeling of the Deformation of Semi-Crystalline Polymers*. PhD thesis, 2006.

[17] W. L. Jorgensen, "Optimized Intermolecular Potential Functions for Liquid Alcohols," *J. Phys. Chem.*, vol. 90, pp. 1276–1284, 1986.

[18] W. Mayo, S. Olafson, B. Goddard III, "Deriding a generic force field for molecular simulation," *J. Phys. Chem.*, vol. 94, pp. 8897–8909, 1990.

[19] B. R. Brooks, R. E. Bruccoleri, B. D. Olafson, D. J. States, S. Swaminathan, and M. Karplus, "CHARMM: A program for macromolecular energy, minimization, and dynamics calculations," *J. Comput. Chem.*, vol. 4, no. 2, pp. 187–217, 1983.

[20] W. L. Jorgensen, D. S. Maxwell, and J. Tirado-rives, "Development and Testing of the OPLS All-Atom Force Field on Conformational Energetics and Properties of Organic Liquids," *J. Am. Chem. Soc.*, vol. 7863, no. 15, pp. 11225–11236, 1996.

[21] M. J. Hwang, T. P. Stockfisch, and a. T. Hagler, "Derivation of Class-II Force-Fields .2. Derivation and Characterization of a Class-II Force-Field, CFF93, for the Alkyl Functional-Group and Alkane Molecules," *J. Am. Chem. Soc.*, vol. 116, no. 6, pp. 2515–2525, 1994.

[22] H. Sun, "COMPASS: An ab Initio Force-Field Optimized for Condensed-Phase Applications s Overview with Details on Alkane and Benzene Compounds," *J. Phys. Chem. B*, vol. 5647, no. 98, pp. 7338–7364, 1998.

[23] D. Brenner, "Empirical potential for hydrocarbons for use in simulating the chemical vapor deposition of diamond films," *Phys. Rev. B*, vol. 42, no. 15, pp. 9458–9471, 1990.

[24] A. C. T. van Duin, S. Dasgupta, F. Lorant, and W. a. Goddard, "ReaxFF: A Reactive Force Field for Hydrocarbons," *J. Phys. Chem. A*, vol. 105, pp. 9396–9409, oct 2001.

[25] N. Allinger, "Molecular Structures by Computational Methods," in *Mol. Struct. Underst. Steric Electron. Eff. from Mol. Mech.*, pp. 28–50, Hoboken: Wiley, 2010.

[26] H. C. Andersen, "Molecular dynamics simulations at constant pressure and/or temperature," *J. Chem. Phys.*, vol. 72, no. 1980, p. 2384, 1980.

[27] H. J. C. Berendsen, J. P. M. Postma, W. F. van Gunsteren, a. DiNola, and J. R. Haak, "Molecular dynamics with coupling to an external bath," *J. Chem. Phys.*, vol. 81, no. 8, pp. 3684–3690, 1984.

[28] S. Nosé, "A unified formulation of the constant temperature molecular dynamics methods," *J. Chem. Phys.*, vol. 81, no. 1, pp. 511–519, 1984.

[29] W. G. Hoover, "Canonical dynamics: Equilibrium phase-space distributions," *Phys. Rev. A*, vol. 31, no. 3, pp. 1695–1697, 1985.

[30] M. D. Hanwell, D. E. Curtis, D. C. Lonie, T. Vandermeerschd, E. Zurek, and G. R. Hutchison, "Avogadro: An advanced semantic chemical editor, visualization, and analysis platform," *J. Cheminform.*, vol. 4, no. 8, pp. 1–17, 2012.

[31] L. Martinez, R. Andrade, E. Birgin, and J. M. Martinez, "Packmol: A Package for Building Initial Configurations for Molecular Dynamics Simulations," *J. Comput. Chem.*, vol. 30, no. 13, pp. 2157–2164, 2009.

[32] S. Plimpton, "Fast Parallel Algorithms for Short-Range Molecular Dynamics," *J. Comput. Phys.*, vol. 117, no. 1, pp. 1–19, 1995.

[33] W. Humphrey, A. Dalke, and K. Schulten, "VMD: Visual molecular dynamics," *J. Mol. Graph.*, vol. 14, no. 1, pp. 33–38, 1996.

[34] A. Stukowski, "Visualization and analysis of atomistic simulation data with OVITOthe Open Visualization Tool," *Model. Simul. Mater. Sci. Eng.*, vol. 18, no. 1, p. 015012, 2009.

[35] T. Kalil and C. Wadia, "Materials Genome Initiative for Global Competitiveness," tech. rep., 2011.

[36] D. N. Theodorou and U. W. Suter, "Molecular Structure of Vinyl Polymer Glass.," *Am. Chem. Soc. Polym. Prepr. Div. Polym. Chem.*, vol. 25, no. 1, p. 180, 1984.

[37] A. A. Gavrilov, P. V. Komarov, and P. G. Khalatur, "Thermal properties and topology of epoxy networks: A multiscale simulation methodology," *Macromolecules*, vol. 48, no. 1, pp. 206–212, 2015.

[38] C. Li and A. Strachan, "Molecular simulations of crosslinking process of thermosetting polymers," *Polymer (Guildf).*, vol. 51, pp. 6058–6070, nov 2010.

[39] L. Liu, Y. Liu, S. V. Zybin, H. Sun, and W. a. Goddard, "ReaxFF- l g: Correction of the ReaxFF Reactive Force Field for London Dispersion, with Applications to the Equations of State for Energetic Materials," *J. Phys. Chem. A*, vol. 115, pp. 11016–11022, oct 2011.

[40] A. Bandyopadhyay, P. K. Valavala, T. C. Clancy, K. E. Wise, and G. M. Odegard, "Molecular modeling of crosslinked epoxy polymers: The effect of crosslink density on thermomechanical properties," *Polymer (Guildf).*, vol. 52, pp. 2445–2452, may 2011.

[41] D. Hofmann, L. Fritz, J. Ulbrich, C. Schepers, and M. Bhning, "Detailed-atomistic molecular modeling of small molecule diffusion and solution processes in polymeric membrane materials," *Macromol. Theory Simulations*, vol. 9, no. 6, pp. 293–327, 2000.

[42] G. S. Larsen, P. Lin, K. E. Hart, and C. M. Colina, "Molecular simulations of pim-1-like polymers of intrinsic microporosity," *Macromolecules*, vol. 44, no. 17, pp. 6944–6951, 2011.

[43] L. J. Abbott, K. E. Hart, and C. M. Colina, "Polymatic: a generalized simulated polymerization algorithm for amorphous polymers," *Theor. Chem. Acc.*, vol. 132, p. 1334, jan 2013.

[44] C. Li and A. Strachan, "Molecular scale simulations on thermoset polymers: A review," *J. Polym. Sci. Part B Polym. Phys.*, vol. 53, no. 2, pp. 103–122, 2015.

[45] D. N. Theodorou and U. W. Suter, "Atomistic modeling of mechanical properties of polymeric glasses," *Macromolecules*, vol. 19, no. 1, pp. 139–154, 1986.

[46] D. Brown, J. H. R. Clarke, and M. Manchester, "Molecular Dynamics Simulation of an Amorphous Polymer under Tension. 1. Phenomenology," *Macromolecules*, vol. 24, pp. 2075–2082, 1991.

[47] G. M. Odegard, B. D. Jensen, S. Gowtham, J. Wu, J. He, and Z. Zhang, "Predicting mechanical response of crosslinked epoxy using ReaxFF," *Chem. Phys. Lett.*, vol. 591, pp. 175–178, jan 2014.

[48] L. J. Abbott, J. E. Hughes, and C. M. Colina, "Virtual synthesis of thermally cross-linked copolymers from a novel implementation of polymatic.," *J. Phys. Chem. B*, vol. 118, pp. 1916–24, feb 2014.

[49] A. Bandyopadhyay and G. M. Odegard, "Molecular modeling of physical aging in epoxy polymers," *J. Appl. Polym. Sci.*, vol. 128, pp. 660–666, apr 2013.

[50] Y. Li, *Atomistic Modeling of Environmental Aging of Epoxy Resins*. PhD thesis, 2012.

[51] T. Clancy, S. Frankland, J. Hinkley, and T. Gates, "Molecular modeling for calculation of mechanical properties of epoxies with moisture ingress," *Polymer (Guildf).*, vol. 50, pp. 2736–2742, jun 2009.

[52] L. Yao, Y. Xia, and Q. Zhou, "A study on hygrothermal degradation and recovery of an epoxy adhesive using molecular dynamics simulation," *J. Adhes. Sci. Technol.*, vol. 4243, no. December, pp. 1–14, 2015.

[53] Y.-B. Lu, Q.-S. Yang, X.-Q. He, and K.-M. Liew, "Modeling the interfacial behavior of carbon nanotube fiber/polyethylene composites by molecular dynamics approach," *Comput. Mater. Sci.*, vol. 114, pp. 189–198, 2016.

[54] B. D. Jensen, K. E. Wise, and G. M. Odegard, "Simulation of mechanical performance limits and failure of carbon nanotube composites," *Model. Simul. Mater. Sci. Eng.*, vol. 24, p. 025012, feb 2016.

[55] Y. Liu and S. Kumar, "Polymer/carbon nanotube nano composite fibers–a review.," *ACS Appl. Mater. Interfaces*, vol. 6, pp. 6069–87, may 2014.

[56] C. Hadden, B. Jensen, A. Bandyopadhyay, G. Odegard, A. Koo, and R. Liang, "Molecular modeling of EPON-862/graphite composites: Interfacial characteristics for multiple crosslink densities," *Compos. Sci. Technol.*, vol. 76, pp. 92–99, mar 2013.

[57] Y. Li, M. Kroger, and W. K. Liu, "Nanoparticle effect on the dynamics of polymer chains and their entanglement network," *Phys. Rev. Lett.*, 2012.

[58] J. Liu, J. Shen, Z. Zheng, Y. Wu, and L. Zhang, "Revealing the toughening mechanism of graphene-polymer nanocomposite through molecular dynamics simulation.," *Nanotechnology*, vol. 26, p. 291003, jul 2015.

[59] R. Rahman and J. Foster, "Deformation mechanism of graphene in amorphous polyethylene: A molecular dynamics based study," *Comput. Mater. Sci.*, vol. 87, pp. 232–240, may 2014.

[60] R. Rahman and a. Haque, "Molecular modeling of crosslinked grapheneepoxy nanocomposites for characterization of elastic constants and interfacial properties," *Compos. Part B Eng.*, vol. 54, pp. 353–364, nov 2013.

[61] H. Kim, A. a. Abdala, and C. W. Macosko, "Graphene/Polymer Nanocomposites," *Macromolecules*, vol. 43, pp. 6515–6530, aug 2010.

[62] L. Mishnaevsky, "Nanostructured interfaces for enhancing mechanical properties of composites: Computational micromechanical studies," *Compos. Part B Eng.*, vol. 68, pp. 75–84, jan 2015.

[63] V. Singh, D. Joung, L. Zhai, S. Das, S. I. Khondaker, and S. Seal, "Graphene based materials: Past, present and future," *Prog. Mater. Sci.*, vol. 56, pp. 1178–1271, oct 2011.

[64] R. Rohini, P. Katti, and S. Bose, "Tailoring the interface in graphene/thermoset polymer composites: A critical review," *Polymer (Guildf).*, vol. 70, pp. A17–A34, 2015.

[65] P. A. A. P. Marques, G. Gonçalves, S. Cruz, N. Almeida, M. K. Singh, J. Grácio, and A. C. M. Sousa, "Functionalized Graphene Nanocomposites," in *Adv. Nanocomposite Technol.*, pp. 247–272, 2011.

[66] J. Hopewell, R. Dvorak, and E. Kosior, "Plastics recycling: challenges and opportunities," *Philos. Trans. R. Soc. B Biol. Sci.*, vol. 364, no. 1526, pp. 2115–2126, 2009.

[67] Y. Jin, C. Yu, R. J. Denman, and W. Zhang, "Recent advances in dynamic covalent chemistry," *Chem. Soc. Rev.*, vol. 42, no. 16, pp. 6634–6654, 2013.

[68] C. R. Fenoli, J. W. Wydra, and C. N. Bowman, "Controllable reversible addition-fragmentation termination monomers for advances in photochemically controlled covalent adaptable networks," *Macromolecules*, vol. 47, no. 3, pp. 907–915, 2014.

[69] C. N. Bowman and C. J. Kloxin, "Covalent adaptable networks: Reversible bond structures incorporated in polymer networks," *Angew. Chemie - Int. Ed.*, vol. 51, no. 18, pp. 4272–4274, 2012.

[70] J. M. García, G. O. Jones, K. Virwani, B. D. Mccloskey, D. J. Boday, G. M. Huurne, H. W. Horn, D. J. Coady, A. M. Bintaleb, A. M. S. Alabdulrahman, and F. Alsewailem, "Recyclable, Strong Thermosets and Organogels via Paraformaldehyde Condensation with Diamines," *Science (80-.).*, vol. 344, pp. 732–736, 2014.

[71] D. Montarnal, M. Capelot, F. Tournilhav, and L. Leibler, "Silica-Like Malleable Materials from Permanent Organic Networks," *Science (80-.).*, vol. 334, pp. 965–968, 2011.

[72] C. J. Kloxin and C. N. Bowman, "Covalent adaptable networks: smart, reconfigurable and responsive network systems.," *Chem. Soc. Rev.*, vol. 42, pp. 7161–73, sep 2013.

[73] K. Yu, P. Taynton, W. Zhang, M. L. Dunn, and H. J. Qi, "Influence of stoichiometry on the glass transition and bond exchange reactions in epoxy thermoset polymers," *RSC Adv.*, vol. 4, no. 89, pp. 48682–48690, 2014.

[74] K. Yu, P. Taynton, W. Zhang, M. L. Dunn, and H. J. Qi, "Reprocessing and recycling of thermosetting polymers based on bond exchange reactions," *RSC Adv.*, vol. 4, no. 20, p. 10108, 2014.

[75] K. Yu, Q. Shi, M. L. Dunn, T. Wang, and H. J. Qi, "Carbon Fiber Reinforced Thermoset Composite with Near 100 % Recyclability," *Adv. Funct. Mater.*, vol. 26, pp. 6098–6106, 2016.

[76] R. Long, H. J. Qi, and M. L. Dunn, "Modeling the mechanics of covalently adaptable polymer networks with temperature-dependent bond exchange reactions," *Soft Matter*, vol. 9, no. 15, pp. 4083–4096, 2013.

[77] H. Yang, K. Yu, X. Mu, X. Shi, Y. Wei, Y. Guo, and H. J. Qi, "A molecular dynamics study of bond exchange reactions in covalent adaptable networks.," *Soft Matter*, vol. 11, pp. 6305–17, aug 2015.

[78] H. Yang, K. Yu, X. Mu, Y. Wei, Y. Guo, and H. J. Qi, "Molecular dynamics studying on welding behavior in thermosetting polymers due to bond exchange reactions," *RSC Adv.*, vol. 6, no. 27, pp. 22476–22487, 2016.

[79] M. S. A. Rahaman, A. F. Ismail, and A. Mustafa, "A review of heat treatment on polyacrylonitrile fiber," *Polym. Degrad. Stab.*, vol. 92, pp. 1421–1432, 2007.

[80] N. Yusof and A. F. Ismail, "Post spinning and pyrolysis processes of polyacrylonitrile (PAN) -based carbon fiber and activated carbon fiber : A review," *J. Anal. Appl. Pyrolysis*, vol. 93, pp. 1–13, 2012.

[81] J. Wang, L. Hu, C. Yang, and Y. Lu, "Effects of oxygen content in the atmosphere on thermal oxidative stabilization of polyacrylonitrile fibers," *RSC Adv.*, vol. 6, pp. 73404–73411, 2016.

[82] H. G. Chae, T. V. Sreekumar, T. Uchida, and S. Kumar, "A comparison of reinforcement efficiency of various types of carbon nanotubes in polyacrylonitrile fiber," *Polymer (Guildf).*, vol. 46, pp. 10925–10935, 2005.

[83] Y. Liu, *Stabilization and Carbonization of Studies of Polyacrylonitrile/Carbon Nanotube Composite Fibers*. PhD thesis, Georgia Institute of Technology, 2010.

[84] B. Saha, A. Furmanchuk, Y. Dzenis, and G. C. Schatz, "Multi-step mechanism of carbonization in templated polyacrylonitrile derived fibers: ReaxFF model uncovers origins of graphite alignment," *Carbon N. Y.*, vol. 94, pp. 694–704, 2015.

[85] V. Agarwal, P. J. Dauenhauer, G. W. Huber, and S. M. Auerbach, "Ab Initio Dynamics of Cellulose Pyrolysis : Nascent Decomposition Pathways at 327 and 600 C," *J. Am. Chem. Soc.*, vol. 134, pp. 14958–14972, 2012.

[86] M. S. Mettler, D. G. Vlachos, and P. J. Dauenhauer, "Top ten fundamental challenges of biomass pyrolysis for biofuels," *Energy Environ. Sci.*, vol. 5, pp. 7797–7809, 2012.

[87] M. Zheng, Z. Wang, X. Li, X. Qiao, W. Song, and L. Guo, "Initial reaction mechanisms of cellulose pyrolysis revealed by ReaxFF molecular dynamics," *Fuel*, vol. 177, pp. 130–141, 2016.

[88] T. P. Senftle, S. Hong, M. M. Islam, S. B. Kylasa, Y. Zheng, Y. K. Shin, C. Junkermeier, R. Engel-Herbert, M. J. Janik, H. M. Aktulga, T. Verstraelen, A. Grama, and A. C. T. van Duin, "The ReaxFF reactive force-field: development, applications and future directions," *Comput. Mater.*, vol. 2, p. 15011, 2016.

[89] K. Chenoweth, A. C. T. van Duin, and W. A. Goddard III, "ReaxFF reactive force field for molecular dynamics simulations of hydrocarbon oxidation.," *J. Phys. Chem. A*, vol. 112, no. 5, pp. 1040–1053, 2008.

[90] B. Koo, N. Subramanian, and A. Chattopadhyay, "Molecular dynamics study of brittle fracture in epoxy-based thermoset polymer," *Compos. Part B Eng.*, vol. 95, pp. 433–439, 2016.

[91] G. Y. Li, J. X. Ding, H. Zhang, C. X. Hou, F. Wang, Y. Y. Li, and Y. H. Liang, "ReaxFF simulations of hydrothermal treatment of lignite and its impact on chemical structures," *Fuel*, vol. 154, pp. 243–251, 2015.

[92] S. R. Kalidindi, *Hierarchical Materials Informatics : Novel Analytics for Materials Data*. 2015.

[93] C. Li, A. R. Browning, S. Christensen, and A. Strachan, "Atomistic simulations on multilayer graphene reinforced epoxy composites," *Compos. Part A Appl. Sci. Manuf.*, vol. 43, pp. 1293–1300, aug 2012.

[94] S. Niezgoda, D. Fullwood, and S. Kalidindi, "Delineation of the space of 2-point correlations in a composite material system," *Acta Mater.*, vol. 56, pp. 5285–5292, oct 2008.

[95] S. R. Kalidindi and M. De Graef, "Materials Data Science: Current Status and Future Outlook," *Annu. Rev. Mater. Res*, vol. 45, pp. 171–93, jul 2015.

[96] K. Dong, X. McDowell, DL. Kalidindi, SR. Jacob, "Dependence of mechanical properties on crystal orientation of semi-crystalline polyethylene structures," *Polymer (Guildf).*, vol. 55, pp. 4248–4257, 2014.

[97] J. Ahrens, B. Geveci, and C. Law, "ParaView : An End-User Tool for Large Data Visualization," in *Vis. Handb.*, Elsevier, 2005.

[98] V. A. Harmandaris, V. G. Mavrantzas, and D. N. Theodorou, "Atomistic molecular dynamics simulation of stress relaxation upon cessation of steady-state uniaxial elongational flow," *Macromolecules*, vol. 33, no. 21, pp. 8062–8076, 2000.

[99] A. Aramoon, T. D. Breitzman, C. Woodward, and J. A. El-Awady, "Correlating Free-Volume Hole Distribution to the Glass Transition Temperature of Epoxy Polymers," *J. Phys. Chem. B*, vol. 121, no. 35, pp. 8399–8407, 2017.

[100] C. Li and A. Strachan, "Free volume evolution in the process of epoxy curing and its effect on mechanical properties," *Polymer (Guildf).*, vol. 97, pp. 456–464, 2016.

[101] H. Dong and K. I. Jacob, "Effect of molecular orientation on polymer free volume distribution: An atomistic approach," *Macromolecules*, vol. 36, no. 23, pp. 8881–8885, 2003.

[102] L. McInnes, J. Healy, and S. Astels, "hdbscan: Hierarchical density based clustering," *J. Open Source Softw.*, vol. 2, no. 11, 2017.

[103] T. Lewiner, H. Lopes, A. W. Vieira, and G. Tavares, "Efficient Implementation of Marching Cubes' Cases with Topological Guarantees," *J. Graph. Tools*, vol. 8, no. 2, pp. 1–15, 2003.

[104] X. Lu, X. Wang, Q. Li, X. Huang, S. Han, and G. Wang, "A ReaxFF-based molecular dynamics study of the pyrolysis mechanism of polyimide," *Polym. Degrad. Stab.*, vol. 114, pp. 72–80, 2015.

[105] D. E. Jiang, A. C. T. Van Duin, W. A. Goddard, and S. Dai, "Simulating the initial stage of phenolic resin carbonization via the ReaxFF reactive force field," *J. Phys. Chem. A*, vol. 113, no. 25, pp. 6891–6894, 2009.

[106] K. A. Trick, T. E. Saliba, and S. S. Sandhu, "A kinetic model of the pyrolysis of phenolic resin in a carbon/phenolic composite," *Carbon N. Y.*, vol. 35, no. 3, pp. 393–401, 1997.

[107] A. Paajanen and J. Vaari, "High-temperature decomposition of the cellulose molecule: a stochastic molecular dynamics study," *Cellulose*, vol. 24, no. 7, pp. 2713–2725, 2017.

[108] A. K. Rappe and W. A. Goddard, "Charge Equilibration for Molecular Dynamics Simulations," *J. Phys. Chem.*, vol. 95, pp. 3358–3363, 1991.

[109] A. Strachan, E. M. Kober, A. C. T. van Duin, J. Oxgaard, and W. A. Goddard, "Thermal decomposition of RDX from reactive molecular dynamics," *J. Chem. Phys.*, vol. 122, no. 5, p. 054502, 2005.

[110] T.-h. Ko, "Influence of Continuous Stabilization on the Physical Properties and Microstructure of PAN-Based Carbon Fibers," *J. Appl. Polym. Sci.*, vol. 42, pp. 1949–1957, 1991.

[111] S. Edrington, *The Limits & Effects of Draw on Properties and Morphology of Pan- Based Precursor and the Resultant Carbon Fibers*. PhD thesis, University of Kentucky, 2017.

[112] A. A. Hagberg, D. A. Schult, and P. J. Swart, "Exploring network structure, dynamics, and function using NetworkX," *Proc. 7th Python Sci. Conf. (SciPy 2008)*, pp. 11–15, 2008.

[113] N. M. O'Boyle, M. Banck, C. A. James, C. Morley, T. Vandermeersch, and G. R. Hutchison, "Open Babel: An open chemical toolbox," *J. Cheminform.*, vol. 3, no. 10, pp. 1–14, 2011.

[114] K. L. Joshi, S. Raman, and A. C. Van Duin, "Connectivity-based parallel replica dynamics for chemically reactive systems: From femtoseconds to microseconds," *J. Phys. Chem. Lett.*, vol. 4, no. 21, pp. 3792–3797, 2013.